BORON REINFORCED FIBROIN MEMBRANE FOR PERIOSTEAL TISSUE ENGINEERING

A THESIS SUBMITTED TO
THE GRADUATE SCHOOL OF NATURAL AND APPLIED SCIENCES
OF
MIDDLE EAST TECHNICAL UNIVERSITY

BY

SEMA AKBABA FATHI

IN PARTIAL FULFILLMENT OF THE REQUIREMENTS
FOR
THE DEGREE OF DOCTOR OF PHILOSOPHY
IN
BIOTECHNOLOGY

AUGUST 2024

Approval of the thesis:

BORON REINFORCED FIBROIN MEMBRANE FOR PERIOSTEAL TISSUE ENGINEERING

submitted by **SEMA AKBABA FATHI** in partial fulfillment of the requirements for the degree of **Doctor of Philosophy** i**n Biotechnology, Middle East Technical University** by,

Prof. Dr. Naci Emre Altun
Dean, **Graduate School of Natural and Applied Sciences** _____

Prof. Dr. Yeşim Soyer Küçükşenel
Head of the Department, **Biotechnology** _____

Prof. Dr. Ayşen Tezcaner
Supervisor, **Biotechnology, METU** _____

Prof. Dr. Zafer Evis
Co-Supervisor, **Engineering Sciences, METU** _____

Examining Committee Members:

Prof. Dr. Dilek Keskin
Engineering Sciences, METU _____

Prof. Dr. Ayşen Tezcaner
Engineering Sciences, METU _____

Prof. Dr. Sreeparna Banerjee
Biological Sciences, METU _____

Assoc. Prof. Dr. Açelya Yılmazer Aktuna
Biomedical Engineering, Ankara University _____

Asst. Prof. Dr. Özge Erdemli
Molecular Biology and Genetics, Başkent University _____

Date: 14.08.2024

I hereby declare that all information in this document has been obtained and presented in accordance with academic rules and ethical conduct. I also declare that, as required by these rules and conduct, I have fully cited and referenced all material and results that are not original to this work.

Name Last name : Akbaba Fathi, Sema

Signature :

ABSTRACT

BORON REINFORCED FIBROIN MEMBRANE FOR PERIOSTEAL TISSUE ENGINEERING

Akbaba Fathi, Sema
Doctor of Philosophy, Biotechnology
Supervisor : Prof. Dr. Ayşen Tezcaner
Co-Supervisor: Prof. Dr. Zafer Evis

August 2024, 184 pages

In this thesis, novel fibroin/sulfated alginate (F/sA) membranes loaded with exosomes of human adipose derived stem cell (hADSC) treated with pure and doped hydroxyapatite (HA) were developed for periosteal tissue engineering. It was found that, co-doping of B (8 mol%) and Zn (4 mol%) to HA provided both proliferative and osteogenic effects on hADSCs and angiogenic effect on human umbilical vein endothelial cells. Both F and sA led to immunomodulation by significantly decreasing IL1B and CASP1 levels of THP-1 macrophages. However, presence of sA more than 5% did not cause significant change. Considering that cell viability and proliferation were the highest for 95:5 group, 95% F to 5% sA was chosen as the optimum ratio. Finally, effects of untreated and HA, 8B HA and 8B 4Zn HA treated exosomes were investigated. 8B HA group significantly increased exosome yield whereas treatment with all HA groups significantly decreased protein and DNA levels. Moreover, treatment with doped HA led to significant increase of RNA levels. F/sA membranes loaded with exosome groups increased early attachment and proliferation of hADSCs. Treated exosome groups were found to increase osteogenic differentiation and decreased expression of inflammatory markers except for 8B 4Zn

HA group, which increased CASP1. Overall, F/sA membrane loaded with exosomes isolated from cells treated with pure and doped HA groups were able to increase proliferation and osteogenic differentiation of hADSCs as well as immunomodulation. Further identification of exosomes isolated from differently treated cells would bring a better understanding for their effects and potential uses.

Keywords: Tissue Engineering, Hydroxyapatite, Exosome, Periosteum, Boron

ÖZ

PERİOSTEUM DOKU MÜHENDİSLİĞİ İÇİN BOR İLE GÜÇLENDİRİLMİŞ FİBROİN MEMBRAN

Akbaba Fathi, Sema
Doktora, Biyoteknoloji
Tez Yöneticisi: Prof. Dr. Ayşen Tezcaner
Ortak Tez Yöneticisi: Prof. Dr. Zafer Evis

Ağustos 2024, 184 sayfa

Bu tezde, periosteal doku mühendisliği için saf ve katkılı hidroksiapatit (HA) ile muamele edilmiş insan adipoz türevli kök hücre (hADSC) eksozomları yüklü özgün fibroin/sülfatlı aljinat (F/sA) membranlar geliştirilmiştir. B (%8 mol) ve Zn'nin (%4 mol) HA'ya birlikte katkılanması, hADSC'ler üzerinde hem proliferatif hem de osteojenik etki ve insan umbilikal ven endotel hücreler üzerinde anjiyojenik etki sağladığı bulunmuştur. Hem F hem de sA'nın, THP-1 makrofajlarının IL1B ve CASP1 seviyelerini önemli ölçüde azaltmıştır. Ancak, sA'nın %5'ten fazla olması anlamlı bir değişikliğe neden olmamıştır. Hücre canlılığı ve proliferasyonunun 95:5 grubunda en yüksek olduğu dikkate alınarak, %95 F ila %5 sA optimum oran olarak seçilmiştir. Son olarak, herhangi bir şey ile muamele edilmemiş ve HA, 8B HA ve 8B 4Zn HA ile muamele edilmiş eksozomların etkileri araştırılmıştır. 8B HA grubu eksozom verimini önemli ölçüde artırırken, tüm HA gruplarıyla yapılan muamele, protein ve DNA seviyelerini anlamlı olarak azaltmıştır. Ayrıca, katkılı HA ile muamele, RNA seviyelerinde anlamlı artışa yol açmıştır. Eksozom grupları yüklenen F/sA membranları, hADSC'lerin erken yapışma ve çoğalmasını artırmıştır. Muamele edilen tüm eksozom gruplarının osteojenik farklılaşmayı arttırdığı ve CASP1'i

artıran 8B 4Zn HA grubu dışında inflamatuar belirteçlerin ekspresyonunu da azalttığı bulunmuştur. Genel olarak, saf ve katkılı HA gruplarıyla tedavi edilen hücrelerden izole edilen eksozomlarla yüklü F/sA membranı, immünomodülasyonun yanı sıra hADSC'lerin proliferasyonunu ve osteojenik farklılaşmasını da arttırabilmiştir. Farklı şekilde muamele edilmiş hücrelerden izole edilen eksozomların daha ileri seviyede tanımlanması, etkilerinin ve potansiyel kullanımlarının daha iyi anlaşılmasını sağlayacaktır.

Anahtar Kelimeler: Doku Mühendisliği, Hidroksiapatit, Eksozom, Periosteum, Bor

To Milad, Haru & Hana

ACKNOWLEDGMENTS

I would like to express my deepest gratitude to my supervisor, Prof. Dr. Ayşen Tezcaner, and co-supervisor, Prof. Dr. Zafer Evis, for their guidance, advice, criticism, encouragement, and insight throughout the research.

I would also like to thank Prof. Dr. Dilek Keskin, and Prof. Dr. Sreeparna Banerjee, Assoc. Prof. Dr. Açelya Yılmazer Aktuna and Assist. Prof. Dr. Özge Erdemli for their suggestions and comments. I am especially thankful to Assoc. Dr. Açelya Yılmazer Aktuna for contributing to immunophenotyping characterization studies of hADSCs.

This work was partially funded by the Scientific and Technological Research Council of Turkey (TUBİTAK) under grant number 123M656 and by the METU Scientific Research Projects Coordination Unit (BAP) under grant number TEZ-D-310-2021-10665. I am also grateful to Boron Research Institute (BOREN), operating under the Turkish Energy, Nuclear and Mineral Research Agency (TENMAK), for providing infrastructure.

I would also like to express my gratitude to my lab mates Gülhan Işık, Bahadır Güner and Ahmet Engin Pazarçeviren for their help, valuable comments and friendship.

My heartfelt thanks go to my parents, Ayten Akbaba and Muharrem Akbaba, for their endless support. I will always be grateful for the efforts they put into my education.

My final and biggest thanks go to Milad, my dear husband. His unwavering support, encouragement, and understanding were my pillars of strength throughout this challenging journey.

TABLE OF CONTENTS

LIST OF TABLES

TABLES

LIST OF FIGURES

FIGURES

CHAPTER 1

INTRODUCTION

1.1 Structure and Importance of Periosteum

Periosteum can simply be defined as the tissue layer enclosing bones (Figure 1.1). Outer surface of the periosteum is made up of collagen fibers and elastin whereas its inner surface facing bone homes osteoblasts, bone precursor cells and periosteal stem cells. Periosteum plays a crucial role in both embryonic osteogenesis and bone defect repair (Li et al., 2016). In case of damage, cells homing periosteum ensure bone regeneration by migrating towards defect area (Colnot et al., 2012). Periosteum is also a highly vascularized tissue which enables nutrient transport needed for bone maintenance and regeneration (Li et al., 2016). Another crucial property of periosteum is its acting as barrier for osteosarcomas. In cases where bone has an open fracture or a tumor is curated from bone, periosteum is also damaged and loss of periosteum impairs bone regeneration (Lorenz, Couch & Burkey, 2017).

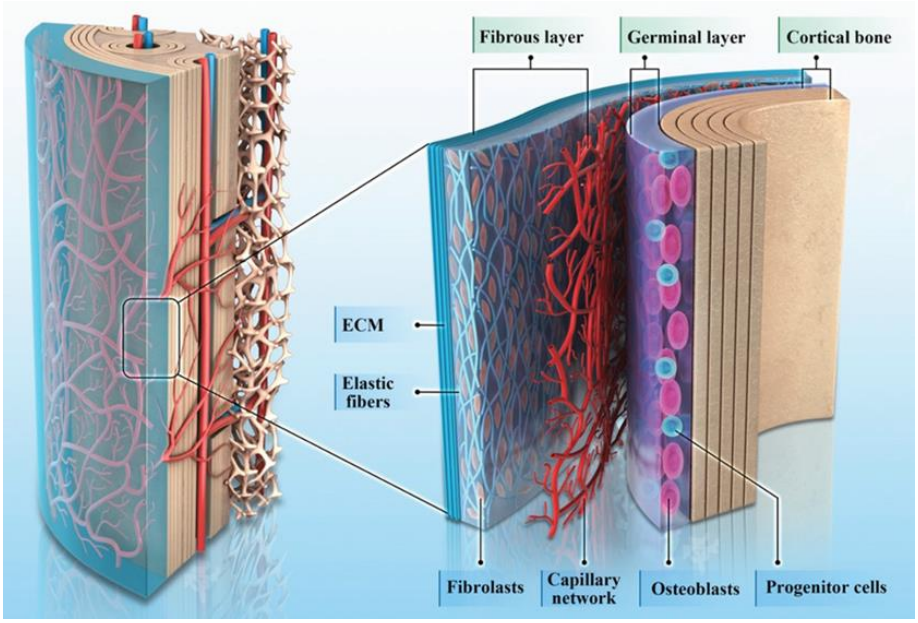

Figure 1.1 Structure of the periosteum (Lou et al., 2021).

Periosteum acts as the substantial layer of bone as it homes fibroblasts, osteoblasts bone precursor cells and stem cells (Arnsdorf et al. 2009). It was stated that periosteum derived stem cells are able to divide up to 30 times and express mesenchymal stem cell (MSC) markers. It was also denoted that periosteum derived stem cells can differentiate into chondrocyte, osteoblast, adipocyte and myocyte (De Bari et al. 2006). Ferretti et al. (2012) reported that periosteal stem cells express vascular epithelial growth factor receptor (VEGFR), an angiogenic marker. Therefore, periosteum should also be restored for proper regeneration of bone. Moreover, periosteum was used as a tissue graft in various studies. Kanou et al. (2005) showed that healthy periosteum transferred to rats with calvarial defects promoted healing of critical-sized defect. In another study, it was stated that transplantation of decellularized periosteum to rabbits with critical defects resulted in significantly more healing and bone formation (Zhao et al., 2017). Although these studies showed the potential of periosteum transplantation for bone regeneration donor scarcity and potential immunogenicity limit its use on humans. It was also denoted that chronical diseases such as diabetes hinders regenerative abilities of periosteum (Doherty et al., 2021). Considering all these properties and its cell reservoirs, it can be said that periosteum is vital for bone regeneration and bone healing can be accelerated through tissue engineering of the periosteum.

1.1.1 Regenerative Medicine Strategies Subjecting Periosteum

Regenerative medicine approach makes up relatively small part of periosteal regeneration strategies. Fan et al. (2010) cultivated bone marrow derived mesenchymal stem cells (BMSCs) supplemented with cobalt chloride, β-glycerophosphate, ascorbic acid and dexamethasone on type-I collagen membrane. Then, cellularized membranes were subcutaneously implanted to rats in order to obtain ectopic bone formation. Use of this implant is considered as limited; since collagen implant itself does not have any properties to promote osteogenesis. In

another study, combined use of Alloderm® collagen membrane and EZ Cure® calcium phosphate bone cement was shown to result in osteogenesis in dogs with ulna defect (Jegoux et al., 2009). In addition to high cost of this approach, Alloderm® collagen membrane is originally intended to be used for soft tissue regeneration purposes. In a different study, Alloderm® acellular dermal matrix was seeded with mouse osteoblast and BMSCs and wrapped around adductor muscle of mice. It was reported that seeded cells were alive after implantation and were able to perform osteogenesis (Schönmeyr et al., 2009). Use of this type of system is considered as impractical as it requires one operation for harvesting of cells and a second operation for implantation. In another study, Keskin et al. (2008) investigated potential of small intestinal submucosa cultivated with periosteal osteoblasts. It was reported that small intestinal submucosa preserved cell viability *in vitro* however, it did not have any significant effect on osteogenesis. A different study investigated efficacy of Ethisorb® patch containing polyglactin and polydioxanone on periosteal bone defects as a periosteal implant. For this purpose, cells isolated from periosteum were supplemented with tricalcium phosphate, fibrinogen and thrombin and cultivated on Ethisorb® patch. It was revealed that periosteal cells were able to produce osteogenic markers osteocalcin (OCN) and alkaline phosphatase (ALP), *in vitro* (Arnold et al., 2002). It can be said that high cost and lack of *in vivo* data can limit use of the aforesaid method. In a recent study, potential of decellularized sheep periosteum was investigated.

It was reported that viability of MC3T3-E1 preosteoblasts seeded on the acellular scaffold increased compared to tissue culture polystyrene (TCPS) during 7 days of incubation. The acellular scaffold was also subcutaneously implanted to rats. It was reported that serum levels of IL2, IL4 and interferon-γ (IFNG) were significantly lower than that of non-decellularized sheep periosteum and Bio-Gide® collagen membrane (He at al., 2020). Potential of decellularized porcine periosteum was also evaluated by *in vitro* immunomodulation assessment and rat calvarial defect model. For this purpose, hydrogel was prepared from decellularized and lyophilized porcine periosteum. It was stated that Raw264.7 macrophages seeded on the acellular

scaffolds expressed significantly lower IL1B and NOS2 and significantly higher CD206, compared to rat tail collagen hydrogel. Micro computed tomography (μ-CT) analysis also revealed that bone mineral density of the acellular scaffold group was also significantly higher than that of collagen and sham groups (Qiu et al., 2020). In another study, porcine small intestine submucosal membrane was decellularized and seeded with rabbit BMSCs. Obtained membrane was then wrapped around decellularized scapular bones. Efficacy of the composite was investigated on rabbits with irregular bone defect on the shoulder blade. Scoring of the radiographic images revealed that there was no significant difference between use of acellular submucosal membrane and combined use of acellular mucosal membrane and decellularized scapular bone, 12 weeks post-surgery. It was also mentioned that ink-formaldehyde perfusion and hematoxylin eosin study revealed acellular membrane groups enabled vascularization, due to pre-existing growth factors coming from acellular membrane (Zhao et al., 2020a). In summary, there are various regenerative medicine approaches present subjecting periosteal implants for bone regeneration, including allografts with donor scarcity, cell-based therapies without scaffolds and commercially available products that were not originally designed for bone regeneration.

1.1.2 Tissue Engineering of Periosteum

Periosteum's irreplaceable role in bone maintenance and regeneration led to studies subjecting periosteal tissue engineering. Considering periosteum's function, main concern that was taken into consideration was ability of scaffolds to promote osteogenic differentiation, which was examined mainly with presence of osteogenic proteins, histological staining, expression of osteogenic genes and μ-CT (Tao et al., 2020; Zhang et al., 2023a). Periosteum homes a variety of cells including macrophages, which engages in osteogenesis by leading periosteum derived stem cells (PDSCs) to the site of defect. Hence, immunomodulation is considered to be a key component of periosteal regeneration (Gao et al., 2019). Another concern of the engineering of the periosteum is homing and supporting the viability of stem cells,

which was assessed with various methods including cell viability assays, cell imaging studies (Kouya et al., 2013; Li et al., 2020). Since periosteum is a highly vascularized tissue, many of the studies also evaluate angiogenic activity of the periosteal scaffolds. *In vitro* tube formation, expression of angiogenic genes and presence of angiogenic proteins and histological evaluations are commonly used for determination of angiogenic potential of the scaffolds (Liu et al., 2020a, Yang et al., 2022). *In vitro* studies about periosteal tissue engineering are summarized in Table 1.1. Major part of the current literature includes use of membranes, hydrogels and electrospun nanofibers (De Souza et al., 2023; Gupta et al., 2021; Zhao et al., 2023a). Low mechanical strength of the electrospun fibers and hydrogels can possess limitation for their use in clinical applications (Zeng et al., 2003).

Table 1.1 *In vitro* studies subjecting periosteal tissue engineering.

Scaffold Composition	*Cells*	*Result*	*Remarks*	*Reference*
Collagen coated poly(L-lactide-co-ε-caprolactone) membrane	Human PDSCs	Initial cell attachment was higher than TCPS.	Combination of collagen coating and PCL improved cell attachment.	Kawase et al., 2010)
Electrospun tricalcium phosphate (TCP)/chitosan nanofiber	7F2	Increased expression of *ALP* compared to pure chitosan group.	TCP promoted *in vitro* osteogenic differentiation.	(Frohbergh et al. (2012)
Patterned collagen membrane wrapped around bioactive glass disc	BMSCs	Increased *COL1*, *ALP* and *RUNX2* expression compared to bioactive glass disc group.	Patterned collagen membrane increased *in vitro* osteogenic differentiation.	(Shi et al., 2013)
Poly(L-lactic acid) (PLA)/ polycaprolactone (PCL) membrane	Bovine PDSCs	Cell migration from periosteum pieces onto the scaffold.	PLA/PCL membrane allowed cell migration.	(Kouya et al., 2013)

Table 1.1 (continued) *In vitro* studies subjecting periosteal tissue engineering.

Patterned poly(L-lactide-co-glycolic) acid (PLGA) membrane	hADSCs	Higher expression of RUNX2, COL1 and osteocalcin (OCN), compared to non-patterned membrane.	Presence of patterns increased osteogenesis.	(Shi et al., 2014)
Electrospun gelatin/PCL/calcium phosphate (CaP) fiber	hFOB	Significantly higher cell viability and ALP activity of hFOB human fetal osteoblasts in calcium phosphate containing group compared to gelatin/poly(ε-caprolactone) only group.	CaP increased osteogenic differentiation.	(Rajzer et al., 2014)
Cytochrome C adsorbed phosphorylated chitosan/xanthan membrane	hADSCs	Scaffolds were non-cytotoxic according to lactate dehydrogenase (LDH) assay.	Phosphorylated chitosan/xanthan membrane was proven to be non-cytotoxic against hFOBs.	(de Souza et al., 2019)

Table 1.1 (continued) *In vitro* studies subjecting periosteal tissue engineering.

Electrospun PCL/CaP fiber	Rat BMSCs	*In vitro* biomineralization increased with addition of CaP. Cell viability and osteocalcin deposition significantly increased compared to PCL group.	CaP increased osteogenic differentiation.	(Liu et al., 2020b)
Electrospun PCL/carboxymethyl chitosan/sodium alginate fiber	MC3T3-E1	Expression of *ALP* and *RUNX2* was significantly higher than PCL, PCL/carboxymethyl chitosan and PCL/sodium alginate groups.	Carboxymethyl chitosan/sodium alginate synergistically increased osteogenic differentiation.	(Tao et al., 2020)
Electrospun PCL/Gelatin methacrylate (GelMA) fiber	HUVECs and MC3T3-E1	*In vitro* biomineralization detected by alizarin red staining was more than TCPS and GelMA groups. Increase in number of junctions by HUVECs, compared to other groups.	PCL (GelMA synergistically increased osteogenic differentiation and *in vitro* osteogenesis.	(Liu et al., 2020a)

Table 1.1 (continued) *In vitro* studies subjecting periosteal tissue engineering.

Collagen membrane coated with electrospun polyurethane/ascorbic acid/calcium peroxide fibers and bioglass–collagen–gelatin–nano-HA cryogel.	Rat PDSCs	Composite membrane retained cell viability better, compared to TCPS group, after induction of reactive oxygen species (ROS) by menadione.	Combination of bioglass, collagen, gelatin and nano-HA improved cell viability.	(Gupta et al., 2021)
Gelatin/chitosan oligosaccharide/ demineralized bone matrix sponge	Human PDSCs	ALP activity of the composite group at day 7 was significantly higher than that of gelatin and Gelatin/chitosan oligosaccharide groups.	Demineralized bone matrix increased osteogenic differentiation providing suitable scaffold.	(Thitiset et al., 2021)
Electrospun coaxial PCL/decellularized porcine periosteal extracellular matrix (ECM) fibers	Human BMSCs	Cell viability on day 7 and expression of *ALP*, *COL1* and *BMP2* on day 14 was similar to decellularized periosteal ECM group and significantly higher than that of PCL group.	Decellularized periosteum improved osteogenesis acting as ECM.	(Li et al., 2022a)

Table 1.1 (continued) *In vitro* studies subjecting periosteal tissue engineering.

Bilayer PCL/chitosan-xanthan membrane	Dental pulp stem cells (DPSCs)	Viability of cells treated with scaffold extracts were similar to that of untreated cells.	PCL/chitosan-xanthan membrane was not cytotoxic.	(De Souza et al., 2023)
3D printed PLA/HA/cell encapsulated GelMA	Rabbit BMSCs and PDSCs	Live/dead staining revealed that both encapsulated cells were viable immediately after crosslinking and after 7 days of cultivation.	PLA/HA/ GelMA composite was not cytotoxic.	(Zhao et al., 2023a)
3-layered electrospun fibers composed of PCL, PCL/gelatin/Mg-doped ZnO, and gelatin/bioglass/COD liver oil	NIH/3T3	Live/dead staining and Hoechst staining revealed that gelatin/bioglass/COD liver oil layer promoted cell attachment for 5 days.	Gelatin/bioglass/COD liver oil layers allowed cell viability	(Tariq et a., 2024)

Potential of periosteal scaffolds was also investigated *in vivo*. Selected *in vivo* studies subjecting periosteal tissue engineering are given in Table 1.2. It can be observed that growth factors were frequently incorporated to scaffolds, in order to improve their biological activity and/or effectivity (Romero et al., 2017; Yin et al., 2018; Romero-Torrecilla et al., 2023). Applicability of growth factors in tissue engineering are considered as limited due to risk of cancer, caused by growth factors (Korc & Friesel, 2009; Fabregat et al., 2014; Wang et al., 2017). Another strategy for improving bone and periosteum regeneration is cell delivery, which aims to compensate cell reservoirs around the area of defect (Baldwin et al., 2017; Wang et al., 2018). As drug delivery, cell therapy also faces the same risk of tumorigenicity (Barkholt et al., 2013). Additionally, location of the delivered cells in the body are also uncontrollable. In a study, electrospun chitosan scaffolds seeded with luciferase expressing hADSCs were implanted to femur. It was reported that starting from day 11, location of the cells could not be determined (Romero et al., 2017).

Table 1.2 *In vivo* studies subjecting periosteal tissue engineering.

Scaffold Composition	*Model*	*Result*	*Remarks*	*Reference*
Gelatin/chitosan/TCP membrane	Rabbit radius defect	Higher osteogenesis compared to sham group according to histological examination.	Membrane implantation improved bone healing.	(Guo et al., 2012).
Arginylglycylaspartylserine (RGDS) modified methacrylate-poly(lactide)-b-PEG-b-poly(lactide)-methacrylate hydrogel loaded with mouse green fluorescent protein^{+} (GFP^{+}) MSCs	Mouse femur defect	MSCs were visible for 8 days in hydrogel group and 1 day in MSCs injection group.	Encapsulation increased retention of the implanted cells.	(Hoffman et al., 2013)

Table 1.2 (continued) *In vivo* studies subjecting periosteal tissue engineering.

Melt spun PCL coated with luciferase expressing (Luc^+) hBMSC encapsulated star-PEG/H-heparin hydrogel on one side and $mCherry^+$ HUVEC encapsulated star-PEG/H-heparin hydrogel on other side.	Mouse femur defect	Number of vessels were significantly higher, compared to cell-free scaffold. Presence of osteoclasts were less pronounced, compared to BMSC encapsulated and cell-free scaffold groups.	Delivery of HUVECs increased angiogenesis. Combined hBMSC and HUVEC delivery delivery decreased osteoclastogenesis.	(Baldwin et al., 2017)
Fibroblast growth factor-2 (FGF-2) and transforming growth factor-β (TGFB) loaded electrospun chitosan mat wrapped around decellularized femur seeded with Luc^+ hADSCs	Rat femur defect	Chitosan nanofibers and cells had significantly higher viability compared to cell seeded femur group. No cells were able to be traced at day 11.	Use of growth factor loaded scaffold promoted cell viability which may be due to growth factors or scaffold's acting as a physical barrier. Lack of traceable cells may be due to cell death or migration.	(Romero et al., 2017)

Table 1.2 (continued) *In vivo* studies subjecting periosteal tissue engineering.

Electrospun PCL/collagen/hydroxyapatite (HA) fibers seeded with BMSCs wrapped around bone allograft	Mouse femur defect	Fibrotic capsule was less visible compared to cell-free scaffold. and increased osteogenesis compared to scaffold-only and allograft-only groups.	BMSCs contributed to immunomodulation. Cell loaded scaffold was not enough to repair the defect.	(Wang et al., 2018)
Basic fibroblast growth factor (bFGF) or bone morphogenic protein-2 (BMP-2) loaded polylactide–poly (ethylene glycol)–polylactide microcapsules loaded chitosan/collagen sponge seeded with PDSCs	Rat cranial defect	Both bFGF and encapsulated microcapsules lead to highest bone mineral density and bone volume followed by BMP-2 encapsulated group.	Growth factor delivery increased osteogenesis. bFGF was more effective.	(Yin et al., 2018)

Table 1.2 (continued) *In vivo* studies subjecting periosteal tissue engineering.

Decellularized MC3T3- E1 sheet/GelMA hydrogel	Rabbit radius segmental bone defect	According to μ-CT analysis bone volume was significantly higher, compared to GelMA group.	Decellularized cell sheet contributed to osteogenesis acting as an ECM.	(Yu et al., 2020a)
Electrospun PLA/polydopamine/ MnO_2 nanoparticle loaded with BMP-2 leptin receptor antibody	Mouse cranial defect	More stem cells recruited to defect site, compared to PLA/PDA group.	MnO_2 nanoparticle was to increase pH to promote ALP activity. Leptin receptor antibody was used to target stem cells.	(Li et al., 2020)
Electrosprayed PLGA/BMP-2 coated allograft	Mouse segmental femur defect	New bone volume detected with μ-CT was significantly higher, compared to allograft group.	Allograft was reinforced with PLGA electrospraying and functionalized with BMP-2 loading to promote osteogenesis.	(Zhuang et al., 2020)

Table 1.2 (continued) *In vivo* studies subjecting periosteal tissue engineering.

Electrodeposited poly(vinylidene fluoride-trifluoroethylene) (PVFT) on electrospun PCL/bioglass fibers	Rat calvarial defect	According to histological evaluation, new bone formation was more apparent, compared to PVFT and bioglass groups.	Bioglass fibers were employed to support osteogenesis whereas PVFT was used to provide piezoelectric base.	Zhao et al., 2020b)
Melt-drawn Nb doped bioactive glass /epoxy resin fiber	Rabbit femur defect	New bone formation and bone mineral density detected with μ-CT were highest in Melt-drawn Nb doped bioactive glass /epoxy resin fiber and lowest in sham group.	Bioactive glass /epoxy resin fiber contributed to mineralization, which was increased with Nb doping.	(Rethi et al., 2021)

Table 1.2 (continued) *In vivo* studies subjecting periosteal tissue engineering.

GelMA/methacrylated Wharton's jelly ECM/E7 peptide hydrogel	Rat cranial defect	µ-CT analysis revealed that new bone volume and bone mineral density was significantly higher compared to sham, GelMA/methacrylated Wharton's jelly ECM and GelMA/E7 peptide groups.	GelMA was used as the biocompatible base material. Wharton's jelly ECM was included to mimic native ECM whereas E7 peptide was used to home neighboring MSCs.	(Zhang et al., 2023a)
3D printed cylindrical PCL scaffold coated with poly-ethyl acrylate coated PCL loaded with BMP2 and fibronectin	Rat femur defect	Scaffolds were ectopically vascularized for 6 weeks prior to implantation. µ-CT analysis revealed that new bone formation after 10 weeks of implantation was significantly higher for all pre-vascularized groups. Healing was more prominent for 25 µg/mL BMP2 and fibronectin loaded group compared to 10 µg/mL loaded group.	Pre-vascularization contributed to osteogenesis. Osteogenic response from growth factors were dose dependent.	(Romero-Torrecilla et al., 2023)

1.2 Biomaterials

1.2.1 Fibroin (F)

F is a protein type biomaterial retrieved from silk produced by various arthropods. Domestic mulberry silkworm *Bombyx mori* can be addressed as the most common source of F (Qi et al., 2017). F consists of 390 kDa heavy light chain and 26 kDa light chain connected by a disulfide bond. Due to its unique amino acid content, F presents a semi-crystalline structure which can be turned into more crystalline version by ethanol or methanol treatment. Glycine, alanine, threonine and serine-rich N-terminal part of fibroin forms β-sheet structure in response to pH, temperature, electricity or sonication (Rockwood et al., 2011). Structure of N-terminal domain of the 2 F molecules after crosslinking, is given in Figure 1.2. Due to its source, availability and low cost, F is considered to be more advantageous than xenogeneic proteins such as collagen (Kundu et al., 2013). Moreover, F was also reported as one of the immunomodulatory biomaterials. In a study, F nanoparticles present in cell culture media were shown to reduce nitrite levels produced by RAW 264.7 macrophage cells (Chon et al., 2012).

Figure 1.2 Structure of the 2 N-terminal domains of fibroin after crosslinking (He et al., 2012).

Table 1.3 Selected studies using fibroin for various tissue engineering approaches.

Scaffold Composition	*Tissue*	*Result*	*Remarks*	*Reference*
Nanohydroxyapatite (nHA)/ silk fibroin methylacrylylated (MASF) composite (1:0 (SF), 1:0.5(SFH), and 1:1(SFHH) ratios)	Bone regeneration	Similar cell viability was observed in all groups. SFH group has shown higher mineralized calcium and ALP activity, RUNX2, Col I, ALP and OCN protein expression and RUNX2 and COL1A1 gene expression compared to SF and SFHH groups.	SF and moderate amount of nHA has enhanced osteogenesis while keeping the cells viable.	(Huiwen et al., 2024)
Exosome loaded silk fibroin (SF) and silk sericin (SS) based scaffolds prepared by simultaneous extraction (SS-SF) and separate extraction (SS SF)	Wound Healing	Wound healing of human skin fibroblast cells (BJ cells) was faster in SS-SF group compared to SS SF group. Similar wound healing capacity was observed in mice for both groups. Average blood vessel diameter for SF-SS group was larger compared to SF SS group.	Simultaneous extraction of SF and sericin, due to its mild extraction condition has provided a better wound closure capacity in vitro and new vessel formation in vivo.	(Han et al., 2021)

Table 1.3 (continued) Selected studies using fibroin for various tissue engineering approaches.

Electrospun silk fibroin membrane functionalized with laminin-511	Kidney tissue engineering	Human induced pluripotent stem cells (hiPSCs) were differentiated into better on laminin coated SF scaffold than the SF and traditional tissue culture plates coated with laminin groups. Cells cultured on laminin coated SF scaffold had higher levels of NPHS1 gene (nephrin) expression and podocin protein expression compared to laminin coated traditional tissue culture plate.	Electrospun SF coated with laminin has provided high (hiPSCs) differentiation toward podocytes by upregulating kidney related gene.	(Mou et al., 2022)
Methacrylated-SF (SF-MA) with 10, 15 and 25% concentration	Bone tissue engineering	Encapsulated MC3T3-E1 cells in 15%SF-MA scaffold had higher viability, cell area, cell perimeter, and aspect ratio compared to 10%SF-MA, 25%SF-MA, and matrigel groups. 15% SF-MA induced osteogenic differentiation in the growth medium in the absence of osteogenic factors	Methacrylated SF with suitable concentration has enhanced cell viability and osteogenic differentiation capacity.	(Rajput et al., 2022)

Table 1.3 (continued) Selected studies using fibroin for various tissue engineering approaches.

Electrospun silk fibroin with different concentrations (3%, 4%, 4.5%, 5% w/v)	Cartilage tissue engineering	Mesenchymal stem cells (MSCs) seeded on 3%SF had higher viability, GAGs and Col II production, and Col II and Sox-9 gene expression compared to 5%SF.	Electrospun SF with low concentration has shown higher cell viability and chondrogenic differentiation capacity.	(Janitermi et al., 2021)
PCL–*Antheraea mylitta* (AM) silk scaffolds and PCL–*Bombyx mori* (BM) silk scaffolds with 25% and 40% BM and AM	Maxillofacial bone tissue engineering	Human gingival mesenchymal stem cells (hGMSCs) cultured on PCL-40AM had higher cell viability compared to PCL-25AM, PCL-25BM, and PCL groups. ALP activity was higher in PCL-40AM compared to all other groups. PCL–25AM and PCL–40AM groups showed higher calcium deposition compared to other groups. Runx2, ALP, and Col I expressions were higher in PCL-40AM and PCL-40BM groups compared to other groups.	Scaffolds prepared by PCL and high ratio of *Antheraea mylitta* (AM) silk have shown higher cell viability and osteogenic differentiation capacity.	(Bojedla et al., 2022)

Table 1.3 (continued) Selected studies using fibroin for various tissue engineering approaches.

Alginate/polyvinylalcohol incorporated with silk fibroin (SF) (0 %, 0.5 %, 1 %, and 2 % SF content)	Maxillofacial bone tissue engineering	MC3T3E1 osteoblast cells cultured on the scaffolds with 1 % and 2 % SF had higher viability and proliferation compared to alginate/PVA and 0.5 % SF groups. Alginate/PVA + 2.0 % SF group had higher total protein content and deposited calcium compared to other groups. ALP activity was higher in Alginate/PVA + 1% and 2% SF compared to other groups.	Alginate/PVA scaffolds with higher SF (1 and 2%) content have shown higher cell viability, proliferation and osteogenic differentiation capacity.	(Sangkert et al., 2021)

Table 1.3 (continued) Selected studies using fibroin for various tissue engineering approaches.

Combining different concentrations of hyaluronic acid-tyramine (HA-Tyr) with regenerated silk-fibroin (SF) (HA100/SF0, HA20/SF80, and HA10/SF90)	cartilage tissue engineering	Cell laden chondrocytes inside HA10/SF90 hydrogel treated with chondrogenic medium had higher viability and COL1A2 gene expression at day 7 compared to day 1. HA20/SF80 hydrogel treated with chondrogenic medium had higher COMP genre expression and lower IL-6 expression on day 7 compared to day 1. HA20/SF80 group showed the highest GAG production compared to other groups.	While all groups have shown high cellular viability profile, HA20/SF80 groups has higher anti-inflammatory and chondrogenic differentiation capacity.	(Ziadlou et al., 2021)

1.2.1.1 Fibroin in Periosteal Tissue Engineering

In this thesis, fibroin was used as the base material for periosteal implant in order to promote regeneration of both bone and periosteum (Kim et al., 2005). Fibroin was chosen in order to mimic periosteum as it is a protein and has fiber type molecules resembling native periosteum. Moreover, fibroin can be obtained and processed in an aqueous form (Rockwood et al., 2011). By courtesy of this property, an environmentally friendly implant was fabricated.

There are 7 studies present where F was proposed as a biomaterial for periosteal implant. In one of these studies, electrospun F containing HA was cultivated with rat BMSCs, and cell viability and osteogenic differentiation were investigated. It was reported that the addition of HA led to increased cell viability and ALP activity. Any *in vivo* studies were not performed (Ding et al., 2016). Although osteogenesis was promoted with the addition of HA, the fabricated scaffold's mechanical strength was found to be significantly lower than that of a healthy human periosteum (Zeng et al., 2003; Ding et al., 2016). In another study, one side of the F sponge was coated with dexamethasone containing electrospun poly(vinyl alcohol) fibers. Fabricated scaffolds were seeded with stem cells isolated from human exfoliated deciduous teeth. Osteogenic differentiation was investigated with ALP activity and expression of osteogenic marker genes. The researchers stated that dexamethasone-containing scaffolds had significantly higher ALP activity than that of tissue culture polystyrene, although there was a drop in the expression levels of type-I collagen and Runx2 genes. Tensile strength and *in vivo* potential of scaffolds were not investigated (Su et al., 2016).

In a more recent study investigating the use of F membrane mineralized with amorphous calcium phosphate for periosteal tissue engineering, it was found that compared to unmineralized F membrane, mineralized F membrane enabled osteogenic differentiation of mesenchymal stem cells *in vitro*, by increasing expression of osteopontin and osteocalcin (Shuai et al., 2021). A different study

evaluated use of F sponge covered with F mat, seeded with BMSCs and endothelial progenitor cells, as an artificial periosteum. ALP activity assay and alizarin staining revealed that, use of the developed artificial periosteum with osteogenic differentiation medium significantly increased osteogenic differentiation, compared to undifferentiated BMSCs seeded on TCPS. However, differentiated BMSCs were not taken into comparison. It was also mentioned that compared to electrospun F and cell free scaffold groups, cell seeded scaffold group significantly increased bone volume to tissue volume ratio, in a rabbit critical size bone defect model (Yu et al., 2023). Different from the aforementioned study using cell transplantation, present work aims to promote healing through exosomes, which less likely to cause tumor formation (Zhang & Cheng, 2023b). In another study, methacrylated F-based, hamburger-like 3-layered hydrogel was developed for periosteal tissue engineering. Top and bottom layers were pure methacrylated F hydrogels whereas middle layer was contained calcium peroxide encapsulated PLA nanoparticles and cell sheets of human BMSC and RAW 264.7. Confocal imaging revealed that both cell types were able to proliferate during 24 hours of incubation. It was also mentioned that extracts from composite cell encapsulated group improved *in vitro* tube formation of HUVECs, compared to F hydrogel group. Effectivity of the hydrogel groups was also tested *in vivo*, against mouse cranial defect. Masson trichrome stain reveled that composite cell encapsulated group improved new bone formation compared to sham and non-cell encapsulated composite group (Hao et al., 2024).

Overall, developed periosteal hydrogel was shown to have potential for angiogenesis and osteogenesis. However, cell-based therapy carries the risk of tumorigenicity (Barkholt et al., 2013). Considering this, in this thesis, exosomes were chosen as an alternative to cell encapsulation. Another study reported that, electrospun F, loaded with melatonin showed similar characteristics to native periosteum in terms of degradation rate, tensile strength and surface wettability. It was also mentioned that melatonin loading significantly increased osteogenic differentiation of rat BMSCs and *in vitro* tube formation of human HUVECs, compared to F group (Deng et al., 2024). In the most recent study electrospun F/HA fibers were loaded with stromal

cell-derived factor-1α (SDF-1α) and calcitonin gene-related peptide (CGRP) by immersion. It was stated that presence of HA or loading of SDF-1α and CGRP did not alter the viability of rat periosteal stem cells, during 7 days of incubation. However, it was also mentioned that loading of CGRP, significantly increased expression of *ALP*, *BMP2*, *OPN* and *COL1* (Yao et al., 2024a). Different from these two studies, in this thesis, F was enriched with exosomes, instead of using drugs.

1.2.2 Sulfated Alginate (sA)

Alginate is a non-branched polysaccharide produced by brown algae. Alginate's repeating units are composed of (1→4)-linked β-D-mannuronate and α-L-guluronate (Figure 1.3). Alginate's free hydroxyl groups enable its modification with functional groups such as sulfate, in order to alter its interaction with other biomolecules, such as proteins (Arlov et al., 2014). In this thesis, sA was used for immunomodulation. The chemical structure of sA repeating unit is given in Figure 1.3.

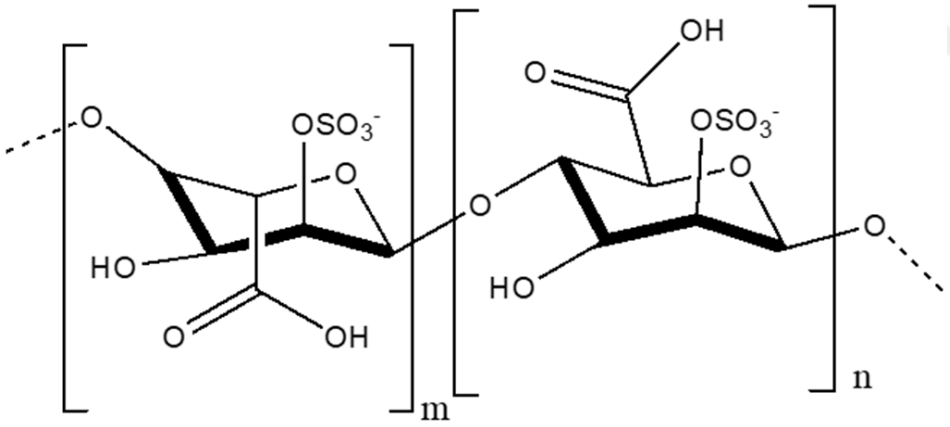

Figure 1.3 Chemical structure of sA repeating unit.

During repair of bone defects, periosteal stem cells differentiate into monocytes and migrate to the defect area as inflammatory response (Colnot et al., 2012). Therefore, immunomodulation of defect area is considered as important for proper bone healing. Kerschenmeyer et al. (2017) reported that sulfated alginate dissolved in cell culture medium reduces expression levels of proinflammatory cytokines genes such as

tumor necrosis factor-α (TNF-α) and interleukin-6 (Il-6) genes. Moreover, cytokines and growth factors must be able to bind to glycosaminoglycans such as heparin, in order to be recognized by cells (Mulloy and Rider 2006). Sulfated alginate was stated to resemble heparin, in terms of its structure (Arlov et al., 2014). Therefore, it is expected that cytokines and growth factors present in body would be able to bind periosteal implant and promote cell viability and differentiation. Tissue engineering approaches subjecting sA are given in Table 1.4.

Table 1.4 Studies using sA for various tissue engineering approaches.

Scaffold Composition	*Tissue*	*Result*	*Remarks*	*Reference*
Core/shell nanofibrous scaffold based on poly(ε-caprolactone) (PCL) as a core material and alginate sulfate (Algs)-poly(vinyl alcohol) (PVA) blend (30:70 and 50:50) as shell material (Algs-PVA/PCL)	Cartilage tissue	MSCs cultured on Algs-PVA/PCL 30:70 and Algs-PVA/PCL 50:50 showed similar viability. Collagen type II expression was higher in Algs-PVA/PCL 30:70 scaffold compared to Algs-PVA/PCL 50:50	Lowering the ratio ofAlgs to PVA from 50:50 to 30:70 did not have effect on viability but enhanced chondrogenic differentiation capacity.	(Omrani et al., 2024)

Table 1.4 (continued) Studies using sA for various tissue engineering approaches.

Sulfated alginate (Algs) hydrogel	Cartilage tissue	TGF-β1 expressing p2/0-Ag14 cells encapsulated in Algs hydrogel induced migration of adipose-derived MSCs (Ad-MSCs) compared to empty scaffold. TGF-β1 expressing p2/0-Ag14 cells induced higher Col II, Sox-9 and aggrecan, and lower Col I expression in Ad-MSCs compared to 10 ng/ml of commercial TGF-β1 with Ad-MSCs encapsulated Algs hydrogel and Ad-MSCs embedded in the Algs hydrogel groups.	Co-culturing TGF-β1 expressing cells with Ad-MSCs in Algs hydrogel compared to direct addition of TGF-β1 to Ad-MSCs provided much higher cell migration and chondrogenic differentiation.	(Askari et al., 2019)

Table 1.4 (continued) Studies using sA for various tissue engineering approaches.

Sulfated alginates (Algs) hydrogel loaded with Prussian blue (PB) nanozymes (PB+Algs-H/L) H/L: high or low degree of sulfation	Wound repair	HUVECs, NIH 3T3, and RAW264.7 cells cultured with PB+Algs-H hydrogel displayed similar proliferation and hemocompatibility compared to Algs-H, Algs-L and Alg groups. IL-8, MCP-1, and VEGF levels as heparin-binding proteins in PB+Algs-H and Algs-H groups were higher than Algs-L and Alg groups. M1 macrophages had higher levels of CD206 and Arg-1 expression as M2 marker in Algs-L, Algs-H, and PB+Algs-H groups compared to Alg group. PB+Algs-H showed the highest healing rate in wound model in mice compared to other groups	Sulfation promoted immunomodulation with higher degree being more effective. Incorporation of PB as an antioxidant with capacity to scavenging of ROS increased angiogenic property and M2 macrophage polarization of the hydrogel.	(Huang et al., 2023)

Table 1.4 (continued) Studies using sA for various tissue engineering approaches.

Double-network (DN) hydrogel based on sulfated alginate and chitosan and bioconjugation of catechol (DN/Algs-Cat and Algs-Cat/CS)	Cartilage tissue	DN/Algs -Cat, Algs-Cat/CS, and Algs/CS had higher viability of mesenchymal stem cells/chondrocytes (MSC/CHs) compared to Alg/CS. Rabbit articular regeneration was better and cartilage formation and GAGs staining were higher in Algs-Cat/CS and DN/ Algs-Cat groups compared to Algs/CS and Alg/CS groups.	Incorporation of catechol as reversible crosslinking moiety enhanced self-healing, higher strength and toughness properties of the DN/SAlg-Cat hydrogel. Presence of sulfated alginate and catechol together enhanced the stabilization of bioactive molecules such as TGF-β1 and enhanced chonrogenic differentiation.	(Baei et al., 2021)
Sulfated alginate with 0.1% or 0.2% degrees of sulfation (Algs)	Intervertebral disc cell culture	Human nucleus pulposus cells density and viability was increased in 0.1%Algs and Alg groups and decreased in 0.2%Algs group. DNA content was lower in 0.2%Algs group compared to 0.1%Algs and Alg groups.	0.1% sulfated group had positive effect on cell proliferation and viability. Both Algs groups did not provide suitable cellular phenotype characteristics compared to non-sulfated alginate.	(Bermudez-Lekerika et al., 2024)

Table 1.4 (continued) Studies using sA for various tissue engineering approaches.

Alginate-based supramolecular polyurethane (ASPU), extended by tributylammonium alginate, biologically active, alginate-based supramolecular polyurethane (BASPU), extended by tributylammonium sulfated alginate	Vascular tissue engineering	BASPU showed continuous blood clotting capacity up to 240 min while ASPU, PCL, and Teflon failed. HUVECs seeded on BASPU showed higher and greater tube-like shape structure than PU1 and PCL. No cytotoxicity was observed among all groups. Subcutaneously implanted scaffold in the rat had lower mast cells and foreign body type giant cells and higher blood vessel formation compared to PCL.	BASPU as an elastomer with sulfated alginate had suitable endothelial cells attachment, anticoagulant, biodegradation rate, superior toughness and high elongation properties. Both supramolecular polyurethanes were hydrophobized with tributylamine to be organic polar solvent soluble. Incorporation of Algs enhanced anticoagulant capacity *in vitro*, Algs supported higher angiogenesis capacity and lower immune response *in vivo*.	(Mostafavi et al., 2021)

Table 1.4 (continued) Studies using sA for various tissue engineering approaches.

Gelatin/sulfated alginate hybrid scaffold (GEL/Algs) with (50:50, 70:30 and 90:10 ratios)	Wound healing	Human dermal fibroblasts (HDFs) treated with GEL/Algs 90:10 and GEL/Algs 70:30 groups had higher cytocompatibility compared to GEL/Algs 50:50 and GEL 100 groups. GEL/Algs 70:30 groups showed higher cell viability compared to GEL 100 group. Male diabetic mice treated with sulfated alginate bearing groups had lower mortality compared to GEL 100. GEL/Algs 70:30 showed the highest wound healing capacity, the highest rate of epidermal tissue formation, lower mast cell numbers, higher number of blood formation compared GEL/Algs 90:10 and GEL 100 groups.	Incorporation of sulfated alginate has enhanced the cell viability in all groups. GEL/Algs 70:30 has shown highest viability which can be correlated to higher cell penetration depth of cells in this group. GEL/Algs 70:30 has shown higher angiogenic and lower immune response capacity.	(Sadeghi et al., 2023)

Table 1.4 (continued) Studies using sA for various tissue engineering approaches.

Sulfated alginate (Algs) hydrogel loaded with rat derived MSCs spheroids	Muscle regeneration	Algs and Alg groups implanted in rat soleus muscles had similar MSCs viability. Acellular Algs and Alg groups showed similar fibrotic tissue formation, whereas the Algs group had less fibrotic tissue and more blood vessels. Algs and Alg showed total collagen content like contralateral muscle, whereas the acellular Alg produced excess fibrotic tissue. Insoluble collage content was similar to contralateral muscle content in Algs group compared to Alg and acellular Alg groups.	Algs has the capacity to retain the endogenous bioactive agents of the cells, therefore incorporation of it can provide a sequestering capacity for MSCs in spheroid. MSCs spheroid has shown to secret growth factors required for muscle regeneration such as VEGF, IGF-1, HGF, and bFGF. MSCs spheroid in sulfated alginate has lower fibrotic tissue formation, enhanced angiogenic capacity and collagen content similar to contralateral muscle content.	(Gionet-Gonzales et al., 2023)

1.2.3 Hydroxyapatite (HA)

HA, type of CaP with a Ca/P ratio of 1.67, composes the mineral part of the bone and 61 wt.% of the total bone. Structure of the HA ($Ca_5(PO_4)_3OH$) is given in Figure 1.4. HA has two channels along the c-axis. In channel A, oxygen ions of the phosphate group and type II Ca ions (Ca(II)) are arranged at the vertices of two equilateral triangles that are rotated 60° from each other. Channel B, with a diameter of 2 Å, contains only type I Ca ions (Ca(I)) (Fiume et al., 2021). Native presence and biocompatibility of HA, led to its synthesis to be used in biomedical applications (Canillas et al., 2017). The microstructure of synthesized HA, including surface area, morphology, grain size can be influenced by various experimental conditions and synthesis methods such as type of precursors, pH, sintering time, sintering temperature, synthesis time, synthesis method and presence of dopants (Farias et al., 2019; Sánchez-Campos et al., 2021; Tilkin et al., 2019; Jodati et al., 2022).

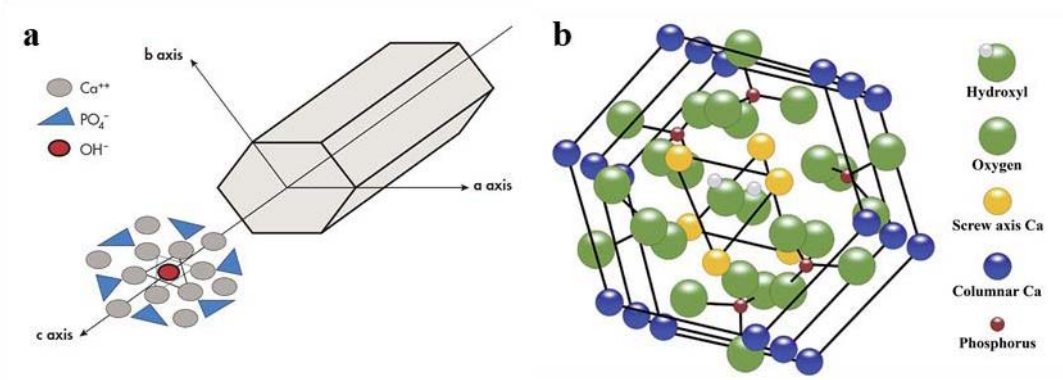

Figure 1.4 Structure of HA unit a) projected along the [001] direction and b) ABABA type arrangement of HA crystal unit (Karampour et al., 2022).

1.2.3.1 HA Synthesis Methods

HA can be synthesized with different methods including, dry, wet, high-temperature, template and deposition synthesis methods (Anandan & Jaiswal 2024). In the dry method, solid-state reactions or mechanochemical approaches can be employed. For the solid-state technique, solid reactant precursors are combined and ball-milled, either with or without the use of aqueous media. Following, the mixture is dried, compacted into pellets, and then subjected to high-temperature sintering to yield HA (Ho et al., 2013).

In the mechanochemical technique, both mechanical and chemical forces play a role in synthesis. Mechanical forces are applied during the ball-milling of the precursors which drive the chemical interactions between the precursors to produce the desired product (Ferro & Guedes, 2019). As the wet method, techniques such as sol-gel, hydrothermal, and wet chemical precipitation are employed for producing HA. The sol-gel technique uses a colloidal solution of precursor reactants and performed by stirring without heating to high temperatures. A gelling agent is added during stirring to facilitate gel formation. Once the gel has matured, it is dried in an oven, followed by calcination and sintering (Farazin & Ghasemi, 2022). In the hydrothermal method, aqueous precursor reactants react with each other at elevated temperatures (100-200°C) within a high-pressure environment using an autoclave (Sadetskaya et al., 2021).

In the wet precipitation method, the phosphate precursor is gradually added to the calcium precursor while maintaining an alkaline pH. Afterward, the mixture is allowed to age at room temperature before undergoing filtration, oven drying, calcination, and sintering for further use (Zampieron et al., 2023). The wet precipitation method can be combined with microwaving to decrease the reaction time and consumed energy, heat the precursors uniformly and efficiently and to produce highly pure and small sized particles with narrow size dispersion (Sabu et al., 2019). In the high-temperature method, the ultrasonic spray pyrolysis technique is documented in the literature. This process consists of four main steps: first,

droplets are formed through ultrasonic irradiation using a vibrator; second, the solvent is removed from the droplet surface in a lower-temperature furnace; third, microcrystals form on the droplet surface in a higher-temperature furnace; and finally, the microcrystals grow (Ueda et al., 2021). In the template method, techniques such as polymer template, emulsion, and Schiff base methods have been developed. In the polymer template technique, polymers serve as templates, and precursors are gradually added to the polymer solution to form HA. Once the reaction is complete, the mixture is allowed to age before undergoing additional processes like calcination (Akshata, Harichandran & Murugan, 2023). Using the emulsion technique, where two or more immiscible liquids are involved, precursor reactant solutions in the aqueous phases are added separately to an organic solvent (oil phase) containing an appropriate type and concentration of surfactant while the emulsion is stirred. The reaction proceeds until HA is formed, which can then be dried and calcined for further use (Tai, Fu & Don, 2012).

In the Schiff-base technique, specific compounds containing aldehyde or ketone functional groups, where the carbonyl group is replaced by an imine or azomethine group, act as ligands to coordinate the reaction between precursors to obtain HA. Typically, an equimolar amount of Schiff-base is added to the calcium precursor. The phosphate precursor solution is then slowly added to the calcium precursor solution while stirring. The reaction mixture is subsequently heated, precipitated, washed, and dried for further use (Anandan, Kumar & Jaiswal, 2023). For the deposition method, both electrodeposition and biomimetic deposition techniques are recommended. Electrodeposition is commonly used for coating applications, such as coating implants with biocompatible materials. This technique employs an electrode system consisting of an anode and a cathode to reduce the dissolution of the electrolyte solution using an electric current. After electrodeposition, the coated samples are treated with alkali-heat solutions for a few hours at a specific temperature, followed by cleaning, drying, and calcination (Yu et al., 2021). In the biomimetic technique a simulated body fluid solution containing HA precursors and other well-defined ionic compounds is prepared to initiate HA formation, with or

without the use of stimulators such as ultrasonic irradiation. After precipitation, HA is filtered, washed, dried, and calcined (Hernández, et al., 2022)

1.2.3.2 Doped HA

Native HA is not stoichiometric due to the presence of cationic and anionic substitutions. These substitutions vary based on the concentration of the substituted ions and the specific target tissue or organ, such as bone, dentin, and enamel. In order to mimic the native HA and improve materials' properties and biological response to HA and HA composites, HA is often modified with various anions and cations (Jiang, Yuan, & Huang, 2020). Metallic cations and nonmetallic anions can be used to substitute for the calcium and phosphate groups present in HA structure, respectively. Morphology, phase composition, degree of crystallinity, grain size, surface charge, ion release, porosity, biodegradation, solubility, and mechanical strength are among the material properties that can be influenced by the integration of dopants within the crystallite lattice (Tabassum, 2022). It is also possible to use double or triple dopants to obtain desired effects. (Yilmaz, Alshemary & Evis, 2019; Liu et al., 2021).

1.2.3.2.1 B-Doped HA

The element B is doped into HA in the form of BO_3^{3-} or BO_2^-, by replacing the PO_4^{3-} and/or OH^- (Tabassum, 2020). It was stated that B-doping decreases crystallinity and crystal size, due to size difference between atoms whereas increase porosity of the particles (Jodati et al., 2022). Another study reported that B-doping can increase or decrease crystallinity, phase composition and crystallite size depending on concentration (Pazarçeviren et al., 2021). *In vitro* and *in vivo* effects of B-doping of HA are summarized in Table 1.5.

Table 1.5 Biological effects of B-doped HA.

Composite	*Cell/Animal Model*	*Results*	*Remarks*	*Reference*
Freeze dried chitosan/1.15 wt% B-doped HA	Rat ADSCs	28-day viability, ALP activity and *COL1A1* and *OPN* expressions of cells seeded on B-doped HA containing group were significantly higher than that of HA containing group.	1.15 wt% B-doping contributed to osteogenic differentiation of ADSCs.	(Akdere et al., 2019)
Sulfonated Polyether ether ketone discs coated with 1.15 wt% B-doped HA	Human periodontal ligament cells	28-day viability and ALP activity of cells seeded on B-doped HA coated group were similar to that of HA coated group.	1.15 wt% B doping was not enough to cause significant change in terms of osteogenic differentiation of periodontal ligament cells	(Çayır Bozoğlu et al., 2022)

Table 1.5 (continued) Biological effects of B-doped HA.

-	hFOB HUVEC THP-1	2-week ALP activity and expression of *RUNX2* of 5 mol% B-doped group were higher than that of TCPS and HA. VEGFA release and junction points were higher for B-doped group, compared to TCPS group. Treatment with B-doped HA extracts decreased CASP1 and increased IL10 levels in macrophages differentiated from THP-1 monocytes compared to HA group.	5 mol% B doping contributed to osteogenic differentiation, angiogenesis and immunomodulation.	(Pazarçeviren et al., 2022)
-	Saos-2	7-day viability and proliferation of Saos-2 human osteosarcoma seeded on 0.05-0.5 mol% B doped HA discs were significantly higher than that of cells seeded on HA discs. ALP activity was similar for all groups.	Up to 0.5 mol% B doping was not enough to increase osteogenic differentiation of Saos-2 cells. Saos-2 cell line is already differentiated, which may not be suitable for investigating effects of low dopant ratios.	(Jodati et al, 2022)

Table 1.5 (continued) Biological effects of B-doped HA.

B-doped HA/ baghdadite	hFOB	85% 0.5 mol% B doped HA and 15% baghdadite containing group synergistically increased cell viability on day 7.	Low B dopant ratio was able to cause synergy with baghdadite for osteogenic differentiation of hFOBs.	(Jodati et al, 2023)
Hyaluronan/ 3.54 mol% B-doped HA	Ovariectomized rabbit femur defect	10µg/ml injection of the composite led to significant increase in new bone formation, compared to hyaluronan, hyaluronan/HA, and sham groups. Bone mineral density significantly increased compared to hyaluronan and sham groups.	3.54 mol% B-doping improved bone regeneration.	(Çiftçi Dede et al., 2022)
Ti coated with B-doped HA/ alginate/gelatin	hFOBs HUVEC THP-1 Rabbit femur defect	5 mol% B-doped HA group increased ALP activity and OPN expression, increased VEGFA release, decreased levels of CASP1 and NOS2. Masson trichrome staining and immunostaining 2 months post implantation revealed that B-doped HA led to superior osteointegration.	5 mol% B doping was able to increase immunomodulation and angiogenesis. 5 mol% B doping also improves osseointegration.	(Pazarçeviren et al., 2023)

1.2.3.2.2 Zn-Doped HA

Zn-doping of HA results in replacement of the Ca^{2+} with Zn^{2+}. Although net charge of the HA is not affected by Zn-doping, lattice parameters expand, since Zn atoms are larger than Ca atoms (Tabassum, 2020). Zn-doping has been reported to decrease crystal size and phase composition, depending on the dopant ratio (Uysal et al., 2021). It was also stated that the thermal stability of Zn-doped HA decreases as the Zn ratio increases (Guerra-López et al., 2024). Zn-doping was also reported to increase the zeta potential (Cuypers et al., 2023). *In vitro*, *in vivo* and clinical effects of Zn-doping of HA are summarized in Table 1.6.

Table 1.6 Biological effects of Zn-doped HA.

Composite/ Product	*Tissue of Interest*	*Cell/ Animal Model/ Clinical Study*	*Results*	*Remarks*	*Reference*
	Bone	MG63	14-day viability of MG63 human osteosarcoma was significantly higher for 1.87 wt% Zn-doped HA sintered at 1250°C, compared to HA sintered at 1250°C, Zn-doped HA sintered at 1100°C and HA sintered at 1100°C. Cell attachment percentage 1 hour post seeding was also higher for Zn-doped HA sintered at 1250°C, compared to aforesaid groups.	Cell viability was affected by Zn doping, depending on sintering temperature, which may be the result of altered phase composition and Zn content.	(Begam et al., 2017)

Table 1.6 (continued) Biological effects of Zn-doped HA.

-	Tooth	HGF-1	There was no difference between viability of HGF-1 human gingival fibroblasts treated with HA and 7 mol% Zn-doped HA groups, but cell viability increased in all groups in a dose dependent manner. Incubation of cells with 15.625 and 125 µg/mL of HA and Zn-doped HA did not affect NO^- level after 3 days.	7 mol% Zn doping increased cell viability with increasing treatment dose without causing inflammation.	(Badea et al., 2023)
-	Bone	MC3T3-E1	0.2 wt% Zn-doped HA allowed adhesion of MC3T3-E1 mouse preosteoblasts whereas 1, 2 and 10 wt.% Zn-doped HA decreased cell adhesion.	10 wt.% Zn doping was toxic which can be due to high amount of Zn release and/or formation of different phases.	(Iwamoto et al., 2022)

Table 1.6 (continued) Biological effects of Zn-doped HA.

-	Bone	BJ-1, HOS	Viability of BJ-1 human fibroblasts treated with HA, 1 mol% Zn-doped HA and 2 mol% Zn-doped HA was similar whereas 1 mol% Zn-doped groups sintered at 100, 200 and 300°C led to significant decrease in viability of HOS human osteosarcoma cells.	Cell viability in response to same material composition varied for different cell lines. Increasing sintering temperature led to different phase composition, which may contribute to aforementioned difference.	(El Hotaby et al., 2024)
Zn-doped HA disc	Bone	Rabbit tibia defect	Foreign body response was not observed from HA and Zn-doped HA groups. Radiological images showed that gap size and surrounding tissue was smaller for Zn-doped HA. H&E staining revealed that formation of vascular sinuses was more pronounced in Zn-doped HA group.	Zn doping improved osseointegration and angiogenesis.	(Bhattacharjee et al., 2014)

Table 1.6 (continued) Biological effects of Zn-doped HA.

Ti coated with 5 wt% Zn-doped HA	Bone	Goat mandible defect	SEM and H&E staining showed that Zn-doped HA coated implants resulted in earlier osteointegration, compared to HA and uncoated Ti, whereas μ-CT analysis revealed that earliest mineralization around the implant for Zn-doped HA group on week 6.	5% Zn doping accelerated osseointegration and mineralization.	(Mistry et al., 2020)
-	Bone	Whole blood cells Rat femur condyle defect	1, 5 and 10 wt% Zn-doped discs did not cause hemolysis. Van gieson staining revealed that all groups induced new bone formation, along with thin fibrous tissue layer, 4 weeks post implantation. Fibrous tissue was not detectable for 5 wt% Zn-doped HA group, after 8 weeks.	5% Zn doping yielded optimal biological response with being not hemolytic and accelerating osteointegration.	(Yang et al., 2018)

Table 1.6 (continued) Biological effects of Zn-doped HA.

microRepair® mouthwash (2 wt% Zn-doped HA containing 11 wt% Zn)	Tooth	Plaque accumulation and gingivitis	Plaque accumulation and gingivitis decreased in all groups. Listerine® and microRepair® caused significant remineralization in early carious lesions, during 45 days of follow-up.	Zn-doped HA prevented plaque accumulatio and increased remineralization of dentin.	(Hegazy & Salama, 2016; Peetsch &Epple, 2011)
microRepair® toothpaste (31.7 wt% Zn-doped HA containing 0.44 wt% Zn)	Tooth	Dentin hypersensitivity	Sensitivity scores significantly decreased compared to baseline, during 2 months of follow-up.	Zn-doped HA containing formulation reduced dentin hypersensitivity.	(Al Asmari & Khan, 2019; Peetsch &Epple, 2011)

Table 1.6 (continued) Biological effects of Zn-doped HA.

microRepair® toothpaste	Tooth	Dentin hypersensitivity	Mouth bleeding score of microRepair® and paraprobiotic containing formulation were significantly lower than Meridol® Gum Protection, during 6 months of follow-up.	Combination of Zn-doped HA and probiotics decreased dentin hypersensitivity.	(Butera, et al., 2021a)
microRepair® toothpaste	Tooth	Tooth remineralization	Calcium deposition on orthodontic buttons brushed was significantly higher than that of Sensodyne Repair & Protect, during 1 month of follow-up.	Zn-doped HA led to increased dentin remineralization.	(Butera et al., 2021b)

1.3 Exosomes

Exosomes are extracellular vesicles with size between 40 and 150 nm (Figure 1.5). Exosomes act as a mediator at cell-to-cell communication and are released from a large array of cells and carry proteins, mRNA and miRNA as their cargo, depending on cell type and cultivation conditions (Greening et al., 2015). Exosomes are being investigated for various research purposes. For example, exosomes were suggested as non-invasive biomarkers for diseases including cancer. Moreover, exosomes were also proposed as vehicles for drug delivery systems (Chung et al., 2020). Exosomes have potential applications in tissue engineering and regenerative medicine as well. Zhang et al. (2016) reported that MSC derived exosomes had regenerative potential as their injection reduced size of myocardial infarction in rat model. Exosomes were reported to have immunomodulatory properties as well (Nair & Salomon, 2018). Chen et al. (2022), stated that cultivation of human BMSC exosomes with T cells significantly reduced expression of pro-inflammatory cytokines Il-1β and TNF-α. Additionally, Lai et al. (2018) reported that exosomes derived from BMSCs lowered the effects of chronic graft versus host disease (cGVHD). The group obtained cGVHD mouse model by irradiation followed by transplanting BMSCs through tail vein injection. It was revealed that exosome treatment significantly increased survival, compared to that of untreated group. Accordingly, exosomes were chosen in order to promote cell viability, angiogenesis and immunomodulation. In another study, Huang and Feng (2017) have shown that exosomes derived from MSCs cultivated in hypoxic conditions increased angiogenesis. Also, it was denoted that exosomes derived from MSCs increased viability of cardiac muscle cells (Lazar et al., 2018). This may be attributed various exosomal cargo that can affect different pathways. Studies subjecting exosomes for various tissue engineering approaches are summarized in Table 1.7.

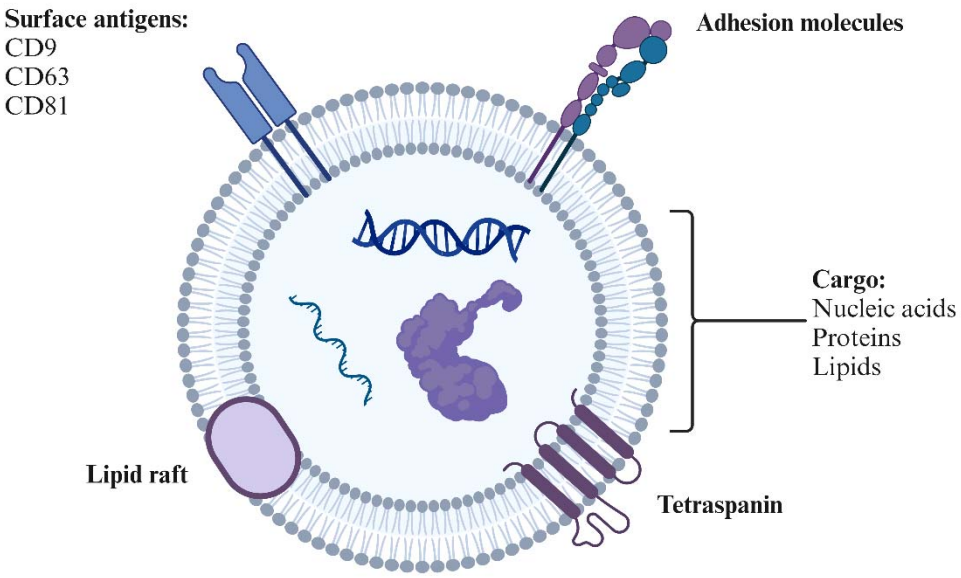

Figure 1.5 Structure of exosome (Zhang et al., 2022).

Table 1.7 Studies subjecting exosomes for various tissue engineering approaches.

Exosome Source and Concentration	*Target Tissue*	*Scaffold*	*Results*	*Remarks*	*Reference*
Diabetic (dBMSC-exos) and normal (nBMSC-exos) rat BMSC 1×10^{10} particle/mL	Rat calvarial bone defect	ShakeGel three-dimensional (3D) hydrogel containing exosome and 1.5×10^{6} BMSCs/mL	nBMSC-exos group had higher bone regeneration and mineralized bone tissue than the dBMSC-exos and without exosome groups More blood vessel and new capillary formation were seen in nBMSC-exos group compared to dBMSC-exos without exosome groups.	Bone regeneration from autologous transplantation of diabetes mellitus patients was impaired. Presence of normal exosome enhanced both osteogenic and angiogenic capacity of the cells.	(Zhu et al., 2019)

Table 1.7 (continued) Studies subjecting exosomes for various tissue engineering approaches.

BMSC 200 µg/mL	Cartilage defect	Alginate-dopamine, chondroitin sulfate, and regenerated silk fibroin (AD/CS/RSF)	Higher average International Cartilage Repair Society (ICRS) score, more migration of BMSCs, higher collagen II and aggrecan and lower collagen I were observed in mice for AD/CS/RSF/EXO group compared to AD/CS/RSF and control group (PBS treated) groups	Presence of exosome in AD/CS/RSF has enhanced its cellular migration and chondrogenic characteristics.	(Zhang et al., 2021)
HUVEC 100 µg/mL	Diabetic cutaneous wound on dorsum of mice	GelMA/PEGDA microneedles (MN) containing exosomes and Tazarotene (T)	At the end of 15th day wound area was smaller, re- epithelialized and collagen deposition was higher, and staining intensity of CD31 and a-SMA was higher in GelMA/PEGDA T + exos MN group compared to GelMA/PEGDA T MN, and GelMA/PEGDA groups	Tazarotene enhances angiogenesis. HUVECs exosome was chosen for angiogenesis. Exosome in GelMA/PEGDA T has enhanced wound healing and angiogenesis capacity of the microneedle patch.	(Yuan et al., 2022)

Table 1.7 (continued) Studies subjecting exosomes for various tissue engineering approaches.

Human urine-derived stem cells 200 μg/ hydrogel	Cranial bone in rats	Gelatin methacrylate (GelMA) and Hyaluronic acid methacrylate (HAMA) and nano-hydroxyapatite (nHAP) composite hydrogel	GelMA-HAMA/nHAP showed higher retention of Exos compared to PBS solution *in vivo*. Bone volume to tissue volume ratio, mature collagen fibres, angiogenic OCN staining, osteogenic RUNX-2 staining, trabecular number, and trabecular thickness were higher in GelMA-HAMA/nHAP Exo group compared to GelMA-HAMA/nHAP and blank groups	Human urine-derived stem cells have been reported to reduce osteolysis and enhance osteogenesis. Incorporation of Human urine-derived stem cells into GelMA-HAMA/nHAP composite hydrogel enhanced bone regeneration by defect repair.	(Lu et al., 2023)

Table 1.7 (continued) Studies subjecting exosomes for various tissue engineering approaches.

Exosome from BMSCs pretreated with Yoda1 drug 1000 µg/ml	Subcutaneous ectopic osteogenesis nude mice Bone defect in rat skull	Gelatin methacryloyl (GelMA)/methacrylated sodium alginate (SAMA)/β-tricalcium phosphate (β-TCP) hydrogels	GELMA/SAMA/β-TCP hydrogel had higher Exos retention compared to PBS solution in mice. GELMA/SAMA/β-TCP + Yoda1 treated Exo group had higher viable cells, collagen I and OCN expression, collagen and calcium deposition, and bone volume compared GELMA/SAMA/β-TCP + Exo group in mice GELMA/SAMA/β-TCP + Yoda1 treated Exo group showed higher bone volume to tissue volume ratio, and collagen deposition compared GELMA/SAMA/β-TCP + Exo group in rats.	Yoda1 which is a hydrophobic drug was shown to enhance osteogenesis. Exosome extracted from BMSCs pretreated with Yoda 1 and incorporated within hydrogel containing untreated BMSCs showed higher osteogenic regeneration capacity.	(He et al., 2024)

Table 1.7 (continued) Studies subjecting exosomes for various tissue engineering approaches.

Human umbilical cord derived mesenchymal-stem-cells (hUCMSC) 1 μg/mL	Alveolar bone defect in Rat	3D-printed silk fibroin/collagen I/nano-hydroxyapatite (SF/COL-I/nHA) composite scaffold	SF/COL-I/nHA/Exos group had higher better bone regeneration, bone volume to tissue volume ratio, trabecular number, mature osteocytes and new blood vessels, and COL1 and CD31 staining compared to SF/COL-I/nHA group.	Exosomes from hUCMSC have been used to investigate their bone regeneration capacity. Incorporation of exosomes increased the bone defect repair through enhancement in osteogenesis and angiogenesis factors.	(Sun et al., 2023)

Table 1.7 (continued) Studies subjecting exosomes for various tissue engineering approaches.

hUCMSC 10 μg/rat	T9 Spinal cord injury in rat	Gelfoam (G)	G-Exosome group treated rats showed higher neuronal regeneration, axonal remyelination, synaptic protection and formation, and lower injury induced glial scar formation, neuroinflammation and apoptosis, and neuropathic pain compared to G and blank groups.	hUCMSC injection decrease cell death in the spinal cord injury model when administered intravenously. Incorporation of exosomes into the gelfoam enhanced anti-inflammation, neuronal regeneration and protection, and reduced glial scar formation and pain-related proteins.	(Poongodi et al., 2024)

Table 1.7 (continued) Studies subjecting exosomes for various tissue engineering approaches.

Trichostatin A pretreated BMSC exosomes (T-Exo) 100 µg/scaffold	Wound in the back of mice	Collagen sponge (Col) scaffolds	Wound healing rate, wound re-epithelialization, collagen fibers density, and CD31 staining were higher for Col-T-Exo and Col-Exo compared to Col group. Lower TNF-α and iNOS (M1 phenotype) expression level and higher CD206 and Arg-1 (M2 phenotype) expression level in macrophages isolated from wound and treated with Col-T-Exo and Col-Exo were observed compared to Col group.	Trichostatin A drug has been reported to enhance differentiation and proliferation cells depending on the type of cell. Exosomes extracted from BMSCs treated with Trichostatin A showed higher wound healing and anti-inflammatory (M1 to M2 phenotype change in macrophages) capacity.	(Wang et al., 2024)

Table 1.7 (continued) Studies subjecting exosomes for various tissue engineering approaches.

Osteogenically pre-differentiated hBMSCs (o-Exo) 1×10^8 particle/mL	Bone regeneration	Gelatin methacryloyl (GelMA) hydrogel (Gel)	Cell viability was higher for Gel+ h-Exo (exosome without pre-differentiation treatment) group compared to Gel+ o-Exo. ALP activity, expression of ALP, Runx2, OCN and Col I genes, were higher in Gel+ o-Exo group compared to Gel+ h-Exo group. HUVECs density, total tube length, number of nodes and migration rate were higher in Gel+ o-Exo and Gel+ h-Exo groups compared to Gel group. LPS stimulated Raw264.7 cells treated with Gel+ o-Exo and Gel+ h-Exo groups have shown higher M2 markers.	Osteogenically pre-differentiated hBMSCs can contain growth factors and cytokines to enhance osteogenesis and angiogenesis. Exosomes from osteogenically pretreated cells caused lower viability but higher osteogenesis. Angiogenesis and anti-inflammatory effect of the osteogenically pretreated and non-treated exosomes were enhanced but both were similar to each other.	(Li et al., 2024)

Table 1.7 (continued) Studies subjecting exosomes for various tissue engineering approaches.

Genetically engineered islet-1 (ISL1)-overexpressed MSC- derived exosomes (ISL1-MSCs-Exo) 1 mg/mL	Myocardial repair	Angiogenin-1 hydrogel (Ang-1 gel)	Ang-1 gel+ ISL1-MSCs-Exo treated HUVECS had higher viability, proliferation, survival rate, migration ratio, node numbers and expression of FGF, PGF, and VEGFB genes compared to ISL1-MSCs-Exo and MSCs-Exo groups. Ang-1 gel+ ISL1-MSCs-Exo treated mice have shown higher left ventricular EF and fractional shortening, thicker infract wall, and lower fibrosis areas compared to ISL1-MSCs-Exo and MSCs-Exo treated mice.	islet-1(ISL1) overexpression has been reported to enhance angiogenesis. Exosomes extracted from ISL-1 overexpressed cells and encapsulated in Ang-1 gel showed higher wound healing and angiogenesis capacity *in vitro* and pro-angiogenetic impact in an *in vivo* ischemic heart model.	(Hu et al., 2022)

Table 1.7 (continued) Studies subjecting exosomes for various tissue engineering approaches.

HUCMSCs 40 μg/500 μL of electrospinning solution	Cardiac regeneration therapy	Polycaprolactone/type I collagen (PCL/COL-1) nanofibrous patch containing transforming growth factor beta 3 (TGF-β3) and exosome (Exo+TGF-β3+NFs)	HUVECs under oxygen/glucose-deprived condition Exo+TGF-β3+NFs had higher cell survival and proliferation, wound closure, tube formation, VEGF, IGF-1, and HGF expression and lower intracellular ROS generation compared to Exo +NFs and Exo groups. Cardiomyocytes had higher anti-apoptotic activity.	Hypoxia condition which can affect anti-apoptosis and proliferation condition. TGF-β3 has been reported to decrease scar tissue formation and fibrosis. HUCMSCs derived exosomes have been reported to reduce acute myocardial infarction injury. Exosome and TGF-β3 containing scaffold have shown higher wound healing and angiogenesis capacity, synergistically.	(Ping et al., 2023)

Table 1.7 (continued) Studies subjecting exosomes for various tissue engineering approaches.

Schwann cells 20 μg/mL	Calvarial bone defects in rat	Gelatin methacryloyl hydrogel (GelMA)	CGRP and β3-Tubulin staining in rats as innervation marker was higher in ExoGelMA compared to GelMA. ExoGelMA group showed lower local inflammatory response, TNF-α and IL-1β staining, M1 macrophages and higher M2 macrophages compared to GelMA group. Neovascularization results showed higher vessel area and vessel numbers in ExoGelMA compared to GelMA. Higher bone volume to tissue volume ratio at the end of 12 weeks and OCN and collagen I staining were observed at the end of 8 weeks in ExoGelMA compared to GelMA.	Schwann cells have been reported to help bone repair in a paracrine manner. Incorporation of Schwann cells within GelMA was shown to enhance osteogenesis, angiogenesis and anti-inflammatory effect.	(Hao et al., 2023)

Table 1.7 (continued) Studies subjecting exosomes for various tissue engineering approaches.

62	hUCMSCs 1×10^{10} particles	Skin wound healing in mice	Collagen/carboxymethyl chitosan (rhCol I/CMC) hydrogel crosslinked with genipin	At the end of 12 day, rhCol I/CMC and rhCol I/CMC-Exo groups showed higher wound closure in mice compared to rhCol I, but there was no difference between exosome containing and exosome free hydrogels. α-SMA staining as the angiogenesis marker has shown higher positive area in rhCol I/CMC-Exo group compared to rhCol I/CMC and rhCol groups. CD163 as M2 macrophages marker was higher in rhCol I/CMC-Exo group compared to rhCol I/CMC and rhCol groups.	Wound healing capacity of the rhCol I/CMC in the presence or absence of the exosome were similar and both of them were higher compared to hydrogel without carboxymethyl chitosan. Presence of exosome in the hydrogel has enhanced angiogenesis and anti-inflammatory effect.	(Wu et al., 2024)

Table 1.7 (continued) Studies subjecting exosomes for various tissue engineering approaches.

hADSCs 1×10^{9} particle/ml	Wound healing	GelMA hydrogel-combined Melt Electrowriting (MEW)-PCL scaffold (PG)	At the end of 14th day, e higher healing rate and re-epithelialization were observed in full-thickness skin wound created in the back of mice in PG-Exo treated groups compared to PG. Higher collagen type III deposition, and higher angiogenesis marker, CD31, staining and number of vessels were observed in PG-Exo treated groups compared to PG.	Incorporation of exosome within hydrogel enhanced the wound healing and angiogenesis capacity.	(Kong et al., 2024)

1.3.1 Exosomes in Periosteal Tissue Engineering

In a study, aptamer and polyethyleneimine functionalized Schwann cell exosomes were immobilized on electrospun polycaprolactone fiber mats, to obtain an artificial periosteum. Fabricated implants were shown to increase osteogenesis, angiogenesis and neural regeneration in comparison to non-exosome containing groups, in a rat critical size bone defect model (Su et al., 2022). Exosomes from treated/induced cells were also used as a periosteal tissue engineering approach to improve biological response from recipient cells. In a study, effect of exosomes in tumor xenograft model with a critical-sized bone defect was investigated. For this purpose, exosomes from non-treated or BMP2 treated rat BMSC and doxorubicin were loaded into calcium phosphate bone cement, in order to fill tumor curettage space. Defect site was also wrapped with a periosteal implant made of *Cissus quandrangularis* extract loaded polyurethane-co-ascorbic acid membrane. Bone density scan revealed that the group with exosomes obtained from BMP-2 treated cells significantly increased bone volume, compared to group containing untreated exosomes (Gupta et al., 2023). Both studies demonstrated improvement of periosteal regeneration due to exosomes, yet exact contents of the exosomes were not studied.

1.4 Aim of the Study

In orthopedics, bone fractures, and tumor curettages can lead to pseudoarthrosis which is caused by loss of periosteum. This results in delayed healing time, incomplete bone regeneration, additional cost for governments and lowered life quality for patients. Aim of this thesis was to develop a periosteal implant in order to restore lost periosteum, improve bone regeneration process and shorten healing time. Designed low-cost implant would be able to be used alone or in combination with other bone fixation implants. The periosteal implant is intended to be wrapped around defect area to provide a migration path from intact periosteum. The implant would be able to be applied during bone fixation or curation operation, without a

need for an additional operation. Considering that there are not any commercially available periosteal implants present, development of domestic, low-cost and effective implant is considered as necessary.

In the first part of this thesis, B- doped and B and Zn co-doped HA groups were synthesized and characterized. Optimized B and Zn dopant ratios were used for treatment of hADSCs whose exosomes was isolated. It was hypothesized that exosomes isolated from B and Zn-doped HA treated cells would improve osteogenic differentiation of hADSCs. Additionally, there are no studies present about synthesis and characterization of B and Zn co-doped HA. It was hypothesized that, B and Zn co-doping would increase cell viability and proliferation, angiogenesis and osteogenesis (Stanić et al., 2010; Zhong & Ma, 2017; Arslan et al., 2018).

In the second part, periosteal implant was fabricated and characterized. F and sA were used as base membrane material. It was hypothesized that F would contribute to regenerative potential whereas sA would provide immunomodulation (Kim et al., 2005; Arlov et al., 2014). Moreover, with combination of protein and polysaccharide type biomaterials, native structure of ECM would be mimicked (Arlov et al., 2014). It must be noted that currently, there are no studies subjecting F/sA composite scaffolds.

In the third part, effect of exosomes on different treatment conditions were investigated. It was hypothesized that exosome amount and exosomal cargo would be affected by treatment with different HA groups. There are currently no studies investigating the effects of dopants on exosomes and recipient cells.

Finally, fabricated scaffolds were loaded with exosomes of hADSCs treated with HA groups, in order to determine potential effects of exosome groups on periosteal regeneration. Graphical abstract of fabrication steps can be found in Figure 1.6. Exosome loading was chosen in order to increase regenerative properties and contribute to immunomodulatory properties (Lai et al., 2018; Nair & Salomon, 2018). Overall, this thesis aimed to develop and fabricate a periosteal implant with regenerative, immunomodulatory, osteogenic and angiogenic properties.

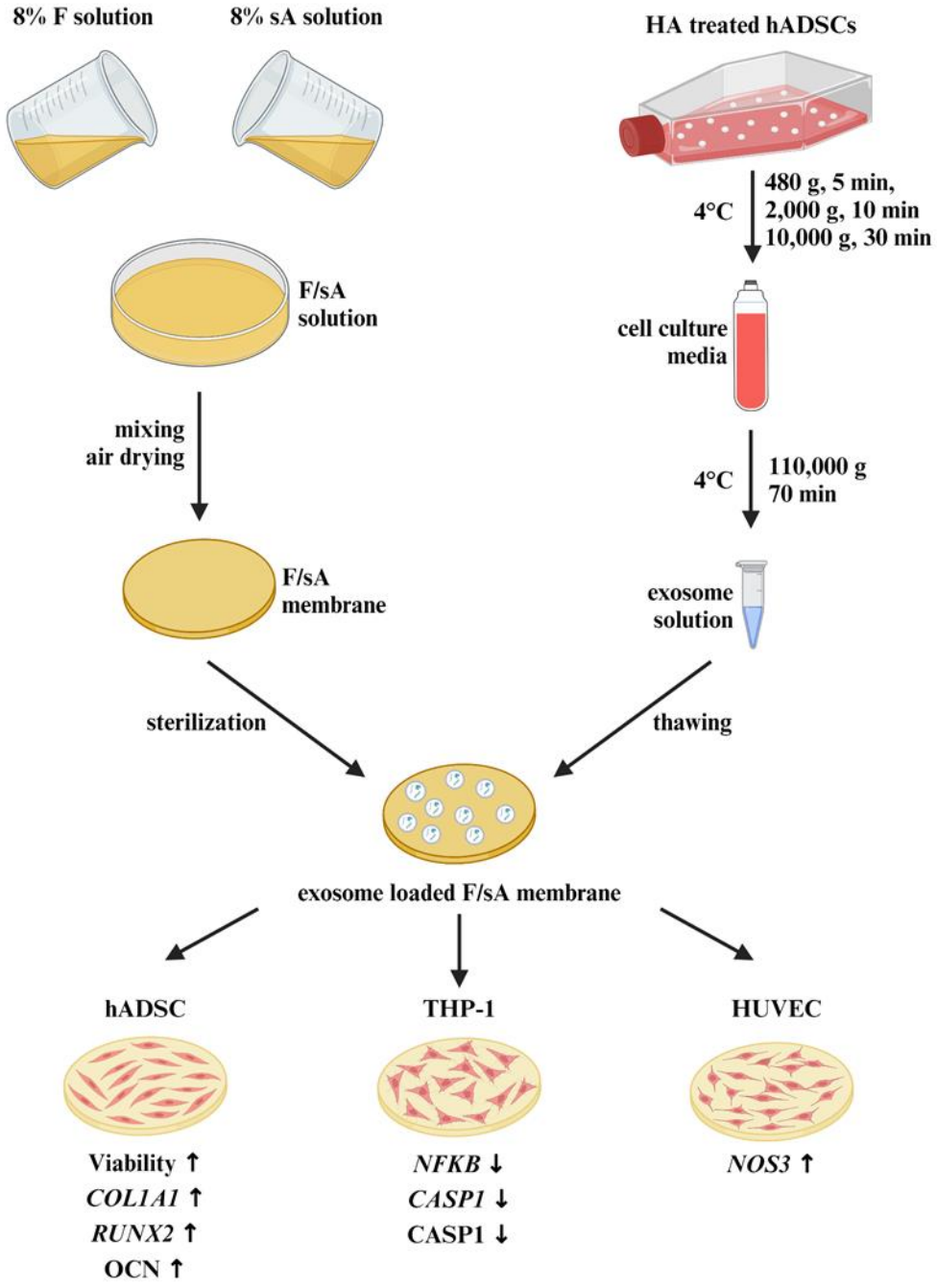

Figure 1.6 Graphical abstract (Created with BioRender.com).

CHAPTER 2

MATERIALS AND METHODS

2.1 Materials

Bombyx mori silk cocoons were purchased from Bursa Kozabirlik (Türkiye) whereas human umbilical vein endothelial cells (HUVECs) were from ATCC (USA). 1,9-dimethyl-methylene blue zinc chloride double salt (DMMB), medium viscosity sodium alginate, $C_2H_5NO_2$ (glycine), $C_6H_8O_6$ (ascorbic acid), $Ca(NO_3)_2 \cdot 4H_2O$ (calcium nitrate tetrahydrate), CH_3COOH (acetic acid), CH_3NO (formamide), collagenase type IA from *Clostridium histolyticum*, dexamethasone, dimethyl sulfoxide (DMSO), ethylenediaminetetraacetic acid (EDTA), H_3BO_3 (boric acid), HNO_3 (nitric acid), HSO_3Cl (chlorosulfonic acid), KCl (potassium chloride), KH_2PO_4 (potassium dihydrogen phosphate), LiBr (lithium bromide), Na_2CO_3 (sodium carbonate), Na_2HPO_4 (disodium hydrogen phosphate), NaCl (sodium chloride), NaN_3 (sodium azide), NaOH (sodium hydroxide), NH_4 (ammonia), $(NH_4)_2HPO_4$ (diammonium phosphate), paraformaldehyde, tris(hydroxymethyl)aminomethane (Tris), Triton X-100, uranyl acetate, $Zn(NO_3)_2.6H_2O$ (zinc nitrate hexahydrate) and β-glycerophosphate were acquired from Sigma Aldrich (USA). Dulbecco's modified eagle medium/nutrient mixture F-12 (DMEM/F12), fetal bovine serum (FBS), penicillin/streptomycin (Pen/Strep), RPMI 1640, Trypsin/EDTA, vascular cell basal medium, vascular endothelial cell growth kit were purchased from Capricorn Scientific (Germany). 3-(4,5-Dimethylthiazol-2-yl)-2,5-Diphenyltetrazolium Bromide (MTT), alamarBlue™ Cell Viability Reagent, and Quant-iT PicoGreen dsDNA Assay Kit were from Invitrogen (USA). Human Interleukin-1β (IL1B), human Caspase-1 (CASP1) and human Vascular Endothelial Growth Factor A (VEGFA) enzyme-linked immunosorbent

assay (ELISA) kits were purchased from Cusabio (China) whereas ALP activity colorimetric assay kit, human osteocalcin ELISA kit, exosomal RNA isolation kit and bicinchoninic acid (BCA) kit were supplied from Biovision (Switzerland). All of the primers were from Oligomer Biotechnology (Türkiye). bovine serum albumin (BSA) and amphotericin B were purchased from Biowest (France) while phorbol 12-myristate 13-acetate (PMA), lipopolysaccharide from *Escherichia coli* 0111:B4 (LPS), adenosine triphosphate (ATP) and normocin were from InvivoGen (USA). High Pure RNA Isolation Kit, Transcriptor First Strand cDNA Synthesis Kit and LightCycler® RNA Master SYBR Green I were supplied from Roche (Switzerland). Matrigel® was purchased from Corning (USA) whereas exosome depleted FBS was from Gibco (USA).

2.2 Methods

2.2.1 Preparation and Characterization of Biomaterials

2.2.1.1 Preparation of Biomaterials

2.2.1.1.1 Isolation of Fibroin

Fibroin isolation began with the removal of sericin which is the other component of the silk cocoon. For this purpose, 4.24 grams of Na_2CO_3 was added to 1 liter of boiling distilled water. 5 grams of silk cocoon pieces was boiled in this solution for 30 minutes. Then, fibroin cotton was washed with cold distilled water and dried at 50°C to remove sericin. The dried fibroin was dissolved in 9.3 M LiBr with a volume of 4 times of its dry weight. In order for the fibroin to dissolve completely, the mixture was incubated at 60°C for 4 hours. The resulting fibroin solution was dialyzed against dH_2O (distilled water) for 2 days. After dialysis, the fibroin solution was centrifuged at 14,000 rpm for 15 minutes to remove impurities. Concentration of the F was determined by air drying 1 ml of F solution. Following, concentration

of the F solution was set to 8% (w/v) by using dH_2O. The obtained fibroin solution was stored at 4°C (Rockwood et al., 2011).

2.2.1.1.2 Sulfation of Alginate

The sulfation of the alginate was accomplished by a one-step condensation reaction. Triple syntheses and characterizations were performed. First, 5 grams of sodium alginate was dispersed in 100 mL of CH_3NO. Then, 3.5 mL of HSO_3Cl was added and the reaction was stirred for 4 hours at 60°C. After completion of the reaction, the sulfated alginate obtained was precipitated in acetone and neutralized with 5M NaOH. Then, sA was dialyzed against distilled water for 2 days. Following dialysis, sA was lyophilized at -110°C and dry sA was stored at 4°C, until use (Daemi, Mashayekhi & Modaress, 2018).

2.2.1.1.3 Synthesis of B-Doped Hydroxyapatite

In order to investigate the effect of boron on the viability and osteogenic differentiation of stem cells, hydroxyapatite with a calcium phosphate molar ratio of 1.6 and hydroxyapatite groups containing boron in different proportions was synthesized. Triple syntheses and characterizations were performed for each group. The materials to be used for HA and boron doped hydroxyapatite (1B HA, 2B HA, 4B HA and 8B HA) and their mole percentages are given in Table 2.1. $Ca(NO_3)_2{\bullet}4H_2O$ was used as the calcium source, whereas $(NH_4)_2HPO_4$ was used as the phosphate source, and H_3BO_3 was used as the boron source. Calcium and phosphate sources were prepared as separate solutions. Boron was added to the phosphate source. Calcium and phosphate sources were dissolved in 200 mL dH_2O in separate beakers. The phosphate source was added slowly to the calcium source. The pH of the mixture was kept at 10 with the help of NH_4 from beginning of phosphate source addition until the reaction was complete. After the start of addition of the phosphate source, the mixture was stirred at 600 rpm for 30 minutes to

complete the reaction. Then, the mixture was aged in a microwave oven at 600 W for 15 minutes. The obtained precipitate was collected by filtering and the filtrate was washed until the washing water reached neutral pH value. The obtained materials were dried at 80°C followed by sintering at 500°C for 2 hours (Dasgupta et al., 2010).

Table 2.1 Precursor materials and mole percentages to be used for the synthesis of hydroxyapatite and boron doped hydroxyapatite groups.

	$Ca(NO_3)_2 \cdot 4H_2O$ (%)	$(NH_4)_2HPO_4$ (%)	H_3BO_3 (%)
HA	61.538	38.462	0
1B HA	61.538	37.462	1
2B HA	61.538	36.462	2
4B HA	61.538	34.462	4
8B HA	61.538	30.462	8

2.2.1.1.4 Synthesis of B and Zn-Doped Hydroxyapatite

In order to investigate the dual effects of B and Zn on cell viability and differentiation, hydroxyapatite groups with a calcium phosphate molar ratio of 1.67, doped with optimized B ratio and different ratios of Zn were synthesized. Triple syntheses and characterizations were performed for each group. For this reason, determined boron doped HA group was used as the control. The materials to be used for boron and zinc doped hydroxyapatite (8B 1Zn HA, 8B 2Zn HA, 8B 4Zn HA and 8B 8Zn HA) and their mole percentages are given in Table 2.2. Different from B-doped HA groups, $Zn(NO_3)_2.6H_2O$ was used as the zinc source. Calcium and Phosphate sources were prepared as separate solutions. Zinc was added to the calcium source while boron was added to the phosphate source. Calcium and phosphate sources were dissolved in 200 mL dH_2O in separate beakers. The phosphate source was then added slowly to the calcium source. The pH of the

mixture was kept at 10 with the help of NH_4 from the beginning of phosphate source addition until the reaction was complete. After the phosphate source was added, the mixture was stirred at 600 rpm for 30 minutes to complete the reaction. Then, the mixture was matured in a microwave oven set at 600 W for 15 minutes. The resulting precipitate was collected by filtering with the help of filter paper and washing was continued until washing water reached neutral pH. After the obtained materials were dried at 80°C, they were sintered at 500°C (Dasgupta et al., 2010). Synthesis steps are given in Figure 2.1.

Table 2.2 Precursor calcium and zinc sources and their mole percentages to be used for the synthesis of zinc-doped hydroxyapatite.

	$Ca(NO_3)_2{\cdot}4H_2O$ (%)	$(NH_4)_2HPO_4$ (%)	H_3BO_3 (%)	$Zn(NO_3)_2.6H_2O$ (%)
8B 1Zn HA	60.538	30.462	8	1
8B 2Zn HA	59.538	30.462	8	2
8B 4Zn HA	57.538	30.462	8	4
8B 8Zn HA	53.538	30.462	8	8

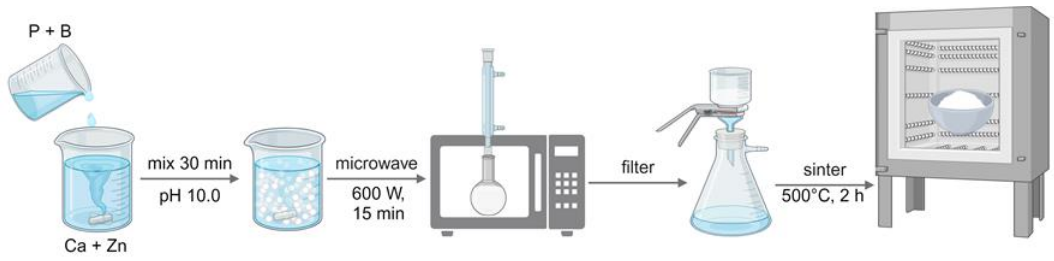

Figure 2.1 Synthesis protocol for B and Zn doped HA groups (Created with BioRender.com).

2.2.1.2 Characterization of Biomaterials

2.2.1.2.1 Determination of Fibroin Concentration

The isolated fibroin concentration was determined by the gravimetric method. 1 mL of fibroin solution was placed in a Teflon container and dried at 37°C. The solution concentration was calculated by weighing the dried fibroin. The solution was kept at 4°C after dilution to 8% concentration in dH_2O until use.

2.2.1.2.2 Determination of Degree of Sulfation

Degree of sulfation (DS) of alginate was determined with Sulfur/Carbon Determinator (LECO, Denmark). DS was calculated according to the Equation 1 where m refers weight and MW stands for molecular weight

$$DS(\%) = 100 \times \left(\frac{m_{sulfur}/MW_{sulfur}}{m_{monomer}/MW_{monomer}} \right) \quad \textbf{(1)}$$

2.2.1.2.3 Scanning Electron Microscopy (SEM)

SEM (FEI NanoSEM, USA) analysis was performed in order to observe morphology of the synthesized HA groups. Samples were sputter-coated with 3 nm of Au, prior to imaging.

2.2.1.2.4 Inductively Coupled Plasma Atomic Emission Spectroscopy (ICP-OES)

Elemental analysis was carried out in order to determine the elemental content and ratios of the synthesized HA groups. Briefly, 250 mg of material was dissolved in 8 ml of HNO_3 and the volume was completed to 50 ml with dH_2O. The samples

obtained were analyzed by ICP-OES (ICAP 7000, Thermo Scientific, USA) to determine the molar ratio of Ca, P, B and Zn (Dalgic et al., 2018).

2.2.1.2.5 X-Ray Diffraction (XRD) Analysis

XRD analysis was performed to determine the phase purity, crystallinity and crystallite size of the synthesized HA groups (Alshemary et al., 2016). XRD patterns were detected with CuKα radiation generated at 40 kV and 30 mA at 2θ angles between 10-80° with a pitch of 0.02°/sec (PANalytical Empyrean, The Netherlands).

2.2.1.2.6 Fourier Transform Infrared Spectrometer (FTIR) Analysis

FTIR analysis was performed to determine the functional groups present on sA and HA groups. Hydroxyl (OH^-), orthophosphate (PO_4^{3-}), boron dioxide (BO_2^-) and boron trioxide (BO_3^{-3}) functional groups are expected to be included in the structure of the synthesized HA groups whereas presence of -OH, -COO- and COC S=O and S-O-C bonds were investigated for sA. The analysis was performed in the mid-infrared range (4000-400 cm-1) (Bruker IFS66/S, USA).

2.2.1.2.7 Particle Size Analysis

Particle size analysis was performed in order to determine the effect of addition of boron and zinc on particle size. The size distribution of the particles of synthesized HA groups was determined by a particle size analyzer (Malvern Mastersizer 2000, UK).

2.2.1.2.8 Ion Release

Time dependent ion release from HA groups was analyzed with ICP-OES. For this purpose, 1g of the HA groups were dispersed in 10 mL of dH_2O and incubated at

37°C for 14 days. On days 2, 7 and 14, dH_2O was collected, filtered through 0.22 μm cellulose acetate filter and presence of Ca, P, B and Zn was analyzed.

2.2.1.2.9 Bioactivity Test

Effect of dopants on in vitro biomineralization was assessed by immersing HA groups in simulated body fluid (SBF, pH 7.40). For this purpose, 100 mg disc shaped samples were immersed in 10 mL of SBF incubated at 37°C, for 14 days. SBF was renewed every other day. After incubation, samples were dried at room temperature and biomineralization on samples' surfaces were examined with SEM (Turhan et al., 2023).

2.2.2 Fabrication and Characterization of Membranes

2.2.2.1 Fabrication of the Membrane Groups

F/sA scaffolds were prepared by mixing 8% ($^{w}/_{v}$) F and 8% ($^{w}/_{v}$) sA solutions. In order to obtain different F/sA ratios, prepared solutions were mixed at different volumes, so that the final volume would be 5 mL (Table 2.3). After mixing, solutions were poured in Teflon molds with diameter of 4 cm and dried at room temperature.

Table 2.3 Nomenclature, weight ratio and volumetric ratios of F/sA scaffolds.

Group	*F/sA (w/w)*	*8% F (mL)*	*8% sA (mL)*
100:0	100:0	5.00	0
95:5	95:5	4.75	0.25
90:10	90:10	4.50	0.50
80:20	80:20	4.00	1.00

2.2.2.2 Characterization of F/sA Membranes

2.2.2.2.1 SEM Imaging

Morphology of F/sA scaffolds as fabricated and after 2 weeks of biodegradation in PBS was investigated with SEM. Samples were sputter-coated as aforesaid (Akbaba et al., 2021).

2.2.2.2.2 Water Contact Angle Measurement

Water contact angle of scaffolds was measured, in order to determine effect of F/sA ratio on surface wettability. Water contact angle was determined by goniometer (Attension, Biolin Scientific, Sweden) at 25°C. dH_2O was chosen as the testing liquid and droplets were set to 7 µL. Contact angles were calculated using Young-Laplace formula (Taylor, et al., 2007).

2.2.2.2.3 Equilibrium Swelling Test

Water uptake percent of F/sA membranes was measured using the general gravimetric method. The dry weights of the 1 cm^2 samples were recorded, then the samples were incubated at 37°C in 10 mL of phosphate buffer solution (PBS, pH 7.4). After 1st, 2nd, 4th, 8th and 24th hours of incubation, the surface of the samples was gently wiped with filter paper, and weights of the wet samples were measured. Finally, the water uptake percentages of the samples were calculated, according to Equation 2, where W_0 is the initial dry weight and W_w is the wet weight at a given time (Wittayaareekul & Prahsarn, 2006).

$$Water\ Uptake\ (\%) = 100 \times \frac{W_w - W_0}{W_0} \qquad \textbf{(2)}$$

2.2.2.2.4 Weight Loss Analysis

Initial weights of 1 cm^2 specimens were weighed and the samples were incubated in 10 mL of PBS, pH 7.4. At the end of the 1^{st}, 4^{th}, 7^{th} and14^{th} days, the samples were dried by lightly wiping with filter paper and lyophilization at -80°C. After measuring the weights of the dried samples, the weight loss percentages were calculated according to Equation 3, where W_0 is the initial dry weight and W_t is the remaining dry weight at a given time (You et al., 2005).

$$Weight\ Loss\ (\%) = 100 \times \frac{W_0 - W_t}{W_0} \quad \textbf{(3)}$$

2.2.2.2.5 Release Study

Release of F and sA from the membranes was studied in PBS at 37°C . The amounts of F and sA released at 1^{st}, 2^{nd}, 4^{th} and 24^{th} hours were determined with bicinchoninic acid assay (BCA) and DMMB assay, respectively. DMMB solution was prepared by dissolving 1.15 mL acetic acid, 608 mg glycine, 320 mg NaCl and 3.2 mg DMMB in 200 mL dH_2O. The solution was filtered after setting the pH of the solution to 3.0. 200 µL of DMBB solution was mixed with 20 µL of sample or standard. After few seconds of shaking absorbance of the samples at 520 nm were recorded (Ladner et al., 2022). BSA (6.25-200 µg/mL, Appendix A) and sA (15.63-125 µg/mL, Appendix B) solutions in PBS were used as standards whereas PBS was used as blank. Released amount was expressed as the percentage of the F and sA present in samples as given in Equation 4, where W_I refers the initial weight of F or sA in sample whereas WR stands for the weight of F or sA released.

$$Release\ (\%) = 100 \times \frac{W_I - W_R}{W_I} \quad \textbf{(4)}$$

2.2.2.2.6 Tensile Test

Tensile test was performed on 4 cm x 1 cm samples wetted with PBS (Univert, Cellscale, Canada). Static tensile speed of 1 mm/min was applied. Ultimate tensile strength, Young's modulus and percent strain for membranes were determined by using the stress-strain curve. Maximum stress withstood by the sample was referred as the ultimate tensile strength whereas slope of the stress-strain curve, where the curve is linear is determined as the Young's modulus and the percent ratio of the elongation to initial length is noted as percent strain (Atila et al., 2015).

2.2.3 *In Vitro* Studies

2.2.3.1 Sample Preparation

HA groups were weighed and placed in falcon tubes, prior to sterilization. F/sA membranes were cut in 9 mm circles for ELISA studies and 35 mm circles for PCR studies. All samples were sterilized with 25 kGy γ-irradiation and stored at 4°C, until use. Exosomes were loaded on sterile F/sA membranes by impregnation for 4 hours with density of 10^7 particles/cm^2. For exosome studies, 95:5 membrane group was simply referred as F/sA, whereas membranes loaded with exosomes from untreated cells were noted as F12. Membrane groups loaded with exosomes from HA, 8B or 8B 4Zn HA treated cells were referred with the same name as the HA group used for treatment.

2.2.3.2 Cell Culture

hADSCs were cultivated in DMEM/F12 supplemented with 10% FBS and 10 U/mL Pen/Strep, in an incubator (5215, (MCO-5M-PE CO_2 Incubator, Panasonic, Japan) at 37°C with 5% CO_2 and 95% humidity. Cells were passaged when they reached 80% confluency, using 0.05% Trypsin/EDTA. Third passage cells were

cryopreserved in 10% DMSO in FBS ($^{v}/_{v}$). Osteogenic media was prepared by supplementing cultivation media with, 50 μg/mL ascorbic acid, 10mM β-glycerophosphate and 10^{-8} M dexamethasone. In studies with exosomes, media was supplemented with exosome depleted FBS.

HUVECs were cultivated with vascular cell basal medium, supplemented with vascular endothelial cell growth kit. Cells were passaged when they reached 80% confluency, using 0.05% Trypsin/EDTA. In studies with exosomes, media was supplemented with exosome depleted FBS.

THP-1 monocytes were cultivated in RPMI 1640 medium supplemented with 10% FBS 10 U/mL Pen/Strep and 50 mg/mL normocin. Cells were passaged when reached $2x10^{6}$ cells/mL. In studies with exosomes, media was supplemented with exosome depleted FBS and no antibiotics were used during immunomodulation studies.

2.2.3.3 Isolation and Characterization of hADSCs

2.2.3.3.1 Isolation of hADSCs

hADSCs were isolated from lipoaspirates as described elsewhere (Zhu et al., 2013). Required ethical approval for non-invasive clinical research was obtained from TOBB University of Economics and Technology (KAEK-118/132). First, lipoaspirate was washed with equal volume of sterile PBS containing 100 U/mL Pen/Strep and 2.50 μg/mL amphotericin B. Washing step was repeated until yellow-colored lipoaspirate was obtained. Afterwards, lipoaspirate was mixed with equal volume of 0.1% collagenase type IA. Digestion was carried out at 37°C for 30 minutes, in an orbital shaker set at 200 rpm. Then, the lipoaspirate was divided into 25 mL portions and mixed with an equal volumes of cultivation media to inactivate collagenase. Stromal vascular fraction (SVF) was obtained as a pellet, after centrifugation at 1200g for 10 minutes. SVF pellet was resuspended with cultivation

media and centrifuged again. Final pellet was resuspended with the cultivation media composed of DMEM/F12 supplemented with 10% ($^{v}/_{v}$) FBS and 10 U/mL Pen/Strep, and filtered through 100 µm cell strainer, to obtain the cell mixture containing hADSCs. Filtrate was added to the flasks and cultivated. Isolated hADSCs were cultivated with cultivation media, in an incubator (MCO-5M-PE CO_2 Incubator, Panasonic, Japan) at 37°C with 5% CO_2 and 95% humidity. Cells were passaged when they reached 80% confluency, using 0.05% Trypsin/EDTA. 3rd passage cells were used for the tests. Isolation steps are given in Figure 2.2.

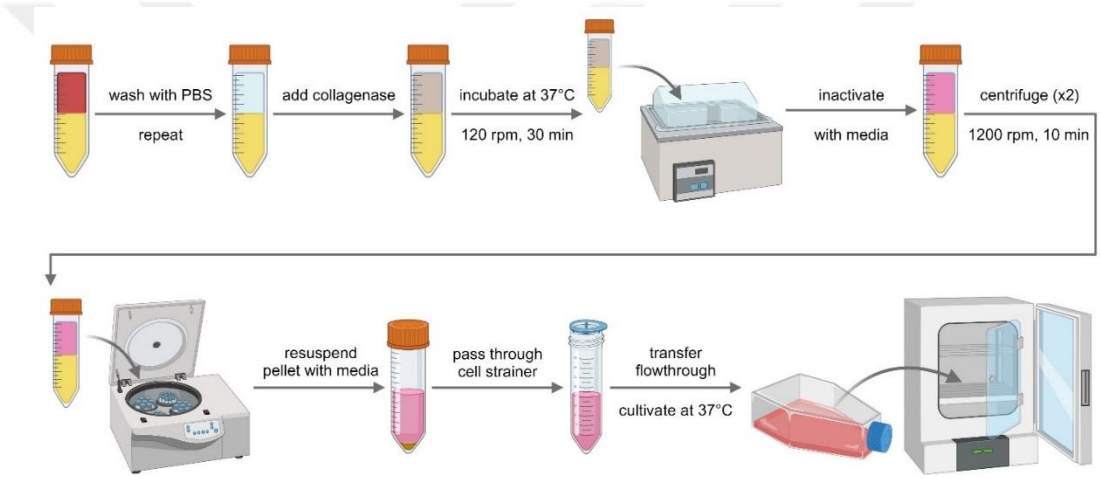

Figure 2.2. Route for isolation of hADSCs from lipoaspirates (Created with BioRender.com).

2.2.3.4 Isolation and Characterization of Exosomes

2.2.3.4.1 Exosome Isolation

Exosomes from cells treated with 0.5 mg/mL HA groups were isolated by ultracentrifugation (Greening et al., 2015). For this purpose, 2x10^{7} third passage cells were seeded to 175 cm^{2} cell culture flasks and incubated for 24 hours. Then, cells

were washed with PBS and cell culture media were replaced with media containing exosome depleted FBS or exosome depleted FBS and HA groups. HA groups to be used for treatment were chosen as HA, 8B HA and 8B 4Zn HA. Exosomes isolated from untreated cells and HA, 8B HA and 8B 4Zn HA-treated cells were referred as F12, HA, 8B HA and 8B 4Zn HA, respectively. After 48 hours of cultivation, the media were centrifuged at 480 g for 5 minutes, at 2,000 g for 10 minutes, and at 10,000 g for 30 minutes. After each step, the pellet was removed and the supernatant was collected. Final centrifugation was performed at 110,000g for 70 minutes using an ultracentrifuge (Hitachi CP100WX, Japan) and the pellet containing exosomes was resuspended in dH_2O. Isolated exosomes were stored at -80°C, until use.

2.2.3.4.2 Characterization of Exosomes

2.2.3.4.2.1 Transmission Electron Microscopy (TEM)

Morphology of the isolated exosomes was investigated with transmission electron microscopy TEM (FEI Tecnai G2 Spirit BioTwin, USA). First, 2 µL of the exosome suspension was loaded on a grid. Then, a drop of 2% uranyl acetate was added on the grid for negative staining. The grid was then washed with dH_2O twice and let dry (Hosseini-Beheshti, et al., 2016).

2.2.3.4.2.2 Nanoparticle Tracking Analysis

The concentration of exosomes isolated from cells treated with different HA groups was determined with nanoparticle tracking analysis (Nanosight NS300, Malvern, UK). For this purpose, 10 µL of exosomes was diluted to 1 mL. Particle size and concentration of the exosomes were recorded for each group.

2.2.3.4.2.3 DNA Quantification

Exosomal DNA was quantified with PicoGreen dye and normalized to particle number (Li et al., 2022b). For this purpose, 10 µL of distilled water and 50 µL of 0.1% Triton X-100 were added to 40 µL of exosomes. After lysis, 100 µL of PicoGreen solution was added and fluorescence with 480 nm excitation and 520 nm emission was recorded. The amount of the exosomal DNA was assessed by using the calibration curve constructed with bovine DNA (25 ng-1µg, Appendix C).

2.2.3.4.2.4 RNA Quantification

Exosomal RNA was isolated by using an exosomal RNA isolation kit (Biovision, Switzerland). 2µL of isolated RNA samples was quantified by using Take3 microvolume plate (Agilent, USA). The concentration of RNA was normalized with particle concentration (Li et al., 2022b).

2.2.3.4.2.5 Protein Quantification

Exosomal proteins were quantified with BCA assay kit and normalized to particle number (Li et al., 2022b). Samples were prepared by adding 20 µL of distilled water, 20 µL of 0.1% Triton X-100 and 50 µL of BCA solution into 20 µL of exosomes. After 1 hours of incubation at 37°C, the absorbance at 562 nm was recorded. Amount of exosomal protein was calculated as aforesaid.

2.2.3.5 Cell Viability Assay

2.2.3.5.1 MTT Assay

Varying concentrations of HA were tested with MTT assay, in order to determine a nontoxic working concentration on hADSCs. For this purpose, hADSCs were seeded

to 96-well plates with a density of $1x10^4$ cells/well. 24 hours after seeding, cells were treated with varying concentrations of HA and incubated for 48 hours. Then, the growth media were replaced with of 0.5 mg/mL MTT solution in DMEM/F12 without phenol red. After incubation for 4 hours, MTT solution was discarded and formazan crystals formed were dissolved in 100 µL of DMSO. Finally, the absorbance at 570 nm was measured (BioTek Synergy H1, USA). Cells which were not incubated with HA were used as control whereas wells without cells treated with different concentrations of HA were used as blanks. Relative cell viability was calculated according to the Equation 5, where $A_{control}$, A_{sample} and A_{blank} refer to absorbance values of the control, sample and blank, respectively.

$$Cell\ Viability\ (\%) = 100 \times \frac{A_{sample} - A_{blank}}{A_{control} - A_{blank}} \quad \textbf{(5)}$$

2.2.3.5.2 Alamar Blue Assay

Effect of HA groups on cell viability and proliferation was determined by Alamar Blue assay. For this purpose, hADSCs were seeded in 48-well plates with a seeding density of $2x10^3$ cells/well and incubated for 4 hours. After initial attachment, cells were treated with 0.5 mg/mL HA groups suspended in cultivation media (Panseri et al., 2012). Viability of hADSCs seeded on membrane samples were also assessed with Alamar Blue assay. Cells were seeded on membranes and cultivation media were added after 4h. Percent reduction of AlamarBlue™ dye was calculated as an indicator of cell viability on days 1, 4, 7, 11 and 14 of cultivation. Increase in viability of cells with time is interpreted as cell proliferation. Briefly, 10% AlamarBlue™ solution was prepared in DMEM/F12 medium. The prepared solution was added to the wells containing the cells and samples washed with PBS and incubated for 4 hours. Then, alamarBlue™ solutions were transferred to a new sterile plate and fresh cultivation media with HA groups were added to wells for cultivation to continue. Absorbances of transferred alamarBlue™ at 570 and 600 nm were recorded. Percent

reduction of alamarBlue^{TM} was calculated according to the Equation 6, where $A570_{sample}$, $A570_{blank}$ refer to absorbances of sample and blank at 570 nm whereas $A600_{sample}$ and $A600_{blank}$ stand for absorbances of sample and blank at 600 nm, respectively.

$$Reduction\ (\%) = 100 \times \frac{\left(117216 \times A570_{sample}\right) - (80586 \times A600_{blank})}{(155677 \times A600_{blank}) - \left(14652 \times A570_{sample}\right)} \quad \textbf{(6)}$$

2.2.3.6 Osteogenic Differentiation

ALP activity was measured, in order to determine the effect of HA groups on osteogenic differentiation of hADSCs. hADSCs were seeded in 48-well plates with a seeding density of $5x10^3$ cells/well and incubated for 4 hours. After initial attachment, cells were treated with 0.5 mg/mL HA groups suspended in osteogenic differentiation media (Panseri et al., 2012). 2 weeks of cultivation was carried out with refreshing the media containing HA groups every other day. Specific ALP activity of the groups was calculated by normalizing the amounts of ALP to DNA. Samples that have not interacted with HA groups and cultivated with cultivation media were used as negative control, while samples that have not interacted with HA groups and cultivated with osteogenic differentiation media were used as positive controls. Wells that have not been seeded with cells and interacted with HA groups were used as blanks. To determine the ALP and DNA amounts, cells were lysed with 300 µL of 0.1 M carbonate buffer with pH 10.0, followed by freeze-thawing. Following, lysates were collected as supernatant after centrifugation at 14000 rpm for 5 minutes. ALP activity colorimetric assay kit was used, according to manufacturer's protocol, (Yang et al., 2012). The standard curve was generated with p-nitrophenol within the kit (0.48-2.40 µmol Appendix D). DNA amount was assessed by mixing 50 µL of cell lysate with 50 µL of PicoGreen solution. The PicoGreen solution was prepared by diluting PicoGreen dye 1:100 with TE buffer containing 10 mM Tris and 1 mM EDTA with a pH value of 8.00. Following,

fluorescence at 480 nm excitation and 538 nm emission was recorded. Amount of the DNA was calculated as aforesaid. Specific ALP activity was calculated as units of ALP per mg DNA per time (Singer et al., 1997).

In order to examine the osteogenic effect of the membrane groups, the amount of osteocalcin (OCN) in the cell was determined. Sterile and exosome incorporated periosteal membranes were placed in 48-well plates and seeded with hADSCs with a density of $5x10^3$ cells/well and cultivated in osteogenic media for 14 days. Amount of extracellular OCN was determined with an ELISA kit. OCN standard was used to prepare a calibration curve (1.25-80 ng/mL, Appendix E) (Mayr- Wohlfart et al., 2001).

PCR analysis was performed to examine the osteogenic effect of the periosteal membranes. Sterile samples were placed in 6-well cell culture dishes and cell seeding was carried out at $2x10^5$ cells/sample. Following cultivation with osteogenic media for 14 days, total RNA was isolated. Following RNA isolation, cDNA was synthesized and PCR reaction was performed (LightCycler® 48, Switzerland). Expressions of *COL1A1* and *RUNX2* were determined in proportion to *ACTB* expression (Mayr- Wohlfart et al., 2001). Sequence of the primers for *ACTB, COL1A1* and *RUNX2* are given in Table 2.4.

Table 2.4 Forward (F) and reverse (R) primers for *ACTB, COL1A1* and *RUNX2*.

Gene	*Primer*	*Sequence (5'→3')*
ACTB	F	CACCATTGGCAATGAGCGGTTC
	R	AGGTCTTTGCGGATGTCCACGT
COL1A	F	GATTCCCTGGACCTAAAGGTGC
	R	AGCCTCTCCATCTTTGCCAGCA
RUNX2	F	CCCAGTATGAGAGTAGGTGTCC
	R	GGGTAAGACTGGTCATAGGACC

2.2.3.7 Immunomodulation

Effect of F/sA ratio on immunomodulation was investigated by using THP-1 monocytes. For this purpose, first, monocytes were differentiated into macrophages by incubation with 50 ng/mL PMA for 48 hours. Differentiated macrophages were detached from the cell culture dish by trypsinization and seeded on samples or TCPS with a density of $1x10^5$ cells/well in 48-well plates. After 24 h of incubation, cells were treated with either 100 μg/mL LPS or 5mM ATP and incubated for an additional 24 h. Amounts of IL1B (7.8-500 pg/mL, Appendix F) and CASP1 (1.56-100 ng/mL, Appendix G) was assessed with ELISA for LPS and ATP treated samples, respectively (Park et al., 2007; He, Hara & Núñez, 2016). Amounts of CASP1 and IL1B were normalized to DNA, which was quantified with PicoGreen dye as aforesaid.

Immunomodulatory properties of F/sA membranes loaded with F12, HA, 8B HA and 8B 4Zn HA exosomes were investigated with amounts of CASP1 and IL1B by using THP-1 monocytes, as aforesaid. Differently, for PCR, cells were seeded on samples or TCPS with a density of $1x10^6$ cells/well in 6-well plates. Expressions of *CASP1* and *IL1B* were determined for ATP treated cells whereas expressions of *NFKB* and *IL10* were determined for LPS treated cells (He, Hara & Núñez, 2016; Park et al., 2007). Sequence of the primers for *RPL13*, *CASP1*, *IL1B*, *NFKB* and *IL10* are given in Table 2.5.

Table 2.5 Forward (F) and reverse (R) primers for *RPL13*, *CASP1*, *IL1B*, *NFKB* and *IL10.*

Gene	*Primer*	*Sequence (5'→3')*
RPL13	F	CGCTCCAAACTCATCCTCTTC
	R	CTCTTCCTCAGTGATGACTCGAG
CASP1	F	GCTGAGGTTGACATCACAGGCA
	R	TGTCTGTCAGAGGTCTTGTGCTC
IL1B	F	CCACAGACCTTCCAGGAGAATG
	R	GTGCAGTTCAGTGATCGTACAGG
NFKB	F	GCAGCACTACTTCTTGACCACC
	R	TCTGCTCCTGAGCATTGACGTC
IL10	F	CATCAAGGCGCATGTGAACTC
	R	AATCGATGACAGCGCCGTAG

2.2.3.8 Angiogenesis

Effect of ions released from synthesized HA groups on angiogenesis was assessed with *in vitro* tube formation assay. For this purpose, 96-well plates were covered with 50 µL of Matrigel®. After 30 min of incubation in 37°C, HUVECs were seeded on Matrigel®, with a density of $1x10^4$ cells/cm^2. Cells were cultivated in 0.5 mg/mL extracts of HA groups in vascular cell basal medium. Vascular cell basal medium was used as negative control whereas vascular cell basal medium supplemented with vascular endothelial cell growth kit was used as positive control. After 4 h of cultivation, media were removed and cells were stained with 20 mM Calcein AM. Samples were imaged with fluorescence microscope at 495 nm excitation and 515 nm emission (Kelley et al., 2022). Obtained images were analyzed using AngioTool (NIH, USA). Junction density, vessel area and total vessel length were calculated by using the software (Zudaire et al., 2011). Amount of VEGFA in HUVECs treated with HA extracts was determined by ELISA. For this purpose, cells were seeded and

treated as aforementioned. Total VEGFA in samples was determined with an ELISA kit, according to manufacturer's protocol (31.25-2000 pg/mL, Appendix H).

Effect of F/sA membranes loaded with F12, HA, 8B HA and 8B 4Zn HA exosomes on angiogenesis was investigated by using HUVECs as well. *In vitro* tube formation and VEGFA ELISA were carried out as aforesaid. For gene expression analyses, cells seeded on TCPS were used as control. Sterile samples were placed in 6-well plates and cell seeding was performed with a density of $1x10^6$ cells/well. Total RNA was isolated after 3 days of cultivation. Relative expressions of *NOS3* and *VEGFA* were determined by using *ACTB* as a housekeeping gene (Murohara et al., 1998). Sequence of the primers for *NOS3* and *VEGFA* are given in Table 2.6.

Table 2.6 Forward (F) and reverse (R) primers for *NOS3* and *VEGFA*.

Gene	*Primer*	*Sequence (5'→3')*
NOS3	F	ACCAGCACATTTGGGAATGG
	R	TCTGAGCAGGAGATGCTGTTG
VEGFA	F	TCACCATGCAGATTATGCGGA
	R	CACGCTCCAGGACTTATACCG

2.2.4 Statistical Analysis

One-way analysis of variance (ANOVA) was used to determine significant differences between groups whereas Tukey's Test was used to compare means (SPSS-26 Software, SPPS Inc., USA). Single asterisk (*) was used to refer statistical significance between groups. Double and triple asterisks were used denote significantly the highest and the lowest groups at the given time point, respectively.

CHAPTER 3

RESULTS AND DISCUSSION

3.1 Characterization of B-Doped HA Groups

B-doped HA groups with 1, 2 4 and 8 mol% dopant ratios were synthesized with microwave assisted wet precipitation method. Obtained HA groups were characterized in terms of morphology, microstructure, phase purity, elemental composition and cytotoxicity. Optimal B dopant ratio was used as the starting point for B and Zn co-doped HA.

3.1.1 SEM Imaging

Morphology of the HA groups was investigated by SEM imaging (Figure 3.1). It was observed that HA groups had round grains. It was reported that for HA, 10% B doping resulted in fused grains, due to disruption of the structure, which was more than the HA groups (Pazarceviren et al., 2021).

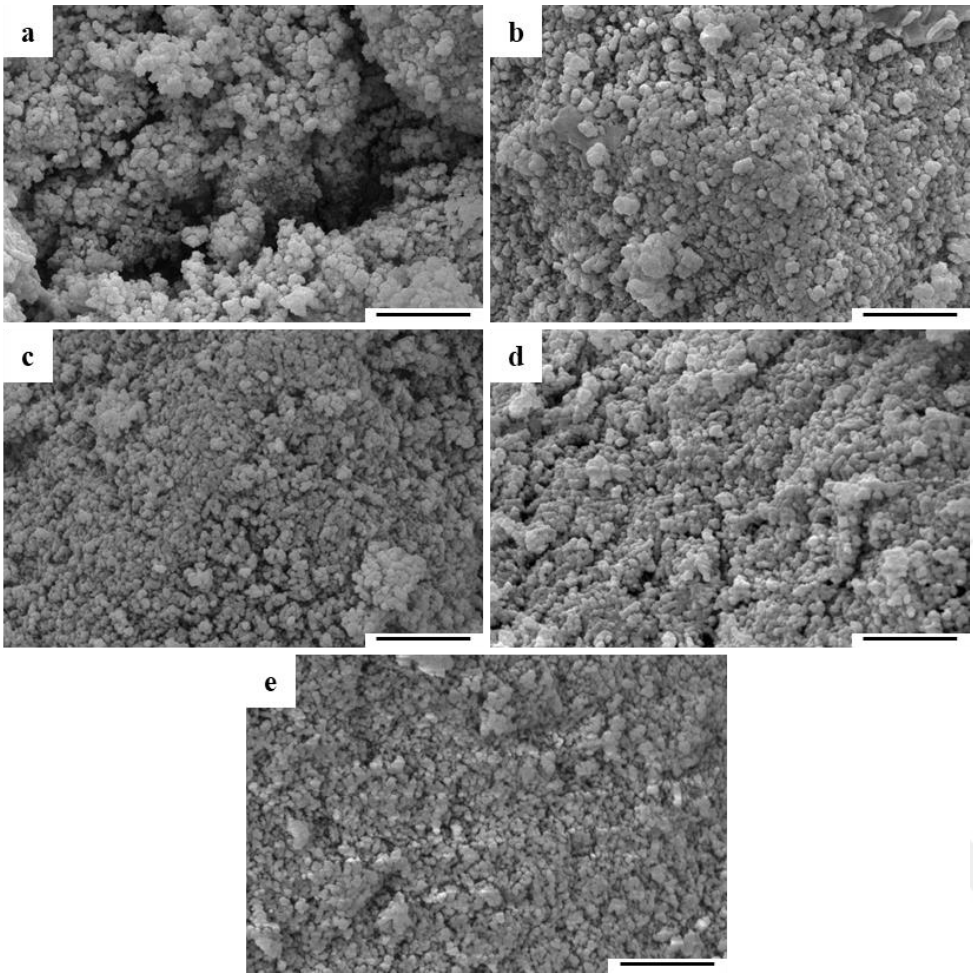

Figure 3.1. SEM images of a) HA, b) 1B HA, c) 2B HA, d) 4B HA and e) 8B HA groups (Magnification 80,000X, scale bar: 1 μm).

3.1.2 XRD Analysis

Effect of boron on HA content, crystallinity percentage and crystallite size were determined with XRD analysis. Data were analyzed according to International Centre for Diffraction Data (ICCD) card 98-001-6742. XRD spectra, HA content, crystallinity percentage and crystallite size of H and B-doped HA groups are given in Figure 3.1. It was found that HA phase percentage was not affected by B-doping. However, B-doping led to decrease in crystallinity and crystallite size. In a study, HA percentage of boron-doped HA groups sintered at 1100°C was stated to increase

for groups containing more than 1% B. On the contrary, crystallinity and crystallite size were reported to be independent of B-doping (Pazarçeviren et al., 2021). It was also stated that phase composition is affected by sintering temperature and sintering temperature values over 1350°C yield other phases such as tetracalcium phosphate, α-tricalcium phosphate, β-tricalcium phosphate, and calcium oxide. Grain size and crystallinity were also reported to increase with increase in the sintering temperature (Muralithran & Ramesh, 2000). Another study reported that sintering above 700°C results in decreasing HA content (Hayakawa et al., 2008). Considering given information, non-significant HA% change and decrease in crystallinity and crystallite size were attributed to low sintering temperature.

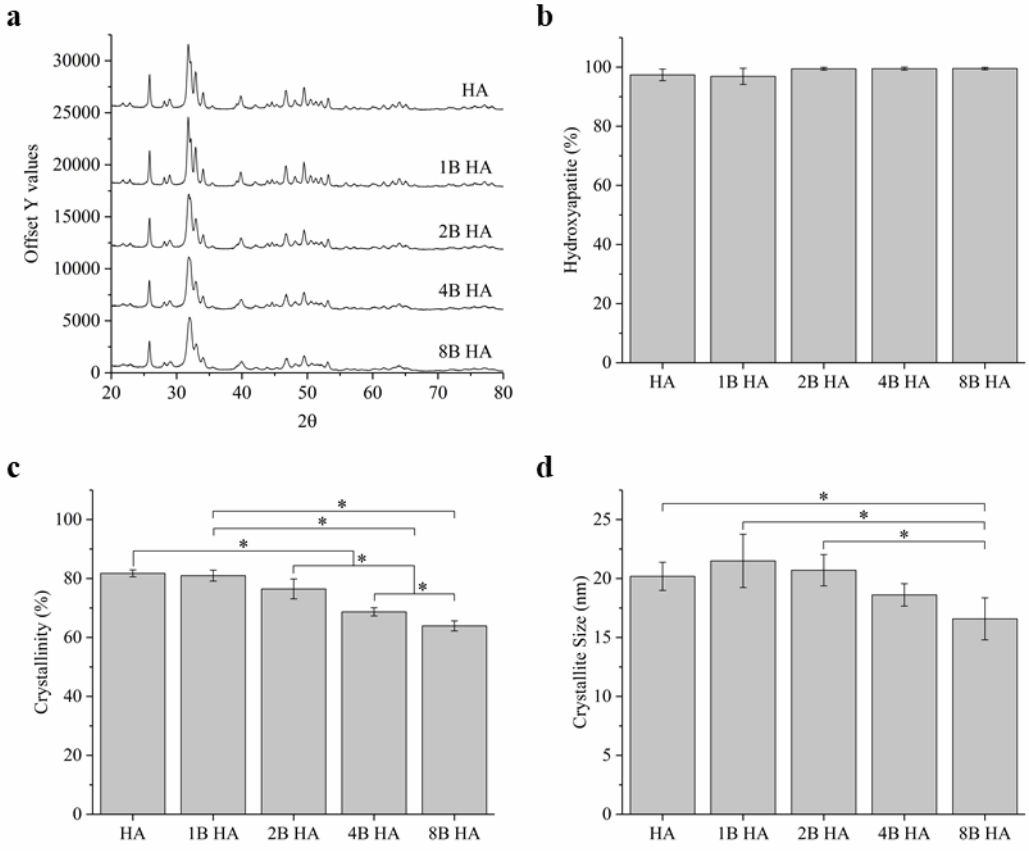

Figure 3.2. a) XRD spectra, b) hydroxyapatite phase percentage, c) crystallinity percentage and d) crystallite size of HA and B-doped HA groups (n=3, $p<0.05$). Asterisk refers statistical differences between the groups.

3.1.3 FTIR Analysis

FTIR analysis performed in the preliminary studies was repeated twice more for different batches of each group, in order to confirm the presence of the functional groups. FTIR spectra of HA and B-doped HA groups are given in Figure 3.3. The presence of PO_4^{3-} was confirmed with the bands around 1089, 1024, 962, 630, 600 and 561 cm^{-1} (Albayrak, 2016). It was also observed that intensity of PO_4^{3-} bands at 1089, 962, 630 and 600 cm^{-1} decreased with increasing B content. Loss of intensity of PO_4^{3-} bands was expected since B is incorporated into HA structure by replacing PO_4^{3-} (Uysal, Yılmaz & Evis, 2020). In a study subjecting B-doped HA sintered at 1100°C, BO_2^- bands were reported to be around 2002 and 1935 cm^{-1}, while BO_3^{3-} bands were determined at 1244, 1205, 783 and 743 cm^{-1} (Baykal et al., 2004). It was noticed that there were no bands at the mentioned wavenumbers. Absence of the reported bands may be due to different sintering temperature. It is also worth mentioning that B containing groups had 2 different bands different than HA group at 2360 and 2341 cm^{-1}, whose intensities increased with increasing B ratio. In a study, band around 2343 $cm^{-1}$was attributed to C-O bond of carbonated hydroxyapatite (Sun et al., 2006). However, in the present case, the signal was only present in the doped groups. It was also reported that B-O can also yield peaks around the same wavenumber, which can explain why increase in B and caused increasing band intensity (Zhang et al., 2020).

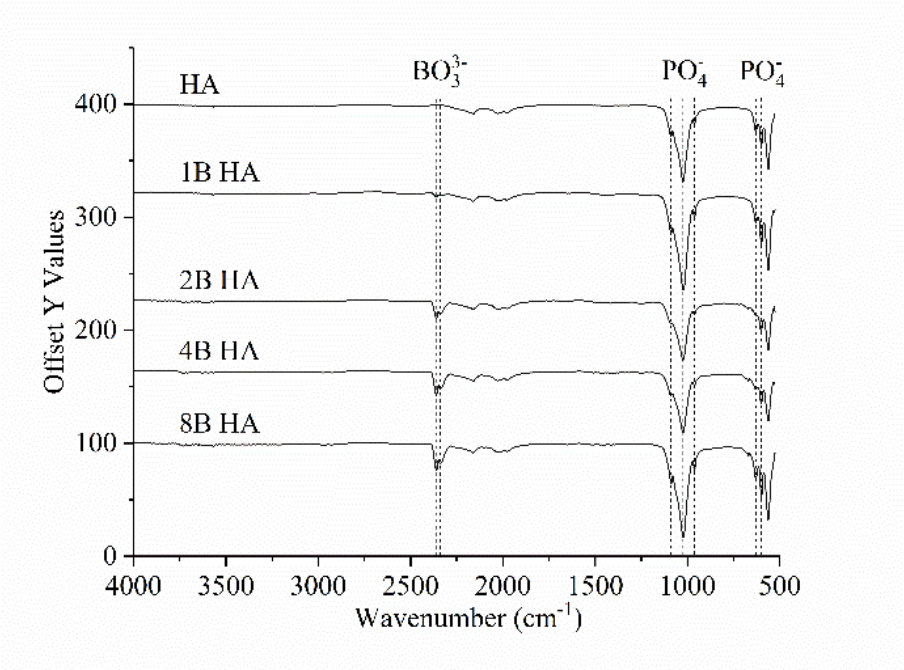

Figure 3.3. FTIR spectra of HA and B-doped HA groups.

3.1.4 Particle Size Measurement

Particle size of HA groups was measured due to their potential to effect ion release and consequently cell response (Fathi, Hanifi, & Mortazavi, 2008). Mean particle size of HA and B-doped HA groups are given in Figure 3.4. Particle size measurement revealed that B doping significantly decreased particle size. It was also found that the mean particle size of 4B HA and 8B HA groups was significantly higher than that of 1B HA and 2B HA groups. In a study done by Pazarceviren et al. (2020), 5% B doping was reported to decrease the particle size of HA groups sintered at 1100°C. Average particle size of the HA group was found to be around 35 μm, which is larger than present results. Particle size is stated to be affected by sintering temperature. Higher sintering temperatures were reported to yield larger particles, which may be the result of significant decrease at even lower dopant ratios and overall smaller size of the particles (Juang & Hon, 1996).

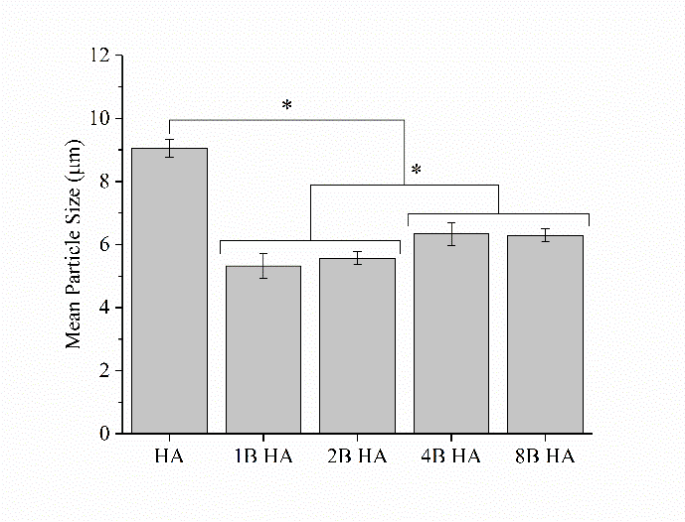

Figure 3.4. Mean particle size of HA and B-doped HA groups (n=3, $p<0.05$). Asterisk is used to refer statistical significance between the groups.

3.1.5 Elemental Analysis

HA groups were subjected to ICP-OES analysis to determine their elemental content. (Ca)/(P+B) ratios and mole percentages of Ca, P and B belonging to HA groups are given in Table 3.1. The analysis revealed that, about half of the B used during synthesis was incorporated into structure of HA, for all groups. It was also noticed that obtained (Ca)/(P+B) ratio of HA group was similar to theoretical ratio 1.67, used during synthesis. Moreover, compared to HA group, (Ca)/(P+B) ratio significantly decreased with B addition more than 2%.

Table 3.1 B mol percentages and Ca/(P+B) molar ratios of HA and B-doped HA groups (n=3, $p<0.05$).

Group	*B (mol %)*	*Ca/(P+B)*
HA	-	1.68 ± 0.0.3
1B HA	0.79 ± 0.03	1.63 ± 0.08
2B HA	1.39 ± 0.04	1.67 ± 0.05
4B HA	2.21 ± 0.05	1.54 ± 0.05[a]
8B HA	4.43 ± 0.09	1.58 ± 0.03[a]

(B ratio significantly increased as the doping amount was increased, from HA to 8B HA. [a] refers significant differences compared to HA group. (Ca)/(P+B) ratio of HA group was significantly higher than that of 4B HA and 8B HA)

3.1.6 *In Vitro* Cytotoxicity Test

Highest HA concentration that would not affect cell viability was determined with MTT assay, in order to determine treatment concentration of hADSCs for exosome isolation (Figure 3.5a). MTT assay after 48 hours of cultivation of hADSCs with varying concentrations of HA showed that treatment concentrations more than 0.5 mg/mL led to significant decrease in cell viability. In a study, cytotoxicity of HA and Ag-doped HA obtained from limestone by precipitation was investigated with MTT assay. It was reported that up to 0.2 mg/mL HA and 2.5% Ag-doped HA did not show cytotoxicity against MC-3T3 pre-osteoblast cells. However, 5% Ag-doped HA was stated to reduce cell viability, at the same concentration (Siriat et al., 2022). Considering the possible effect of dopants on cell viability and osteogenic differentiation, 0.5 mg/mL was chosen as the treatment concentration for the rest of the study. Percent cell viability of treated hADSCs cells relative to untreated cells is given in Figure 3.5b. It was found that viability of cells treated with 50 mg/mL 4B HA and 8B HA was significantly lower than that of cells treated with 50 mg/mL HA. Like viable cells, apoptotic cells release exosomes as well. Their exosomes were stated to carry miRNA, organelles and nuclear fragments (Kakarla et al., 2020).

Unlike the ones from healthy cells, exosomes derived from dying cells can elicit immune response (Park et al., 2018). Therefore, the group 8B HA, which did not significantly alter cell viability, was chosen as the safe group with the highest B content. Further studies for deciding the optimal HA group to be used to collect exosomes were conducted via synthesis of groups with 8 mol% B and varying ratios of Zn dopant.

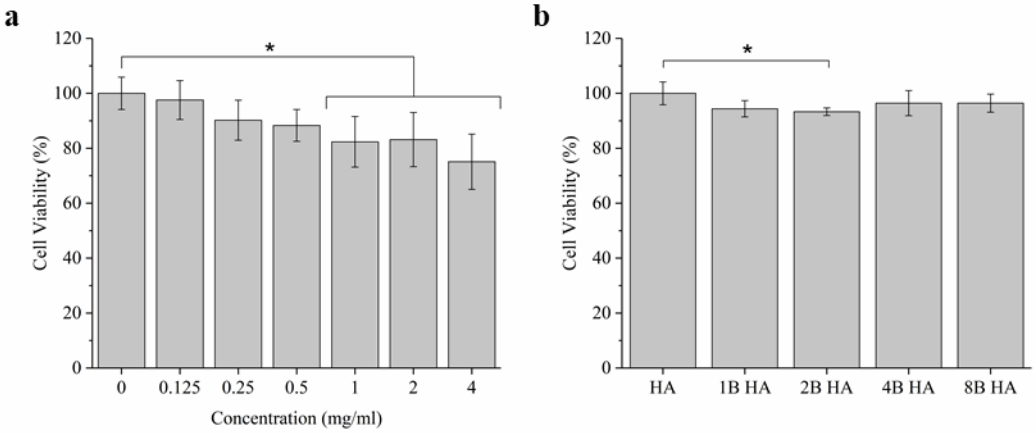

Figure 3.5. a) Viability of cells seeded on TCPS and treated with a) different amounts of HA for 24h (n=5, $p<0.05$) b) 0.5 mg/ml of HA and B-doped HA extracts for 24h (n=4, $p<0.05$). Viability of untreated cells seeded on TCPS was considered 100%. Asterisk refers statistical significance between the groups.

3.2 Characterization of B and Zn- Doped HA Groups

HA groups with 8 mol% B and 1, 2 4 and 8 mol% Zn ratios were synthesized with microwave assisted wet precipitation method. Obtained HA groups were characterized in terms of morphology, microstructure, phase purity, elemental composition, ion release profile and cytotoxicity.

3.2.1 SEM Imaging

Morphology of the HA groups was investigated by SEM examination (Figure 3.6). It was observed that HA group had round and larger grains, whereas doped HA groups had smaller and fused grains. It was also noticed that doping resulted in irregularly shaped grains. Similar to obtained data, it was reported that for HA, 10% B doping resulted in fused grains, due to disruption of the structure (Pazarceviren et al., 2021). Concordantly, it was also stated that 10% Zn containing HA sintered at 1000°C resulted in fused grains (Ofudje et al., 2019).

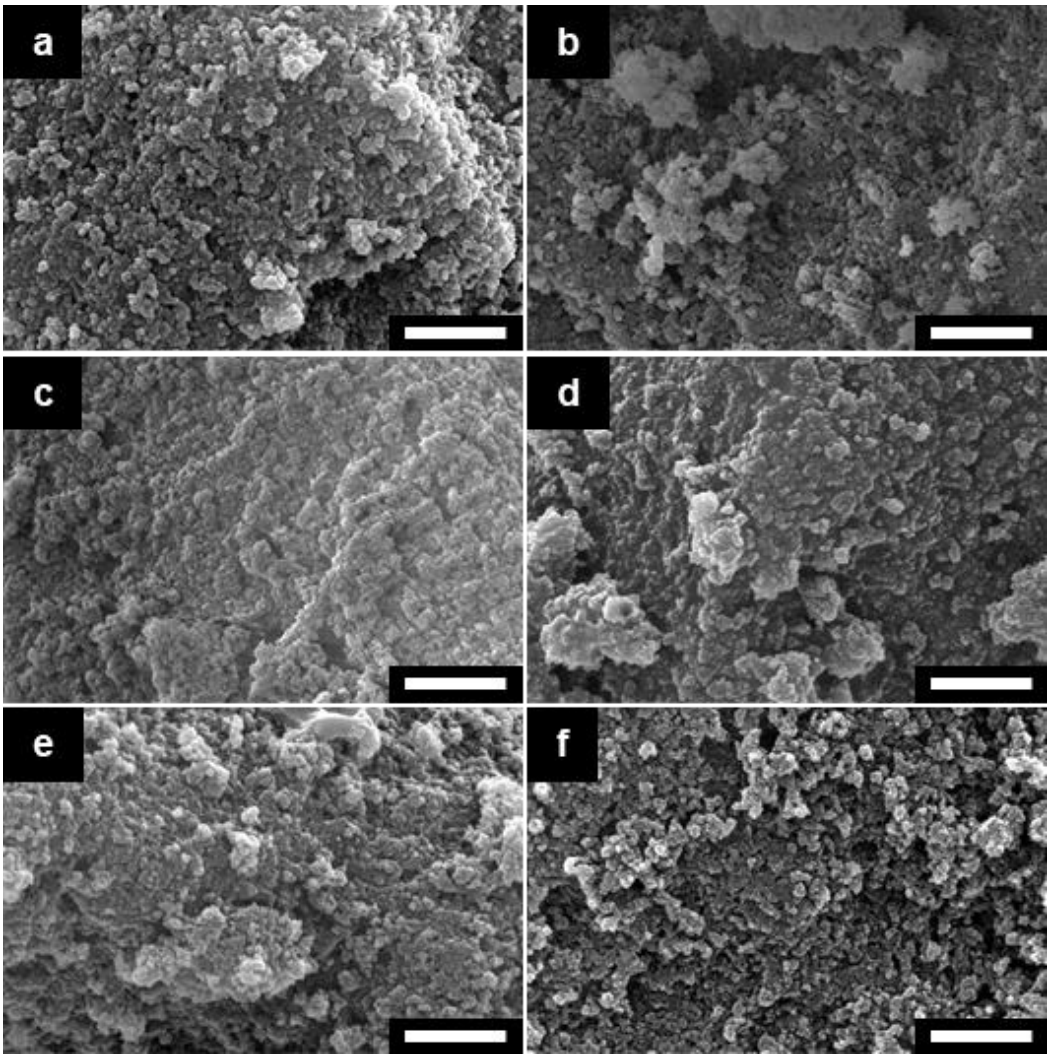

Figure 3.6. SEM images of a) HA, b) 8B HA, c) 8B 1Zn HA, d) 8B 2Zn HA, e) 8B 4Zn HA, f) 8B 8Zn HA groups (80,000X, Scale bar: 1µm).

3.2.2 Particle Size Measurement

Particle size of HA groups was measured due to their potential effect on the ion release and consequently cell response (Fathi, Hanifi, & Mortazavi, 2008) (Figure 3.7). Particle size measurement revealed that 8% B doping significantly decreased particle size. In a study done by Pazarceviren et al. (2021), 5% B doping was reported to decrease the particle size of HA groups sintered at 1100°C. It is also worth mentioning that average particle size of the HA group was found to be around 35

μm, which is larger than present results. Particle size is stated to be affected by sintering temperature. Higher sintering temperatures were reported to yield larger particles, which may be the result of significant decrease at even lower dopant ratios and overall smaller size of the particles (Juang & Hon, 1996). On the other hand, Zn dopant led to increasing particle size trend. It was found that although initial 1% Zn doping led to significantly smaller particle size, compared to that of 8B HA. Particle size of 8B 8Zn HA group was significantly higher than that of other co-doped groups. A study subjecting Fe & Zn-doped HA revealed that around 12% dopant resulted in significantly smaller particle size (Ramya et al., 2014). Accordingly, in the present study, HA groups equal or less than 12% of total dopants led to smaller particle size.

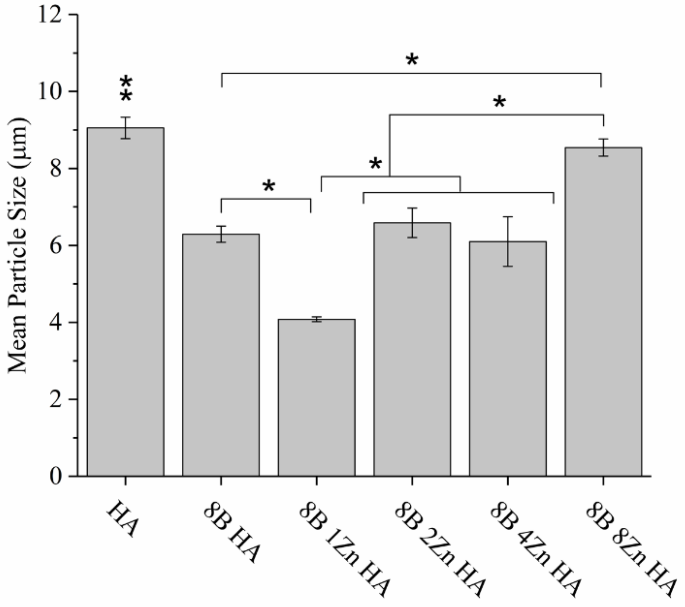

Figure 3.7. Mean particle size of HA groups (n=3, $p<0.05$). Single asterisk is used to refer statistical significance between the groups whereas double asterisk denotes significantly the highest group.

3.2.3 Elemental Analysis

Presence of incorporated dopants in HA groups was investigated with ICP-OES (Figure 3.8). It was found that incorporation of dopants significantly decreased (Ca+Zn)/(P+B) ratio. (Ca+Zn)/(P+B) ratio for HA was 1.68±0.04 which was close to the theoretical ratio. It was also noted that 8B 8Zn HA group had significantly the lowest (Ca+Zn)/(P+B) ratio (1.50±0.02), which was lower than the theoretical value. Concordantly, previous studies stated that incorporation of Zn into HA decreased the (Ca+Zn)/(P+B) ratio, due to formation of other phases (Alioui et al., 2019; Stanic et al., 2010). Elemental analysis also revealed that incorporation of B into HA structure was 5.14±0.28% for 8B HA group. Previous literature also reports that incorporation of B into HA with wet synthesis is around half of the theoretical ratio (Jodati et al., 2023; Pazarceviren et al., 2021). It was mentioned that B replaces PO_4^{3-} in the form of orthoborate and OH in the form of both orthoborate and metaborate, which makes maximum calculated B-doping to be around 4.56% (Ternane et al., 2002). Low incorporation of B into HA was also associated with wet synthesis route, due to of B source being washed out (Kolman et al., 2017). Addition of Zn was found to significantly decrease B percentage, with 8B 8Zn HA group having the significantly lowest B content (2.07±0.0.02%). Decreasing B percentage in bi-doped HA was attributed to wet synthesis as well, since incorporation of B was reported to occur on hydrated surface of the apatite (Cacciotti, 2018). Molar percentages of Zn were found as 1.13±0.03, 2.20±0.12, 5.01±0.18 and 9.76±0.16 for 8B 1Zn HA, 8B 2Zn HA, 8B 4Zn HA and 8B 8Zn HA groups, respectively. It was revealed that Zn was incorporated into HA, effectively. In a study, Zn-doped HA was synthesized with wet precipitation method, with slightly more incorporation percentage than the theoretical value, as well (Stanic et al., 2010; Alioui et al., 2019).

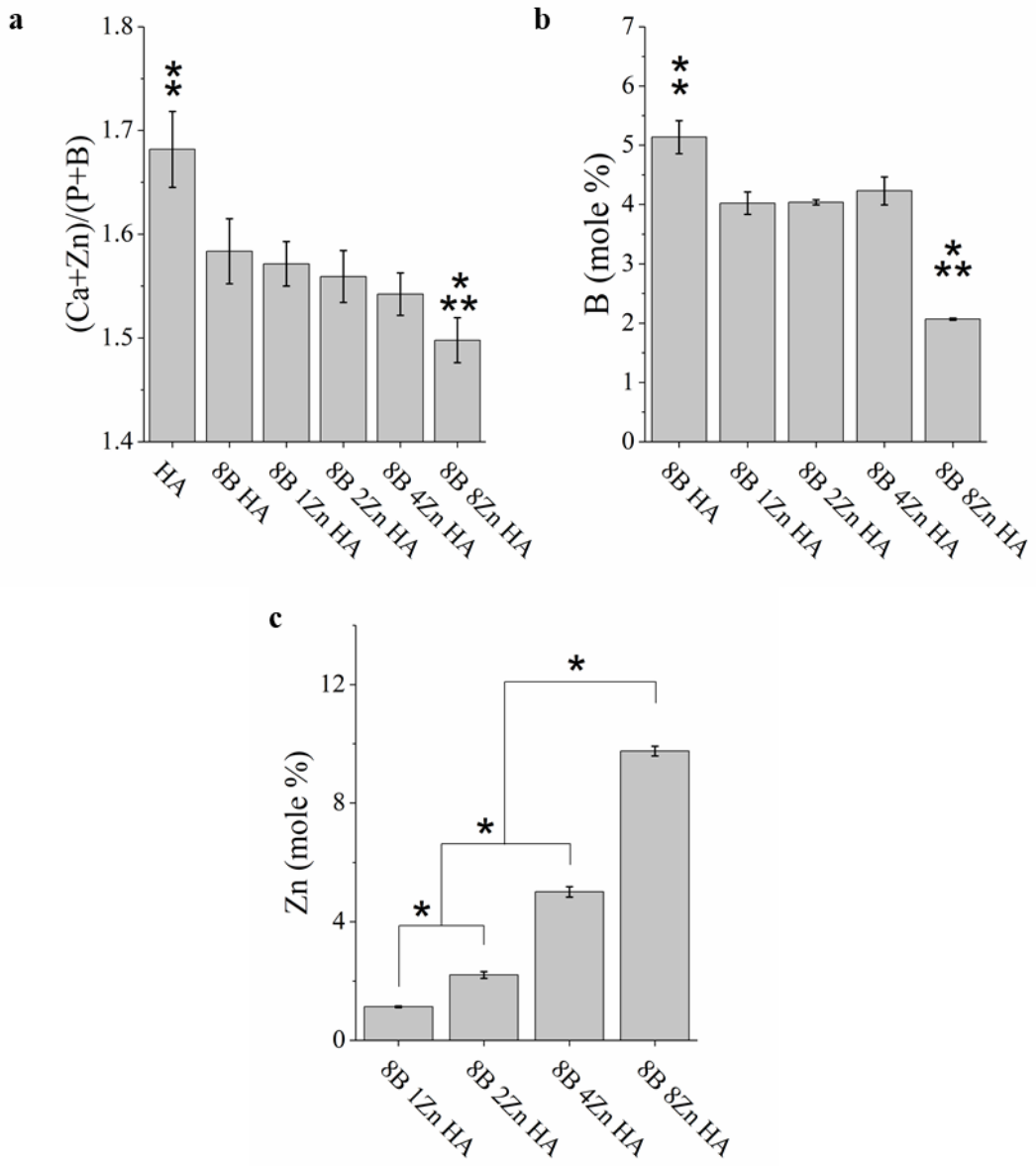

Figure 3.8. Ca/P mole ratios (a), and B (b) and Zn (c) mole percentages of HA groups determined with ICP-OES (n=3, $p<0.05$). Single asterisk refers statistical significance between the groups. Double and triple asterisk denote significantly the highest and the lowest groups, respectively.

3.2.4 FTIR Analysis

In order to examine the changes of intensities of functional groups due to B and Zn doping, FTIR analysis was performed (Figure 3.9). Concordant with a reported study, presence of PO_4^{3-} was confirmed with the bands around 1089, 1024, 962, 630, 600 and 561 cm^{-1} (Albayrak, 2016). Intensities of PO_4^{3-} bands at 1089, 962, 630 and 600 cm^{-1} were found to decrease with increasing Zn ratio. This finding was not expected as Zn is expected to replace Ca in the HA structure (van Rijt et al., 2021). However, it was reported that Zn incorporation can result in decreasing HA phase, which may be responsible from decreasing intensities of PO_4^{3-} bands (Naqshbandi et al., 2014). In a study, the band around 2337 cm^{-1} was referred to Z-O bond of ZnO nanoparticles (Norouzzadeh et al., 2020). It was also reported that B-O can also yield bands around the same wavenumber (Zhang et al., 2020). Therefore, it can be concluded that bands at 2360 and 2341 cm^{-1} can be attributed to B-O and Zn-O bonds. Phase composition of HA was known to effect biological effects of HA (Uysal et al., 2020).

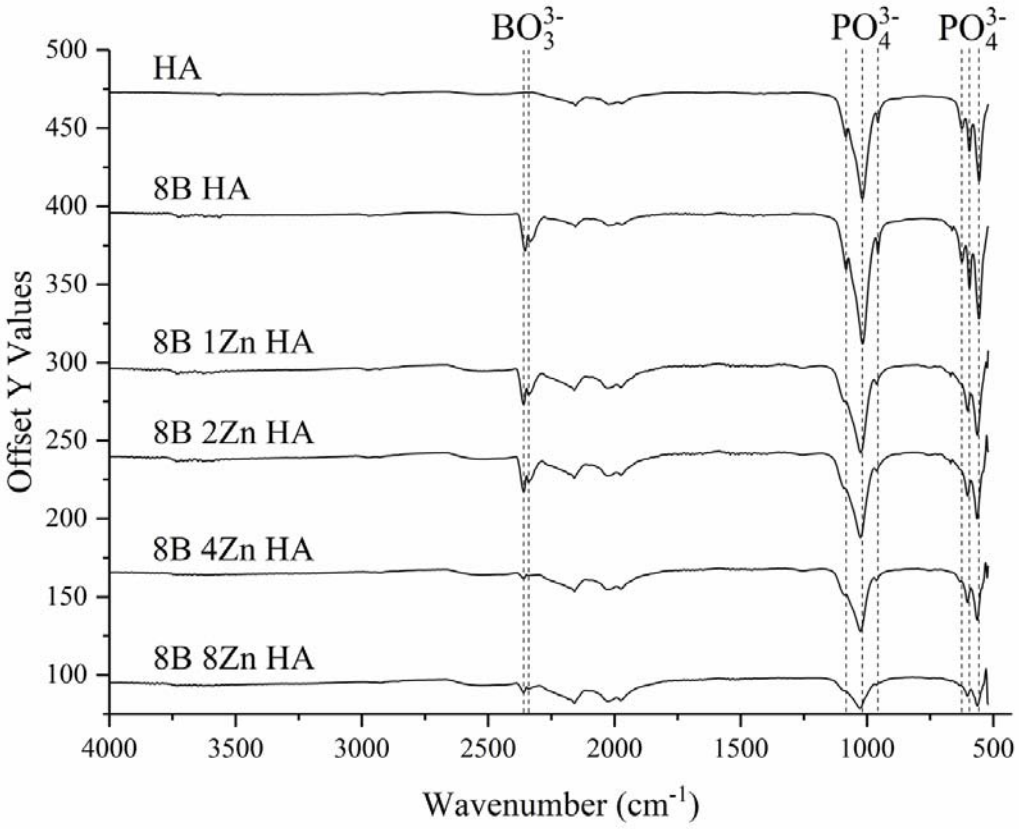

Figure 3.9. FTIR spectra of HA groups.

3.2.5 XRD Analysis

Structure of HA groups was investigated with XRD analysis (Figure 3.10). XRD spectra of the HA groups revealed that intensity of the peaks decreased whereas their width increased, which translated into structural differences between groups. It was determined that HA group had the highest HA percentage (94.37±1.93%), indicating that B-doping led to a significant decrease in HA phase percentage for all groups. B-doping was reported to decrease HA percentage due to formation of other phases such as β-TCP, CaO and borates (Ternane et al., 2002). In this case, apart from HA, β-TCP phase was observed. It was also found that compared to both HA and 8B HA, HA phase percentages of 8B 4Zn HA (84.43±0.50%) and 8B 8Zn HA (76.6±0.6%) groups were significantly lower, indicating higher Zn dopant concentrations led to a

decrease in the HA phase ratio. In a study, it was reported that 10 mol% Zn-doped HA sprayed with plasma had 4.8% HA whereas there was no HA phase in 15 mol% Zn doped HA. It was stated that increasing Zn dopant resulted in formation of other phases such as α-TCP and β-TCP (Candidato Jr. et al., 2018). In terms of crystallinity, it was found that crystallinity of HA group (90.43±2.84%) was significantly higher than that of 8B HA group (81.95±1.39%). It was mentioned that HA synthesized by wet method result in merging and broadening of the peaks, resulting in lowered crystallinity (Kolmas et al., 2017). Additionally, there was no significant difference between crystallinity percentage of 8B HA and Zn doped groups. However, crystallinity of 8B 2Zn HA (84.93±1.42%), 8B 4Zn HA (81.21±0.48%) and 8B 4Zn HA (76.11±4.94%) groups was significantly lower than that of HA group. There was also a significant difference between crystallinity of 8B 2Zn HA and 8B 8Zn HA groups.

In a study, Zn doped HA with Zn mol % ranging between 1-4 % was synthesized. Increasing Zn was shown to decrease crystallinity ratio, which was explained by disruption of the crystal structure due to size difference between Ca and Zn atoms (Kaygili & Tatar, 2012). Overall, it can be said that increasing Zn resulted in a slight decrease in crystallinity percentage, yet the main effect was due to presence of B. Crystallite size was also affected by boron doping. It was noted that crystallite size of 8B HA group (145.67±4.93 nm) was significantly lower than that of HA (189.33±40.58 nm) group. It was mentioned that lower intensity and broadening of the peaks caused by B-doping resulted in smaller crystallite size of the synthesized HA (Jodati et al., 2022). Crystallite size was found to be affected by increasing Zn as well. Every increase in Zn ratio was noted to significantly decrease the crystallite size. In a previous study, it was mentioned that crystallite sizes of the 7 and 10 mol% Zn-doped HA were lower than that of HA, synthesized by wet precipitation method. The decrease was attributed to size difference of Ca and Zn atoms (Popa et al., 2016).

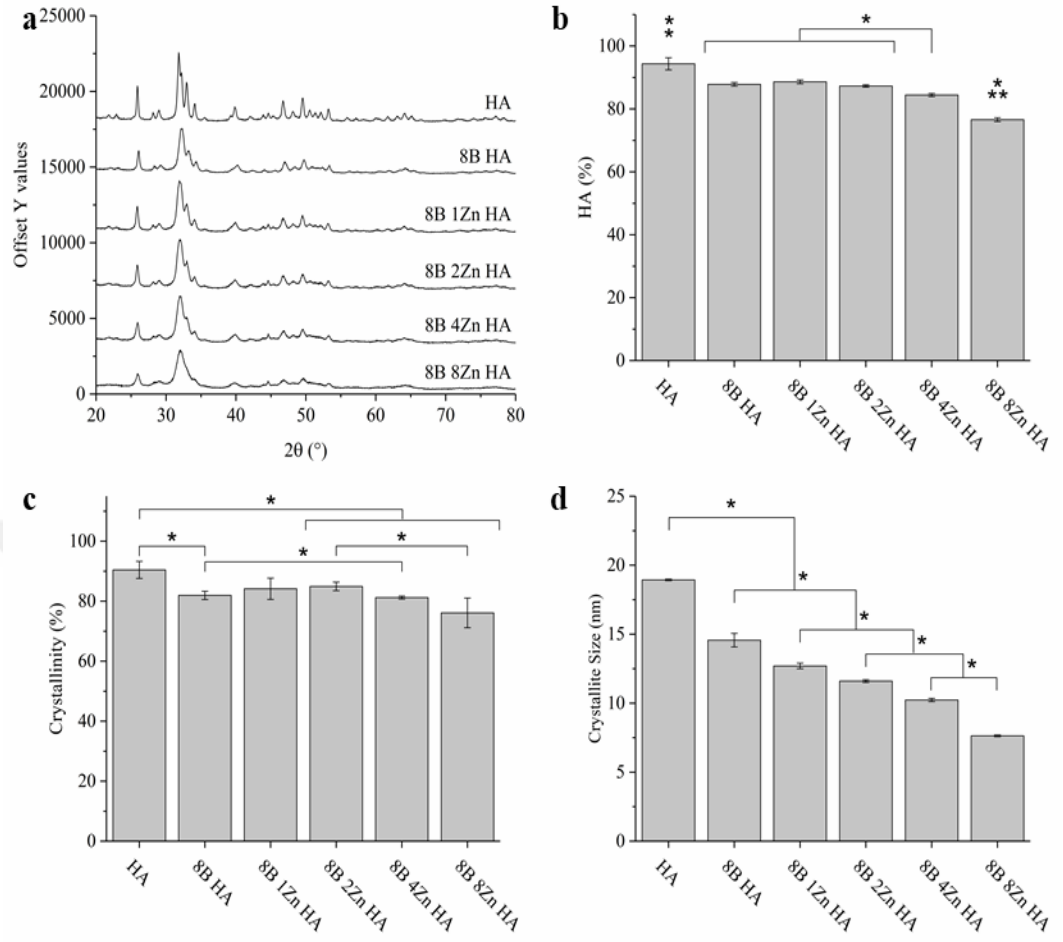

Figure 3.10. a) XRD spectra, b) HA ratio, c) crystallinity percentage and d) crystallite size of HA groups (n=3, p<0. 05). Single asterisk was used to refer statistical significance between groups. Double and triple asterisk were used denote significantly the highest and the lowest groups at the given time point, respectively.

3.2.6 Ion Release

Cumulative release of Ca^{+2}, PO_4^{3-}, BO_2^- and Zn^{2+} from HA groups was determined with ICP-OES (Figure 3.11). Ca release significantly increased from day 2 to day 7 for all groups. However, there was no significant change between days 7 and 14, except for 8B 4Zn HA (21.34±0.18 ppm at day 7) and 8B 8Zn HA (16.67±0.84 ppm at day 7) groups. Ca amount released from 8B HA group (104.22±3.40 ppm at day

14) was significantly higher than that of other groups, for every timepoint. Higher Ca release from 8B HA compared to HA was attributed to smaller size of the 8B HA particles which contributes to higher surface area (Pazarçeviren et al., 2021). It was also noted that Ca released from HA group (75.97±3.89 ppm at day 14) was significantly higher than that of 8B 1Zn HA (22.76±7.47 ppm at day 14), 8B 2Zn HA (24.93±7.29 ppm at day 14), 8B 4Zn HA (26.89±0.41 ppm at day 14) and 8B 8Zn HA (22.57±0.78 ppm at day 14), which was related to replacement of Ca by Zn in Zn-doped groups (Alioui et al., 2019). Cumulative P release significantly was the highest for HA on days 2 (1.28±0.48 ppm), 7 (3.92±0.63 ppm) and 14 (6.88±0.78 ppm). P release from 8B 1Zn HA samples was significantly higher than that of 8B HA and other Zn doped groups on days 7 (2.36±0.16 ppm) and 14 (2.48±0.16 ppm), indicating that presence of 1% Zn facilitated ion release. It was stated that co-doping can alter material's properties depending of substitution combination and ratio (Cacciotti, 2018). Accordingly, mean particle size of 8B 1Zn group was significantly lower than that of 8B HA group, which can result in higher P release.

It was also determined that 8B HA group released significantly higher B at days 2 (108.74±4.06 ppm), 7(148.33±3.68 ppm) and 14(175.06± 3.40 ppm). Lowest release was obtained from 8B 8Zn HA group at all timepoints (47.05±7.56 ppm at day 14). As aforesaid, incorporation of Zn significantly decreased B ratio present in HA groups, with the lowest B containing group being 8B 8Zn HA. Hence, the data correlated with release profile. In a previous study, 5 mol% B containing HA synthesized with wet precipitation and sintered at 1100°C was reported to release 10% of its B content, during 24h of incubation in cultivation media (Pazarçeviren et al., 2021). In the present study 8B HA group was found to contain approximately 55.27 mg B per g HA, which makes the released ratio approximately 3.93, 5.37 and 6.33% for days 2, 7 and 14, respectively. It was noted that sintering temperature alters Ca/P ratio and phases present in HA, which effects ion release (Chen et al., 2019). Zn release was similar for 8B 4Zn HA (0.22±0.03ppm at day 14) and 8B 8 Zn HA (0.29±0.02 ppm at day 14) groups except for day 14. Zn released from these groups were significantly higher than that of 8B 1Zn HA and 8B 2Zn HA groups, at

all timepoints. Notably, Zn released from 8B 8Zn HA group significantly increased at all timepoints, whereas 8B 2Zn HA (0.32±0.01 ppm at day 2) and 8B 4Zn HA (0.13±0.04 ppm at day 2) groups reached plateau at day 2. In a study, 5 and 10% Zn-doped HAs synthesized via wet precipitation and sintered at 1000°C were reported to release 1.434 and 2.012 mg/g Zn, after 5 days of incubation in PBS, which was higher than observed in the present data (Ofudje et al., 2019).

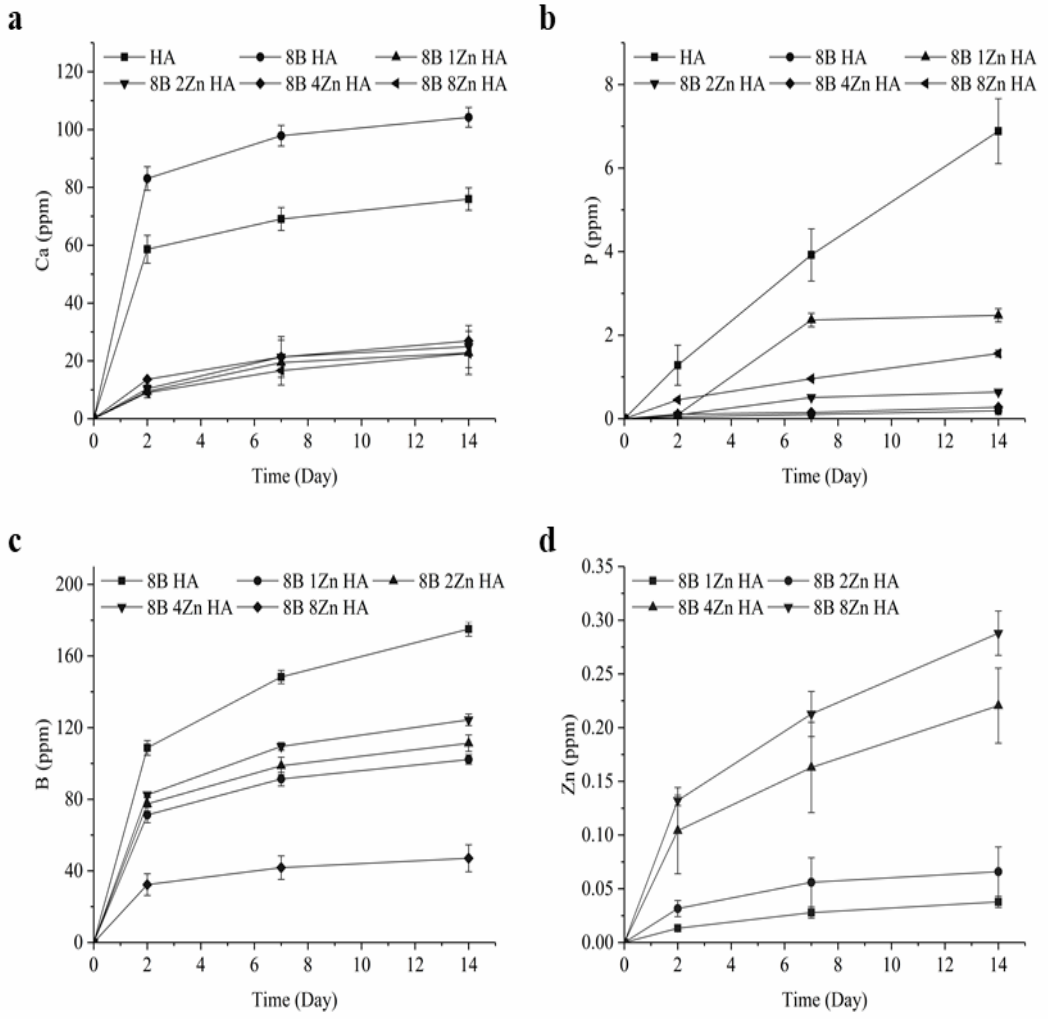

Figure 3.11. a) Ca, b) P, c) B and d) Zn released from HA groups, in dH_2O during 14 days of incubation at 37°C (n=3).

3.2.7 *In Vitro* Biomineralization

Effect of dopants on biomineralization was assessed by incubation of HA groups in SBF at 37°C (Figure 3.12). SEM images revealed presence of spherical CaP precipitate for all groups (Kim & Park, 2010). In addition to the precipitate layer throughout the surface of all samples, doped groups also had bud-like CaP precipitation. Abundance of CaP buddings were associated with presence of nucleation sites (Saddiqi, Patra & Seeger, 2017). It was also noticed that doped groups had cracked surface, which was associated with drying of thicker layer of CaP. Although grain size of the precipitates was similar, CaP layer on doped groups was more porous. In a study, it was reported that after 14 days of incubation in SBF, hardystonine/HA composite had more porous CaP precipitation, compared to pure HA. Porosity of the precipitate was associated with availability of more nucleation sites (Gheisari, Karamian & Abdellahi,2015). In a similar study, Zn doped HA coated titanium was reported to yield porous CaP precipitation, whereas HA coating resulted in dense precipitate. Difference in morphology was related to ions released by the pure and Zn-doped HA (Ding et al., 2014). Concordantly, Ca and P release from HA group was significantly higher than that of Zn-doped groups. Another study also found that dopants led to same morphological change in CaP precipitate. It was reported that CaP precipitation on HA was dense, whereas Na and Cl doped HA resulted in porous precipitate (Yoo et al., 2020). Similarly, it was observed that morphology of the precipitates was porous on day 14, for all doped groups. Hence, it was concluded that both B and Zn contributed to bioactivity.

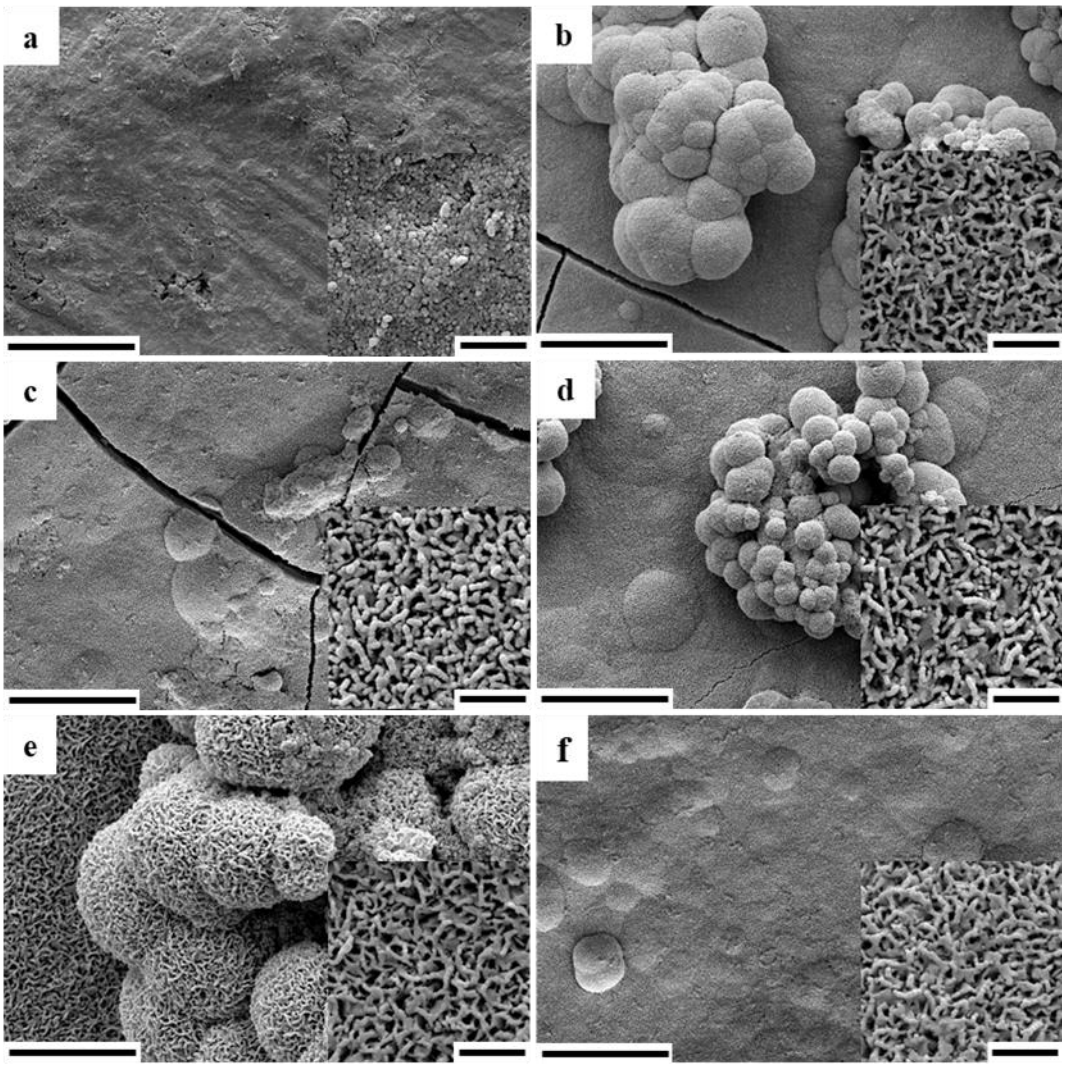

Figure 3.12. SEM images of a) HA, b) 8B HA, c) 8B 1Zn HA, d) 8B 2Zn HA, e) 8B 4Zn HA and f) 8B 1Zn HA discs immersed in SBF for 14 days (5000X and 80,000X (inset image). Outer scale bar: 20 μm, inset image scale bar: 1 μm).

3.2.8 Cell Viability and Proliferation

Effects of treatment with HA groups on cells during 14 days of incubation were investigated with Alamar blue assay (Figure 3.13a). Percent reduction of alamarBlue^{TM} indicates cell viability and increase in viability with time is interpreted as cell proliferation (Allen et al., 2022). On day 1, all groups had similar percent

reduction, except for 8B 8Zn HA group. On days 7, 10 and 14, viability of hADSCs treated with 8B HA, 8B 1Zn HA, 8B 2Zn HA and 8B 4Zn HA was significantly higher than that of untreated cells, indicating that 8% B and up to 4% Zn doping increased cell viability and proliferation. It was stated that 1 µg/mL B was found to be cytotoxic to human bone marrow stem cells (Ying et al., 2011). In the present study, highest B release was from 8B HA group (175.06±3.99 ppm, on day 14), which was less than 20% of the mentioned cytotoxic dose. B was also reported to be present in mineral part of the bone, acting as a trace element (Jugdaohsingh et al., 2015). Hence, effect of B on proliferation of hADSCs which can undergo osteogenic differentiation was considered as an important factor for bone tissue engineering (Grottkau & Lin, 2013). A previous study investigated the effect of HA and 0.3% B doped HA on viability of Wharton's jelly derived mesenchymal stem cells. Cells were treated with a density of 1 mg HA/3x10^3 cells. MTS and LDH tests were performed after 3 days of incubation. It was reported that both groups did not cause cytotoxicity as result of both tests (Kolman et al., 2017). In the present study, 2x10^3 cells were treated with 100 µl of 0.5 mg/ml HA groups, which was a lower treatment concentration. However, concentrations of the dopants were much higher.

In another study, effects of HA and up to 0.5 mol% B-doped HA discs on hFOBs were examined. It was stated that there was a significant increase of percent reduction of alamar blue on days 1 and 7 for all B-doped HA groups, compared to HA group. It was also mentioned that viability and proliferation of hFOBs seeded on 0.25 and 0.5 mol% B-doped HA discs were significantly higher than that of 0.05 and 0.1 mol%% B-doped HA discs concluding that B doping had potential to promote viability and proliferation (Jodati et al., 2022). In another study, viability of MC3T3-E1 cells seeded on chitosan, HA/chitosan composite and 1.15 wt% B-doped HA/chitosan composite scaffolds was investigated with MTT test. It was stated that B-doped HA incorporation into chitosan did not cause cytotoxicity, after 21 days of cultivation (Tuncay et al., 2017). In the present study, it was shown that B-doping with much higher concentration is capable of promoting viability and proliferation of hADSCs. It was also found that viability of cells treated with 8B 8Zn HA group

was significantly the lowest at all time points. Notably, Zn released from 8B 8Zn HA group was significantly higher than that of other groups, which probably led to toxicity. Overall, Zn-doping did not lead to increase in viability and proliferation of hADSCs, except for 8B 4Zn HA on day 4.

In a previous study, effects of a much lower dopant concentration were investigated. It was reported that 0.03125 mol% Zn-doped HA obtained with hydrothermal synthesis was non-cytotoxic against L929 fibroblasts after 24 hours of incubation with 0.4 mg/mL Zn-doped HA (Xiao et al., 2018). In the present study, much higher ratio of Zn doping was used. In a different study, effect of HA and 10 mol% Zn HA coating of Ti implants on 3-day viability of human osteoblasts was examined. Mentioned coatings were prepared via transition from monetite without sintering. Via DAPI stained nuclei counting, it was reported that both HA and 10 mol% Zn HA coatings led to significant decrease in cell viability, compared to TCPS. It was also mentioned that cell viability and proliferation of cells seeded on Zn HA coating was significantly higher than that of HA coating (Ortiz, 2016). Considering the aforesaid studies, it can be said that cytotoxicity of 8B 8Zn HA may arise from combinatorial effects of high concentration of both dopants. SEM images after 1 day of incubation revealed that cells were in contact with HA groups (Figure 3.13b-g). Additionally, it was seen that cells presented stem cell like and healthy morphology, except 8B 8Zn HA group. Cells treated with 8B 8Zn HA were rounder, indicating toxicity. It was reported that zeta potential of 0.1 mg/mL HA, varied between -10-15 mV, depending on particle size. It was also mentioned that decreasing particle size resulted in increasing zeta potential, which promoted attachment of HA particles to fibronectin present on cell surface (Wu et al., 2015). Hence, attachment of small HA particles onto cells were related to net charge of HA particles.

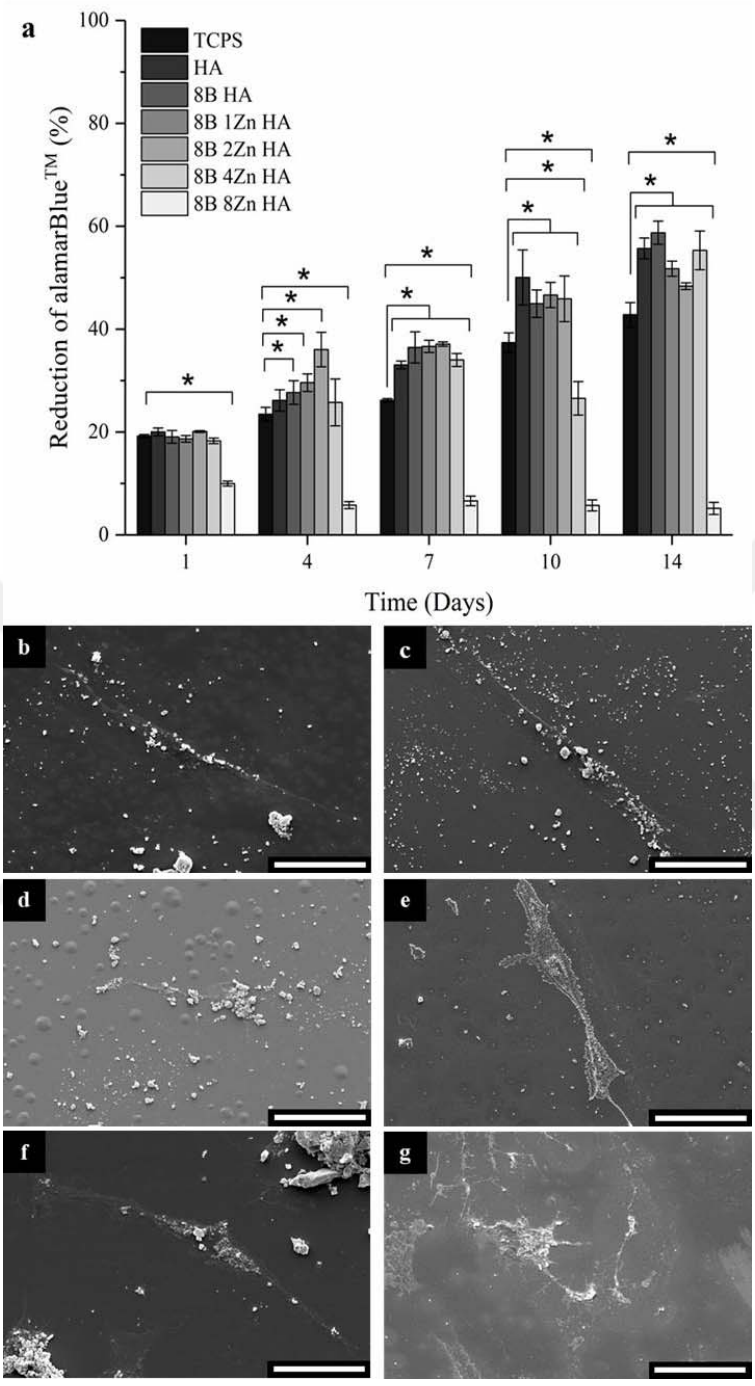

Figure 3.13. a) Percent reduction of alamarBlueTM by hADSCs cultivated in the presence of 0.5 mg/mL HA groups (n=4, $p<0.05$). SEM images of cells treated with b) HA, c) 8B HA, d) 8B 1Zn HA, e) 8B 2Zn HA, f) 8B 4Zn HA and g) 8B 8Zn HA groups, after 1 day of incubation (2000X, Scale bar: 50 μm). Asterisk denotes statistical significance between the groups.

3.2.9 Osteogenic Differentiation

Effect of HA groups on osteogenic differentiation of hADSCs was investigated with ALP assay. ALP activity was measured on days 7 and 14 (Figure 3.14). It was revealed that ALP activity of negative control group which was cultivated without osteogenic media was significantly lowest on both time points. On day 7, it was found that ALP activity of positive control was the highest. However, on day 14, it was found that ALP activity of 8B 4Zn HA group was significantly higher than that of other groups, including positive control group. It was mentioned that B-doped hydroxyapatite-loaded poly(butylene adipate-co-terephthalate) fibers increased expression of ALP, collagen and osteocalcin genes of human BMSCs (Arslan et al., 2018). In another study, it was stated that 0.01 and 0.1 ppm boric acid treatment significantly increased 7-day ALP activity and expression of osteogenic markers. It was also noted that 1 ppm boric acid led to significantly lower ALP activity compared to 0.01 and 0.1 ppm (Ying et al., 2011). Considering the aforesaid literature and ion release data, it was concluded that the osteogenic effect of B is concentration dependent.

ALP activity assay also revealed that on day 14, ALP activity of cells treated with 8B HA, 8B 1Zn HA 8B, 2Zn HA and 8B 8Zn HA groups was significantly lower than ALP activity of cells treated with 8B 4Zn group. Considering ion release and alamar blue assay together, lower ALP activity of 8B 8Zn group was attributed to cytotoxicity caused by high Zn release. It was also noted that there were no statistically significant differences between ALP activity of 8B HA, 8B 1Zn HA 8B and 2Zn HA groups, on day 14. Zn is mentioned as a cofactor for many enzymes, including ALP and collagenase which regulate osteogenesis (Nizet et al., 2020). Hence, lower ALP activity of these groups could be related to insufficient Zn release. Concordantly, it was stated that titanium coated with 5 mol% Zn-doped hydroxyapatite precipitated on fibroin nanoparticles increased ALP expression of MC3T3-E1 preosteoblasts, compared to uncoated Ti and TCPS. No significant difference was reported between HA coating and 5% Zn HA coating (Zhong & Ma,

2017). In the present study, incorporation percentage of the osteogenic Zn was closer, although amount used for treatment was much lower than aforementioned studies. However, media renewal provided constant HA presence. Overall, osteogenic differentiation was promoted with treatment of 8B 4Zn HA.

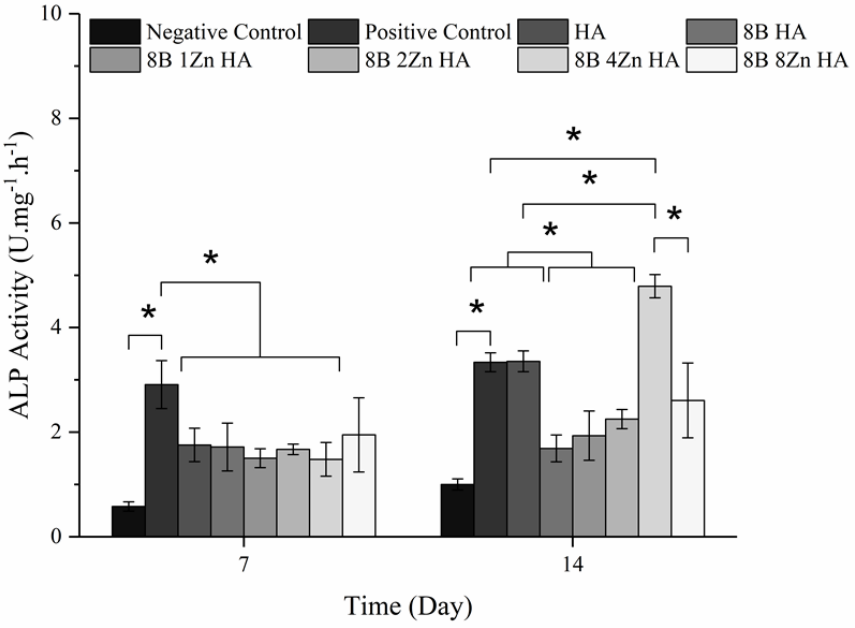

Figure 3.14. ALP activity of hADSCs treated with 0.5 mg/mL HA groups normalized to DNA (n=4, p<0. 05). Asterisk was used to refer statistical significance between groups.

3.2.10 *In Vitro* Angiogenesis

Effect of HA groups on *in vitro* angiogenesis was assessed with tube formation assay (Figure 3.15). Obtained images were evaluated with AngioTool (NIH, USA). It was found that junction density, vessel area and total vessel length of all HA groups were higher than these of negative control and similar to positive control. There was no significant difference between HA groups, indicating major angiogenic activity can be due to ions released from HA. In a previous study subjecting effects of size of HA on HUVECs, it was reported that 20 and 80 nm HA particles were taken up by the

cells, resulting in anti-angiogenic effect, through PI3K/Akt pathway (Shi et al., 2017). However, in the present case, mean particle size of HA groups was between 4-9 μm. Moreover, cells were treated with the extracts.

In a study, effects of HA microstructures with diameter of 12 and 36 μm on angiogenesis was investigated. HA microstructures synthesized via hydrothermal method was reported to significantly increase the expression of endothelial nitric-oxide synthase (eNOS), and vascular endothelial growth factor (VEGF) (Yang et al., 2019). Although B doping did not contribute to significant angiogenesis in this study, 5 mol% B doped HA was reported to increase VEGF-A release and vessel area of HUVECs. It must be noted that the concentration of the used extract was 100 mg/mL, which was much higher than the present study and the extracts were supplemented with vascular endothelial cell growth kit (Pazarceviren et al., 2023). It was also found that area of the vessels formed by HUVECs treated with 0.5 mg/mL of 8B 4Zn HA group was significantly higher than that of positive control. In a previous study, incorporation 10% of 30 mol% Zn-doped HA into gelatin nanofibers was reported to increase eNOS and VEGF significantly, compared to gelatin nanofibers (Chopra et al., 2022). Considering the present literature, it can be said that optimum angiogenic effect of the co-doped HA groups can be modulated with both dopant ratio and concentration of the used HA.

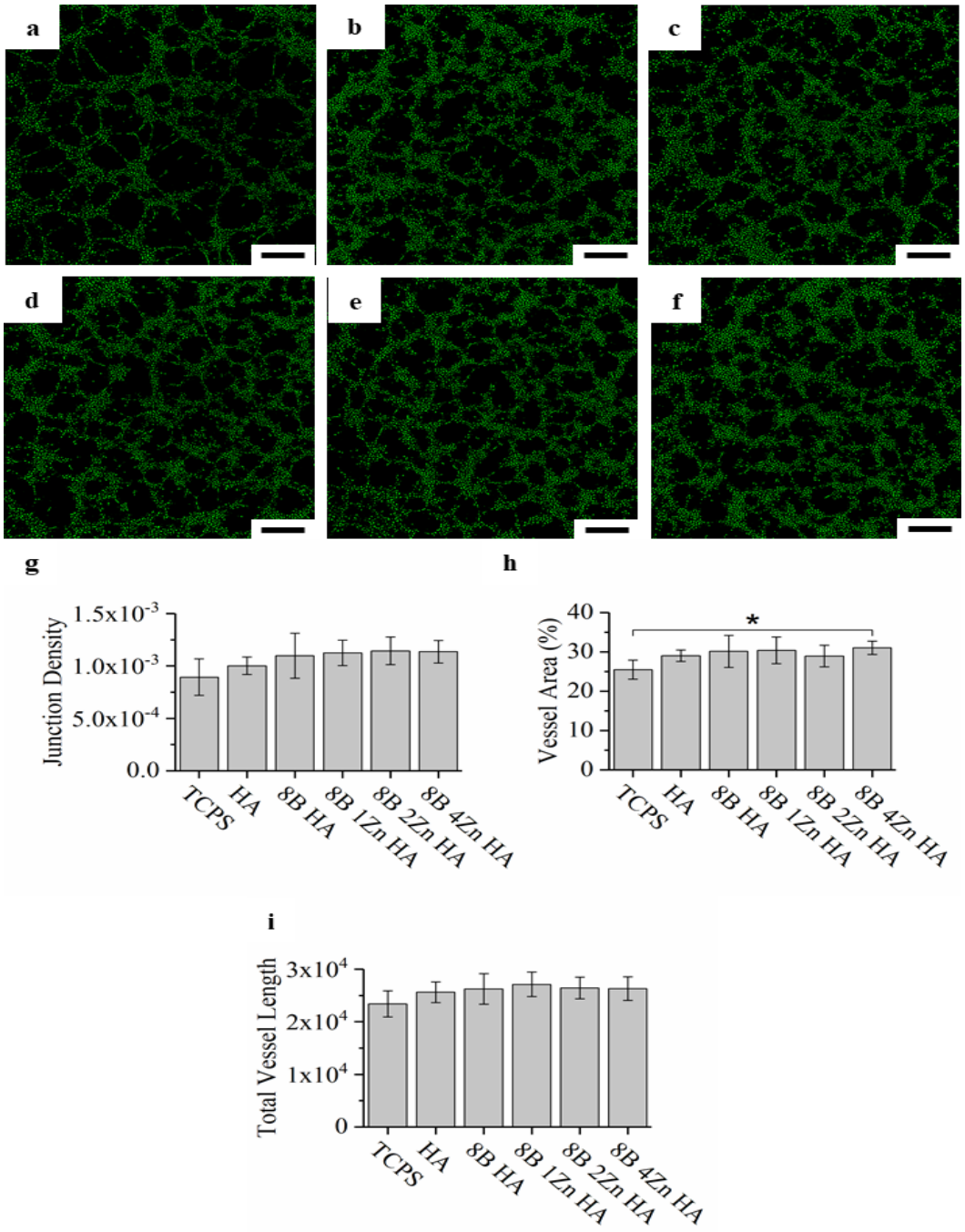

Figure 3.15. Representative 4X Fluorescent microscopy images of TCPS (a), HA (b), 8B HA (c), 8B 1Zn HA (d), 8B 2Zn HA (e) and 8B 4Zn HA (f) groups. Junction density (g), vessel area percentage (h) and total vessel length (i) obtained by image analysis (n=3, p<0. 05). Asterisk refers statistical significance between groups.

3.3 Characterization of F/sA Membranes

F/sA membranes were fabricated with 100:0, 95:5, 90:10 and 80:2 F:sA (w/w) ratios. Obtained membranes were characterized in terms of morphology, equilibrium swelling, weight loss, surface wettability, mechanical properties and release profile. Effect of F/sA compositions on viability and proliferation of hADSCs and immunomodulatory properties against THP-1 derived macrophages were also investigated.

3.3.1 Characterization of sA

FTIR spectra of alginate and sA were analyzed with FTIR spectroscopy, in order to confirm sulfation (Figure 3.16). -OH (3224 cm^{-1}), -COO- (1408 and 1597 cm^{-1}) and COC (1026 cm^{-1}) bands of alginate were observed in both samples (Rhimi et al., 2022). Unlike the alginate spectrum, the sA spectrum was observed to have a band around 1209 cm^{-1} corresponding to S=O symmetric stretching and another peak around 820 cm^{-1} representing S-O-C (Mohammadi et al., 2018; Freeman, Kedem & Cohen, 2008). Degree of sulfation was also determined with Sulfur/Carbon Determinator as 40.87±0.16% (n=3). In a study, it was stated that sA with a sulfation degree of 80% was obtained as a result of a similar reaction, and the degree of sulfation depended on the chlorosulfonic acid concentration in formamide. Also, it was mentioned that overuse of chlorosulfonic acid can result in shortened polymer chain (Syanda et al., 2022).

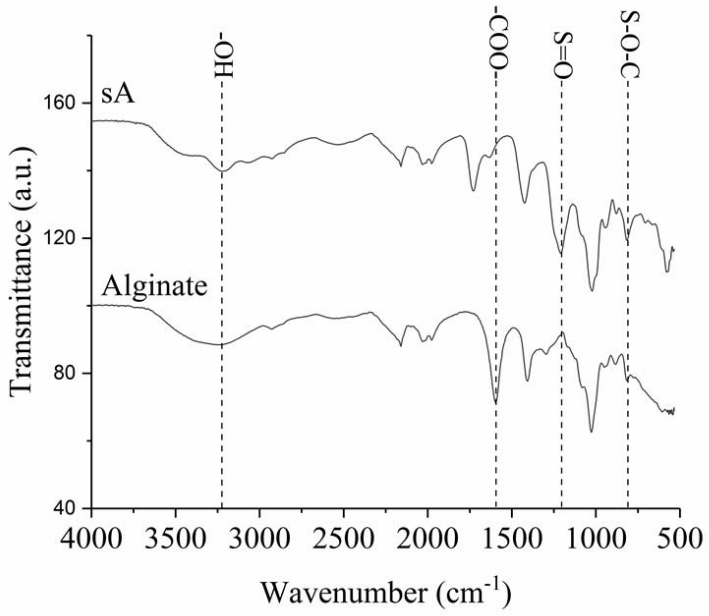

Figure 3.16. FTIR spectra of alginate and sA.

3.3.2 Morphology of F/sA Membranes

Morphology of F/sA scaffolds was investigated with SEM (Figure 3.17**)**. Overall, all scaffolds were observed to have integrity, with minor microcracks. However, it was noticed that surface of the scaffolds became rougher with increasing sA content. It was reported that fabrication method can affect morphology of F membranes. In a similar study, air dried fibroin membrane whose solvent was formic acid, was reported to have smooth morphology (Pasternak et al., 2019). In another study, electropolymerized F membranes were noted to have rougher surface with nanopores (Wang & Zhang, 2014). In addition to fabrication parameters, combination of different materials with F can also play a role on morphology of membranes. It was reported that addition of 30% ($^{v}/_{v}$) polyvinyl alcohol to F resulted in microporous structure, whereas same ratio of glycerol yielded rougher surface with no pores (Geão et al., 2019).

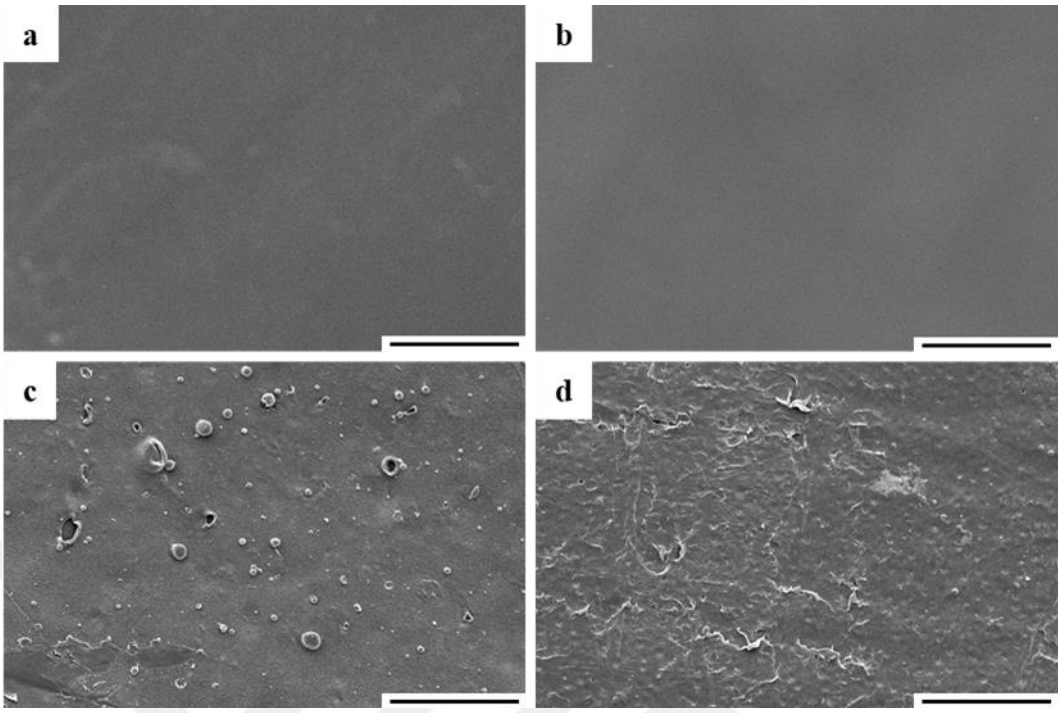

Figure 3.17. 1000X SEM images of a) 100:0 , b) 95:5, c) 90:0 and f) 80:20 F/sA membrane groups (Scale bar: 100 μm).

3.3.3 Equilibrium Swelling Analysis

Equilibrium analysis was performed by the gravimetric method (Figure 3.18). It was observed that all F/sA groups reached to their maximum in 1 hour. It was revealed that water uptake of 5% and 10% sA containing membranes were significantly higher than that of 100% F containing 100:0 group. It was also noticed that starting from 4th hour, water uptake percentage of 80:20 group was significantly lower than that of 100:0 group.

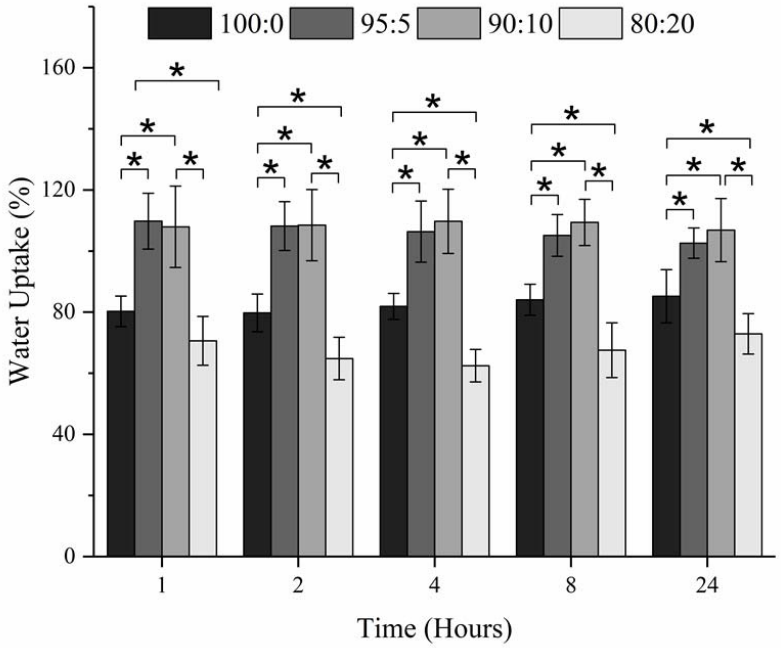

Figure 3.18. 24-hour equilibrium swelling profiles of the F/sA membrane groups (n=3, $p<0.05$). Asterisk refers significant difference between the groups.

3.3.4 Weight Loss Analysis

F/sA membranes were subjected to weight loss analysis in order to investigate *in vitro* stability of the samples (Figure 3.19a). It was found that sA percentage led to increasing weight loss trend with 80:20 group having significantly the highest weight loss at all time points. It was also noticed that weight loss occurred mainly on Day 1. This was expected since sA is a water-soluble polymer and was not crosslinked (Daemi, Mashayekhi & Modaress, 2018). In water uptake analysis, it was observed that even though addition of 5% and 10% sA led to significant increase, 20% resulted in significant decrease, compared to F membrane. Considering the water uptake and weight loss analyses together, it was concluded that lower water uptake of 20% sA containing group was due to early weight loss. Weight loss analysis was also verified with SEM imaging (Figure 3.19b-e**)**. It was observed that 100:0, 95:5 and 90:8

groups held their integrity, whereas visible deformations were present on 80:20 group.

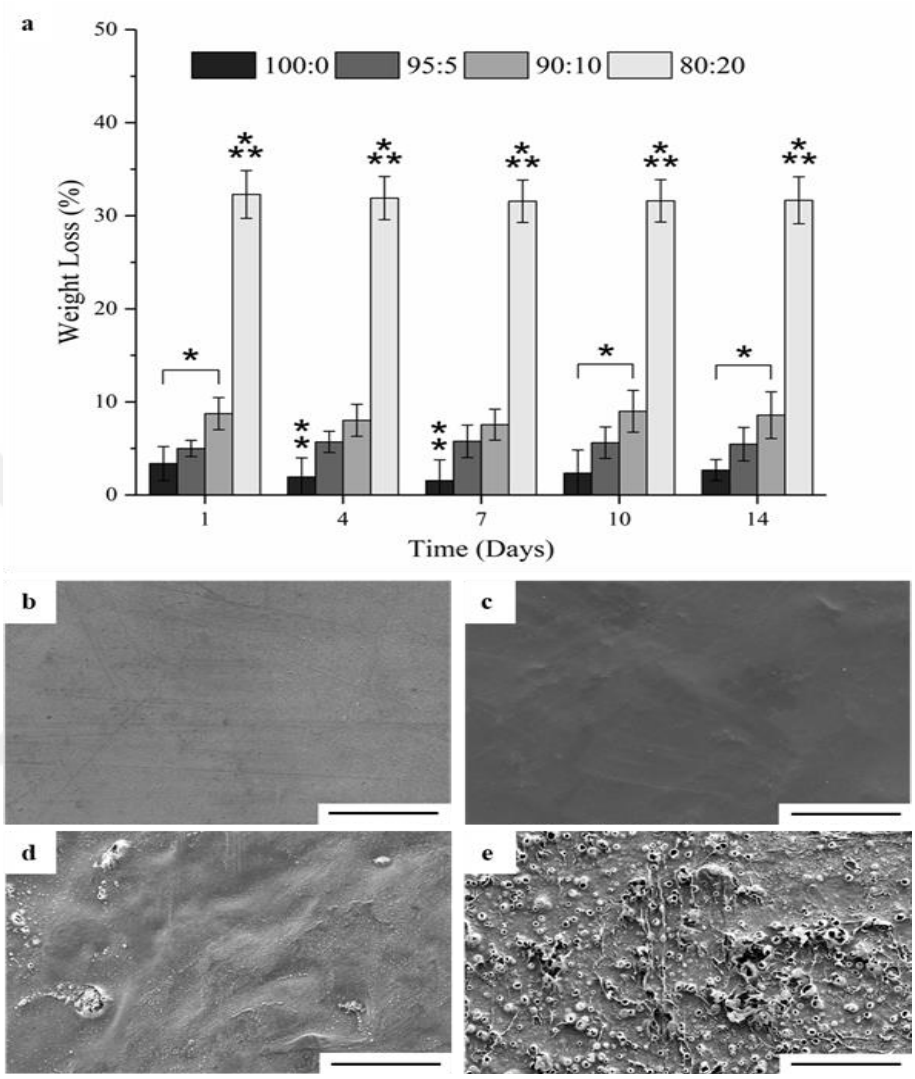

Figure 3.19. a) 14-day weight loss profiles of membrane groups (n=3, $p<0.05$). 1000X SEM images of b) 100:0, c) 95:5, d) 90:10 and e) 80:20 groups after 14 days of incubation in PBS at 37°C (Scale bar: 100µm). Single asterisk denotes statistical significance between the groups. Double and triple asterisk are used show significantly the highest and the lowest groups at the given time point, respectively.

3.3.5 Water Contact Angle Measurement

Surface wettability of the F/sA scaffolds was determined by water contact angle measurements (Figure 3.20). It was found that increasing sA content led to decreasing water contact angle trend with 80:20 group having significantly the lowest water contact angle. It is known that a scaffold's composition and morphology effect its surface wettability. In a study, lyophilized fibroin sponge coated with electrospun fibroin fibers was found to have water contact angle around 42° (Yu et al., 2023). Another study reported that fibroin membrane had water contact angle around 90° (Lan et al., 2022). It was also stated that coating of polyether sulfonate fibers with sA lowers water contact angle form around 75° to 38° (Salimi et al., 2018). It was also known that alginate is highly hydrophilic (Chen et al., 2006; Aburabie et al., 2020). Although there were no reports on hydrophilicity of the F/sA blends, decrease of the water contact angle was attributed to the increasing content of sA, by taking previous literature into account. Water contact angle was stated to effect adhesion of cells, by altering conformation of fibronectin. It was mentioned that surfaces with water contact angle between 40-70° are able to promote cell adhesion (Al-Azzam & Alazzam, 2022). Considering the present data, 95:5 and 90:10 groups were expected to promote cell viability and adhesion. However, surface wettability of the membranes is expected to change, after initial release of sA from the membrane groups.

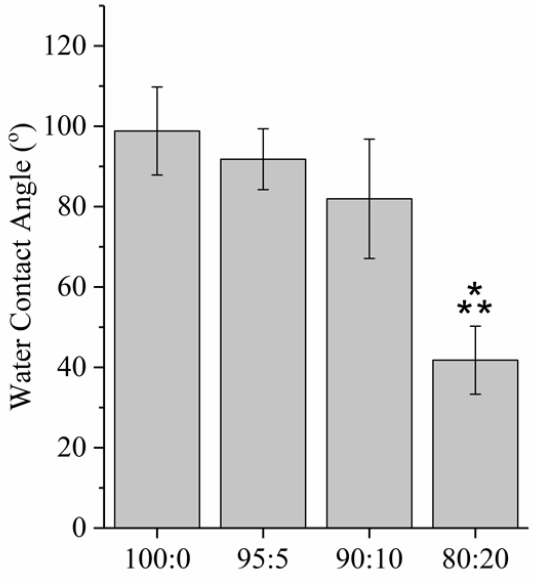

Figure 3.20. Water contact angles of membrane groups (n=3, p<0. 05). Triple asterisk denotes significantly the lowest group.

3.3.6 Tensile Test

In order to determine the mechanical properties of the F/sA membranes, tensile test was performed (Figure 3.21). It was determined that Young's modulus and tensile strength decreased due to increasing sA concentration, while the elongation percentage increased significantly. In a study examining the properties of membranes containing various amounts of F and alginate, it was found that alginate content up to 50% increase the percentage of elongation due to the increase in intramolecular hydrogen bonds (Wang, et al., 2019). In another study examining the effect of increasing F percentage on the mechanical properties of alginate membranes, it was stated that up to 60% F increased the mechanical tensile strength (de Moraes and Beppu, 2013).

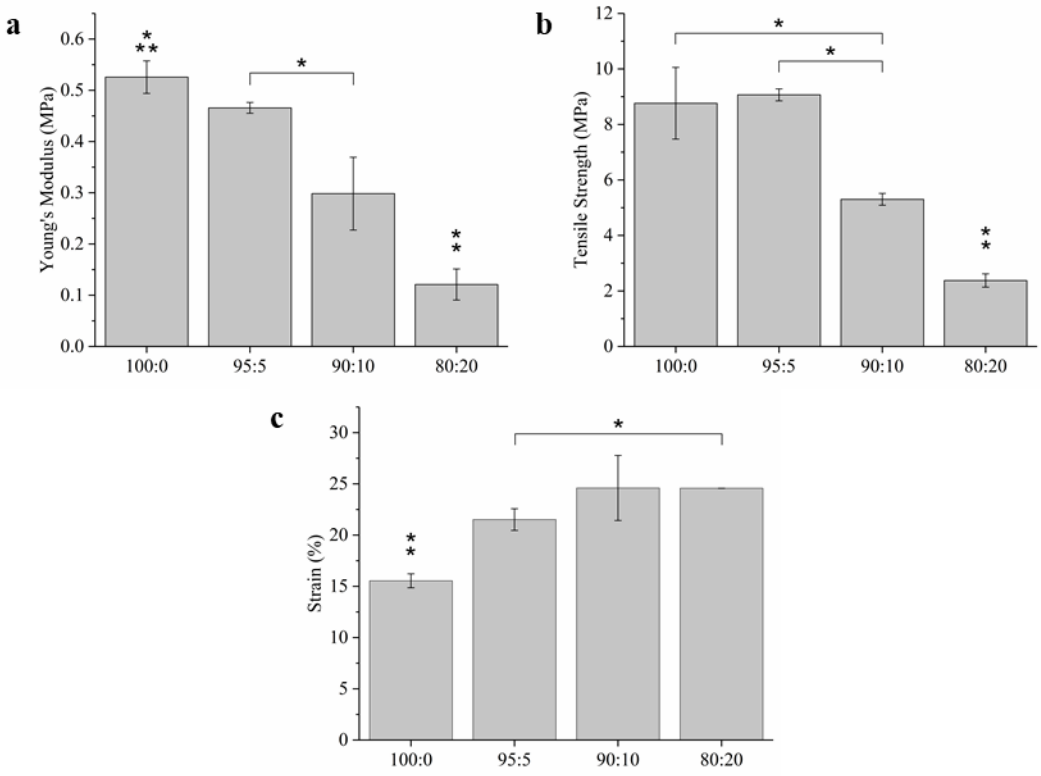

Figure 3.21. Young's modulus (a), tensile strength (b) and strain percentage (c) of membrane groups (n=4, p<0. 05). Single asterisk refers statistical significance between the groups. Double and triple asterisk denote significantly the highest and the lowest groups at the given time point, respectively.

3.3.7 Release of F and sA

Release of F and sA during *in vitro* biodegradation was monitored with BCA and DMMB assay, respectively (Figure 3.22). In concordance with the weight loss, highest release of F and sA was observed from 80:20 group. sA release was found to be increasing with increasing sA ratio of the groups. It was also noted release of sA also triggered release of F as well. SEM analysis after weight loss analysis also revealed visible degradation in 80:20 group (Figure 3.19e). It was mentioned in a study that increased surface area of F scaffolds resulted in higher rate of degradation, due to available chains for hydrolysis (Luo et al., 2015). sA was mentioned to reduce

inflammation through decreasing expression of TNF-α in macrophages (Kerschenmeyer et al., 2024). Periosteum's healing process starts with inflammation taking up to 48h (Lin et al., 2014). Hence, the membrane groups were not crosslinked to allow sA to be released during the acute inflammation phase.

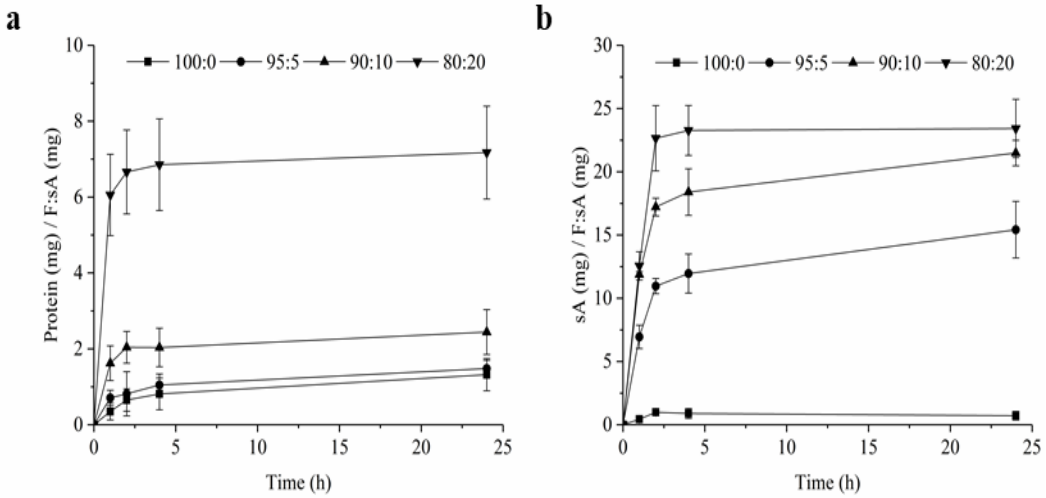

Figure 3.22. a) Protein and b) sA release percentages from F/sA membrane groups (n=3).

3.3.8 Cell Viability and Proliferation

In vitro biocompatibility of F/sA membranes was investigated, in order to determine the effect of sA concentration on cell viability and proliferation (Figure 3.23). On day 1, it was found that all groups had significantly higher cell viability than control group (TCPS). Starting from day 4, it was revealed that 100:0 and 95:5 groups had significantly higher reduction of alamarBlue™, than that of other groups. On days 10 and 14, viability of cells seeded on 80:20 group was significantly the lowest. According to the cell viability and proliferation assay, 5% and 10% sA content was considered as eligible for further studies. Final decision on F/sA membranes was made according to their immunomodulatory properties.

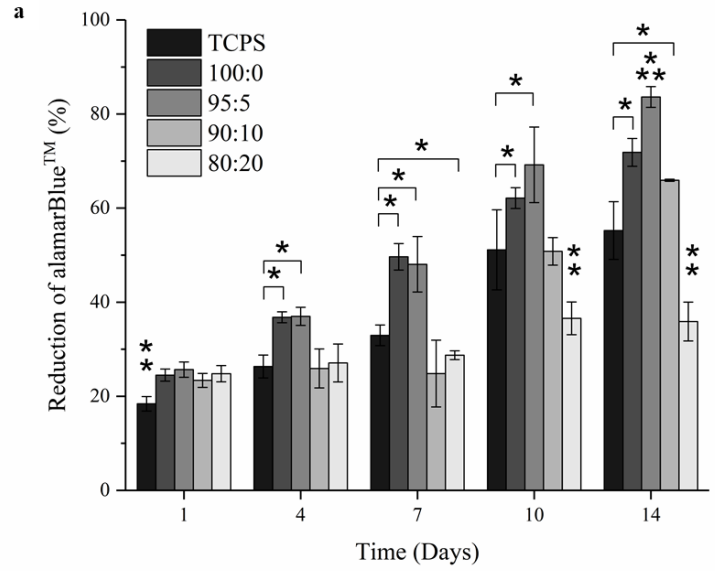

Figure 3.23. Percent reduction of alamarBlue™ by hADSCs seeded on F/sA membranes. Cells seeded on TCPS was used as a control group (n=4, p<0. 05). Single asterisk refers statistical significance between the groups. Double and triple asterisk are used denote significantly the lowest and the highest groups at the given time point, respectively.

3.3.9 Immunomodulatory Properties

Immunomodulatory properties of the F/sA ratio of the membranes were assessed by using THP-1 monocytes. First, monocytes were differentiated into macrophages with PMA (Daigneault et al., 2010). Differentiated cells were then treated with LPS to stimulate proinflammatory cytokines (Chanput et al., 2010). Therefore, levels of Il-1β were measured to examine immunomodulatory effect (Figure 3.24). It was found that cells seeded on TCPS and stimulated with LPS presented significantly higher Il-1β than thoseof cells seeded on TCPS and differentiated with PMA only. Il-1β released from cells seeded on all membrane groups and stimulated with LPS were significantly lower than that of LPS group, for all groups. Notably, Il-1β levels of PMA differentiated cells were similar to those of F/sA 95:5, 90:10 and 80:20 groups.

For the other study, cells were treated with ATP, to induce formation of NLRP3 inflammasomes (Sutterwala, Haasken, & Cassel, 2014).

NLRP3 inflammasomes play role in both inflammatory signaling and innate immune, which can cause rejection of the implant. (Blevins et al., 2022). By lowering the Caspase-1 levels, formation of immune infiltration can be lowered and acute graft rejection can be prevented (Wu et al., 2023). Hence, the concentration of Caspase-1 was investigated to examine immunomodulatory properties of the membrane groups (Figure 3.24) ELISA revealed that ATP treatment significantly increased Caspase-1 levels in all groups. Similar to Il-1β, Caspase-1 levels were significantly lower for all membrane groups, compared to ATP group consisting of cells seeded on TCPS. Again, sA ratio more than 5% did not lead to any significant decrease. It was previously reported that electrospun F fibers did not contribute to immunomodulation of Raw 264.7 macrophages (Akbaba et al., 2021). However, it was also mentioned that immunomodulatory properties of F depend on structure and processing of the scaffold (Motta et al., 2009). Moreover, sA was mentioned to perform as an immunomodulatory biomaterial. It was reported that sA hydrogels decreased expression of TNF-α of mouse bone marrow derived macrophages primed with LPS and IFN-γ (Huang et al., 2023). Considering that sA content more than 5% led to significantly lower cell viability and did not significantly decrease Il-1β and Caspase-1 levels, it was concluded that F/sA 95:5 group would be used for further studies.

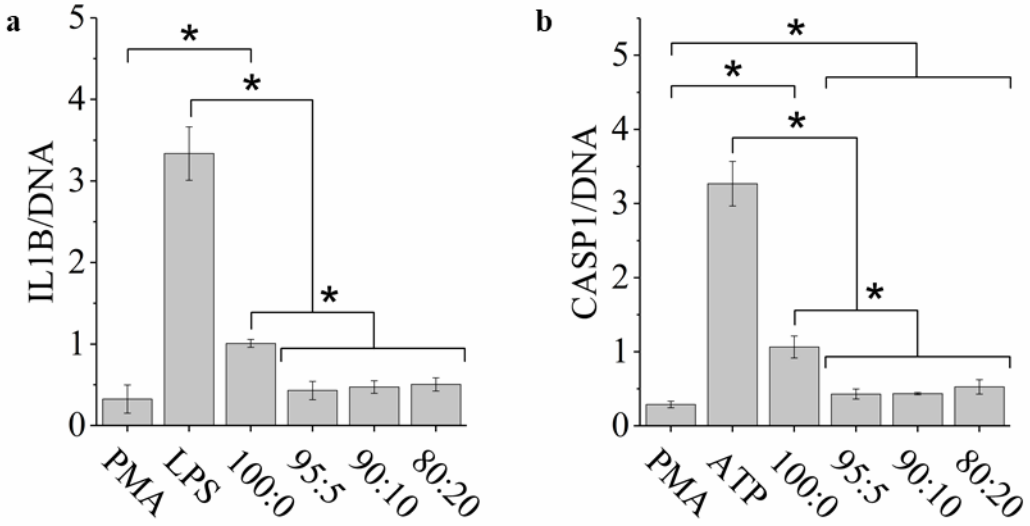

Figure 3.24. a) Extracellular IL1B from PMA differentiated and LPS induced THP-1 cells seeded on F/sA membranes. PMA differentiated cells seeded on TCPS was used as negative control whereas PMA differentiated and LPS induced cells seeded TCPS was used as positive control (n=4, $p<0.05$). b) Intracellular CASP1 from PMA differentiated and ATP induced THP-1 cells seeded on F/sA membranes. PMA differentiated cells seeded on TCPS was used as negative control whereas PMA differentiated and ATP induced cells seeded TCPS was used as positive control (n=4, $p<0.05$). Single asterisk denotes statistical significance between the groups. Double and triple asterisk are used denote significantly the lowest and the highest groups at the given time point, respectively.

3.4 Characterization of Exosome Groups

3.4.1 TEM Imaging

The morphology of exosomes isolated from the F12 group (exosomes isolated from untreated cells) was examined by TEM (Figure 3.25). Exosomes were observed as round shaped and intact (Hosseini-Beheshti et al., 2016).

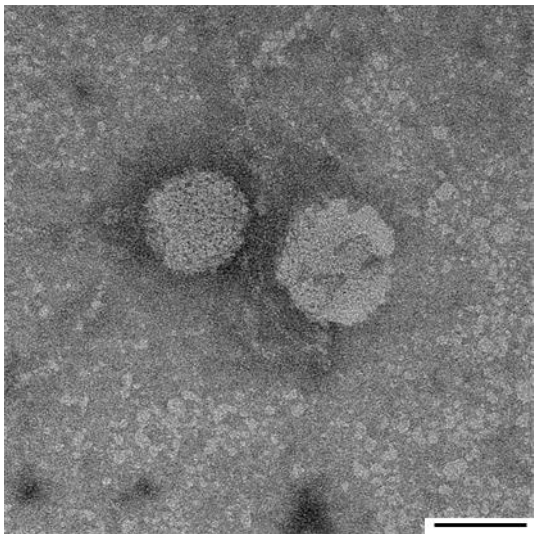

Figure 3.25. TEM image of exosomes from F12 group (Scale bar: 50 nm).

3.4.2 Size and Concentration of Exosome Groups

Particle size of exosomes isolated from different experimental groups was determined by nanoparticle tracking analysis (Figure 3.26a). The average size data for all groups was similar and found to be in the range of 30-200 nm, which is accepted for exosomes (Gurung et al., 2021). Effect of treatment to exosome yield was also investigated (Figure 3.26b). It was determined that the exosome concentration obtained from cells treated with 8B HA was significantly higher than the F12 group that was not subjected to any treatment. No differences were found between other groups. It is stated in the literature that $4x10^7$ stem cells can produce $3–3.5x10^{10}$ particle exosomes within 48 hours (Kordelas et al., 2014). Present data obtained from exosomes isolated from $2x10^7$ cells were found to be similar to the indicated quantity. No significant difference was detected between the average sizes of the exosome groups. This situation is thought to be due to the isolation of exosomes by ultracentrifugation (Yakubovich et al., 2022).

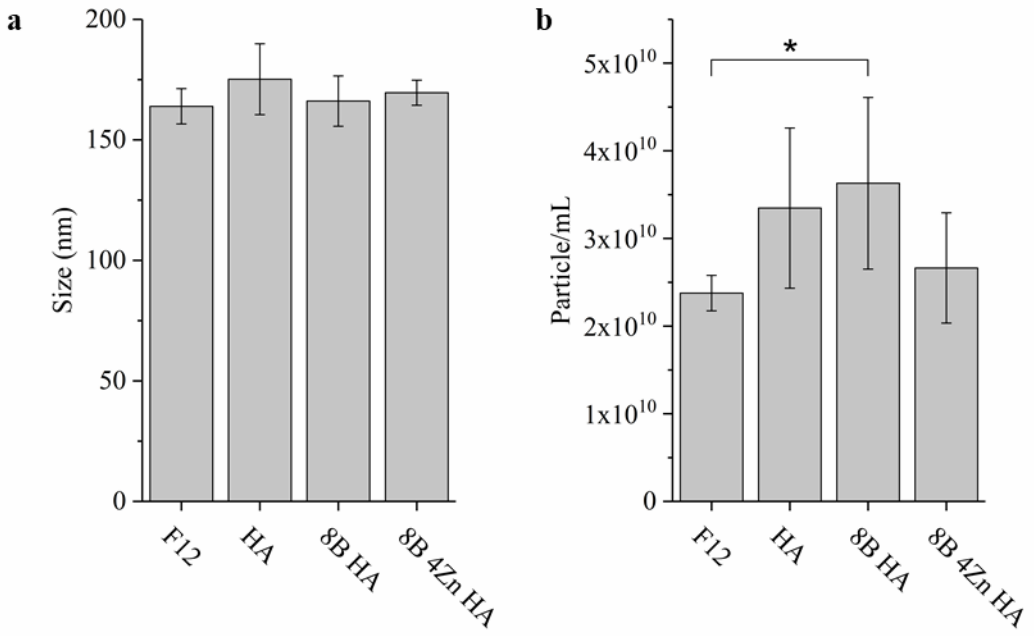

Figure 3.26. Mean particle size (a) and concentration (b) of exosome groups (n=3, $p<0.05$). Asterisk was used to refer statistical significance between groups. Double and triple asterisk were used denote significantly the lowest and the highest groups at the given time point, respectively.

3.4.3 Protein Content

It has been reported in the literature that more than 40,000 proteins were detected in the exosomes of 10 species. It was also stated that these proteins may belong to general processes such as cargo, exosome release, membrane fusion, and may also be associated with carcinoma, sarcoma, melanoma, neurological disorders, cardiovascular diseases, and immune response (Li et al., 2023). Protein content of exosome samples was determined with BCA assay (Figure 3.27). The amount of exosomal protein was normalized to the exosome concentration so that the exosomal content could be evaluated independent from the concentration (Li et al., 2022b). It was determined that the amount of exosomal protein was the lowest e in the 8B HA group. In addition, it was determined that all HA groups caused a significant decrease in the amount of exosomal protein.

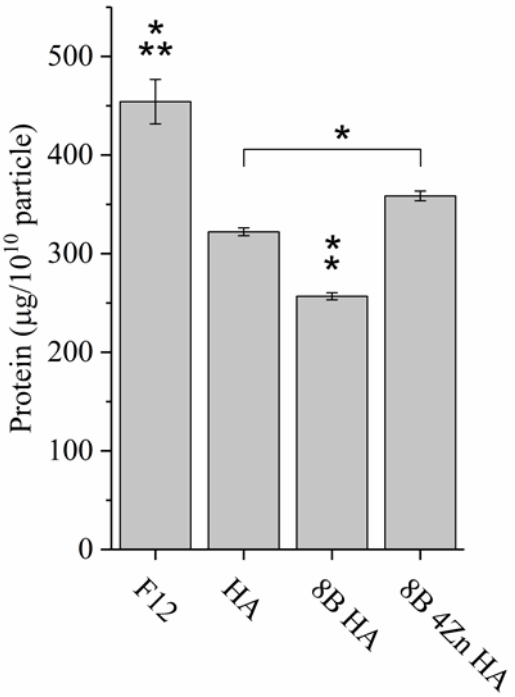

Figure 3.27. Protein contents of exosome groups per 10^{10} particles (n=3, p<0. 05). Asterisk refers statistical significances between the groups.

3.4.4 DNA Content

Exosomal DNA content was measured by PicoGreen dye (Figure 3.28). It was determined that the amount of exosomal DNA caused a significant decrease in all groups HA treated groups. Significantly, the lowest amount of DNA/exosome was detected in the 8B HA group. It has been stated in the literature that exosomal DNA is associated with cell proliferation, programming of immune cells, metastasis, resistance and epigenetic changes that play a role in cancer mechanisms (Bhattacharya et al., 2023). It is thought that the decrease in the amount of exosomal DNA may make the therapeutic use of these exosomes advantageous. It was also reported that exosomal DNA participates in innate immune response (Malkin & Bratman, 2020). Malaria infection is known occur through transmission of exosomal DNA (Sisquella et al., 1985). Hence, exosomal DNA is can also play role in implant rejection.

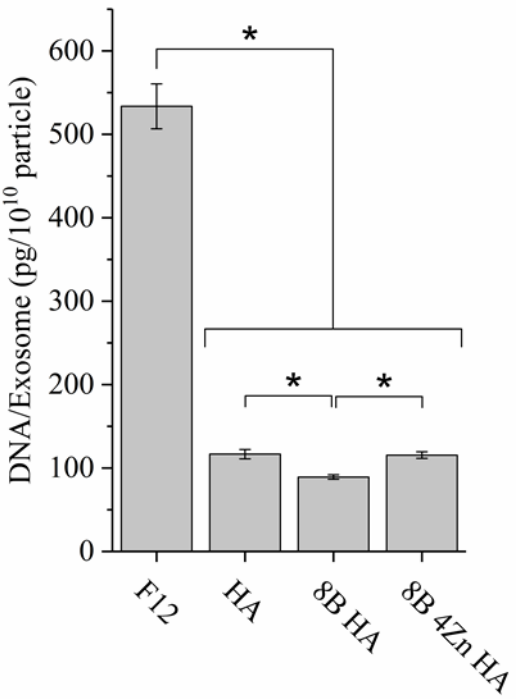

Figure 3.28. DNA contents of exosome groups per 10^{10} particles (n=3, p<0. 05). Asterisk denotes statistical differences between the groups.

3.4.5 RNA Content

In order to examine the effect of the amount of RNA in exosomes on experimental groups, RNA amounts of the isolated samples was determined spectrophotometrically (Figure 3.29). When the effects of HA treatment groups on exosomal RNA released by hADSCs were examined, it was determined that 8B HA and 8B 4ZnHA groups caused a significant increase in the amount of exosomal RNA compared to F12 and HA groups. In a study comparing the RNA contents of exosomes obtained from BMSCs and ADSCs, it was stated that ADSCs contain RNAs belonging to osteogenic genes such as ALP (Baglio et al., 2015). It was previously mentioned that treatment of with HA groups affected viability and osteogenic differentiation of hADSCs. In a study, it was stated that exosomes isolated from pre-differentiated hBMSCs significantly increased osteogenic differentiation of hBMSCs, compared to exosomes isolated from non-differentiated

hBMSCs (Li et al., 2024). Considering the literature and the available data, increased RNA content may be attributed to transcriptomic differences between groups, as a result of treatment.

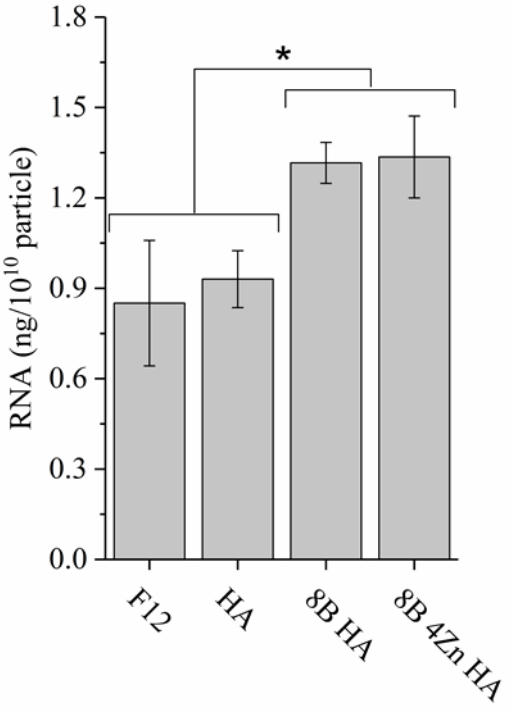

Figure 3.29. RNA contents of exosome groups per 10^{10} particles (n=3, $p<0.05$). Asterisk denotes statistical differences between groups.

3.5 *In Vitro* Properties of Exosome Loaded F/sA Membranes

3.5.1 Cell Viability and Proliferation

The effect of exosomes on the viability and proliferation of hADSCs was determined by alamar blue assay (Figure 3.30). It was determined that the viability of the cells seeded on TCPS was significantly higher on the 1st day and significantly lower on the 4th and 7th days compared to the other groups. No significant difference could be determined between the groups on day 10. On the 14th day, it was noted that the cell viability of the 8B 4Zn group was significantly higher than that of the TCPS and F12

groups. In a study conducted with exosomes obtained from induced pluripotent cells, it was reported that the mentioned exosomes increased the viability of human dermal fibroblasts (Kim et al., 2018). In another study, it was stated that exosomes isolated from hADSCs at a concentration of 2.14×10^{10} particles/ml did not cause a significant change in cell viability on the SKINETHIC™ skin model (Ha et al., 2020). Apart from regeneration, hADSCs can also participate in immunomodulation by cell-to-cell contact and paracrine activity. Stem cells are reported to involve in both innate and adaptive immune responses, with their immunomodulatory effects primarily occurring through interactions with immune cells via direct contact and paracrine signaling. These interactions involve T-cells, B-cells, natural killer cells, macrophages, monocytes, dendritic cells, and neutrophils (Song et al., 2020). Hence, promotion of viability and proliferation of stem cells are considered to be important for regeneration around the implant area.

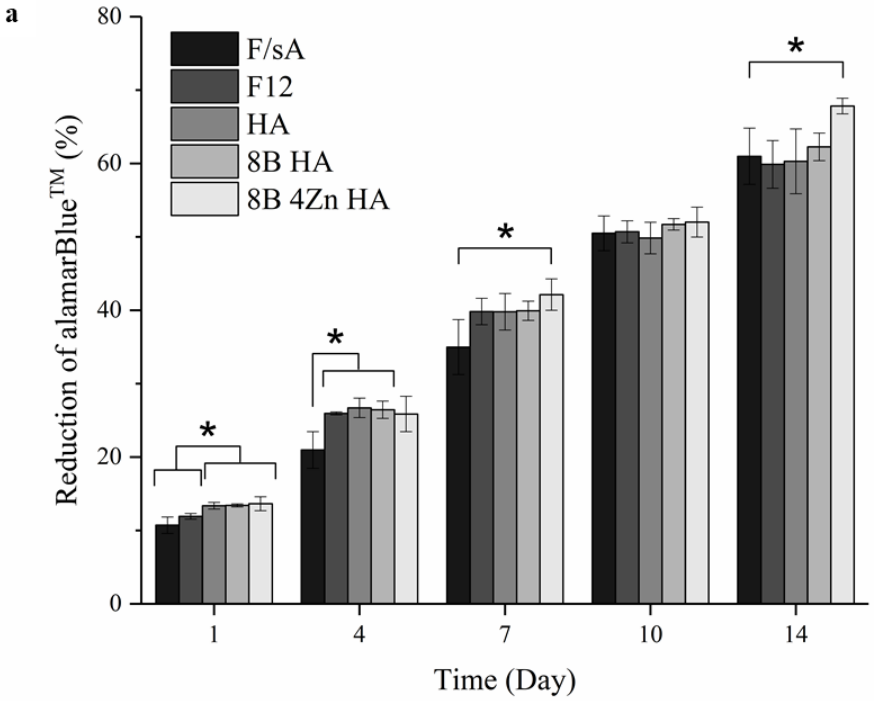

Figure 3.30. Percent reduction of hADSCs seeded on membrane groups (n=4, p<0. 05). Asterisk denotes statistical differences between the groups.

3.5.2 Osteogenic Differentiation

Osteogenic differentiation analysis was performed on hADSCs to determine the effect of experimental groups on osteogenic differentiation. As a result of the studies, it was determined that the osteogenic cell medium caused a significant increase in *COL1A1* and *RUNX2* gene expressions and the amount of osteocalcin (Figure 3.31a, b). Considering *COL1A1* and *RUNX2* gene expressions, it was determined that the 8B HA group had osteogenic activity similar to the TCPS+ group and significantly higher than the F/sA group. Unlike the gene expression analysis results, the amount of osteocalcin was found to be significantly higher in the HA and 8B 4Zn H groups compared to the other groups (Figure 3.31c). *COL1A1* gene expression is regulated by MRTF-A activation as a result of the RHOC/ROCK, TGF-β and WNT/CTNNB pathways (Meng et al., 2018). *RUNX2* expression is regulated by the Jagged/NICD, WNT/CTNNB, BMP/SMAD and TGFB/SMAD pathways, as well as directly by vitamin D (Rutkovskiy et al., 2016). Similarly, OCN is regulated by WNT/CTNNB, RUNX2, in addition to vitamins D and K. Additionally, OCN synthesis occurs later than *COL1A1* and *RUNX2* expression (Li et al., 2016). It is thought that the differences observed in gene expression analysis and ELISA results might be due to the activation of different pathways or the synthesis pathway of osteocalcin, a late osteogenic protein, activated sufficiently after 2 weeks of cultivation.

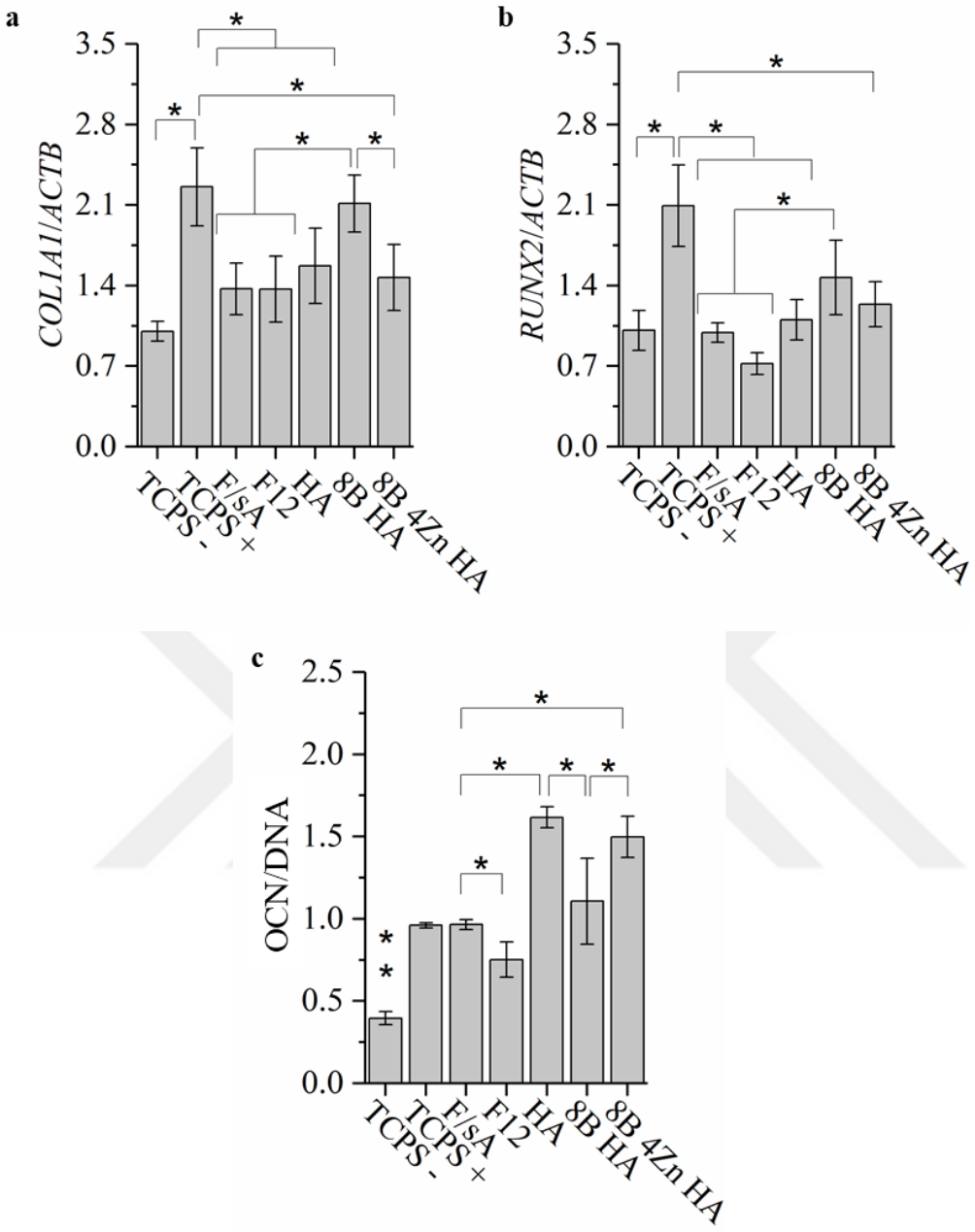

Figure 3.31. Expression of a) *COL1A1* and b) *RUNX2* relative to *ACTB* for cells seeded on groups (n=3, p<0.05). c) Amount of OCN released from hADSCs seeded on membrane groups, relative to DNA (n=4, p<0.05). Single asterisk refers statistically significant difference whereas double asterisk denotes significantly lowest groups. TCPS– stands for cells cultivated on TCPS with cultivation media while TCPS+ refers cells cultivated on TCPS with osteogenic media.

3.5.3 Immunomodulation

3.5.3.1 TLR4 Activation

In order to examine effects of exosome groups on *in vitro* inflammation in samples treated with LPS, the expression of *NFKB* and *IL10* was determined relative to *RPL13* expression (Figure 3.32a, b). Additionally, the amount of extracellular IL1B was determined by ELISA (Figure 3.32c). The results obtained were normalized according to the amount of DNA (Park et al., 2007; Panilaitis et al., 2003). As a result of the analyses, it was determined that LPS treatment significantly increased *NFKB* gene expression and the amount of Il-1β, and significantly decreased *IL10* gene expression. It was determined that F/sA membranes had an immunomodulatory effect by significantly reducing the amount of IL1B and increasing *IL10* gene expression. When exosome contributions were examined, it was determined that F12, HA, 8B 4Zn HA groups caused a significant decrease in *NFKB* gene expression, which is an inflammation marker, and anti-inflammatory *IL10* gene expression, compared to the F/sA group. *NFKB* gene expression can be activated by IL1B and is also regulated by TLRs, TCN and TNFR (Weber et al., 2010; Yu et al., 2020b). For this reason, it is thought that analyzing the expressions of other genes belonging to these pathways is necessary to explain the current situation. *IL10* gene expression was in concordance with IL1B. It was determined that the *IL10* gene expression of the F/sA group was significantly less than the 8B HA and 8B 4Zn HA groups. *IL10* expression in macrophage cells is regulated by activation of ERK protein following TLR2 and TLR4 activation (Saraiva and O'garra, 2010). Similarly, IL1B is regulated by TLR activation following LPS stimulation (Weber et al., 2010).

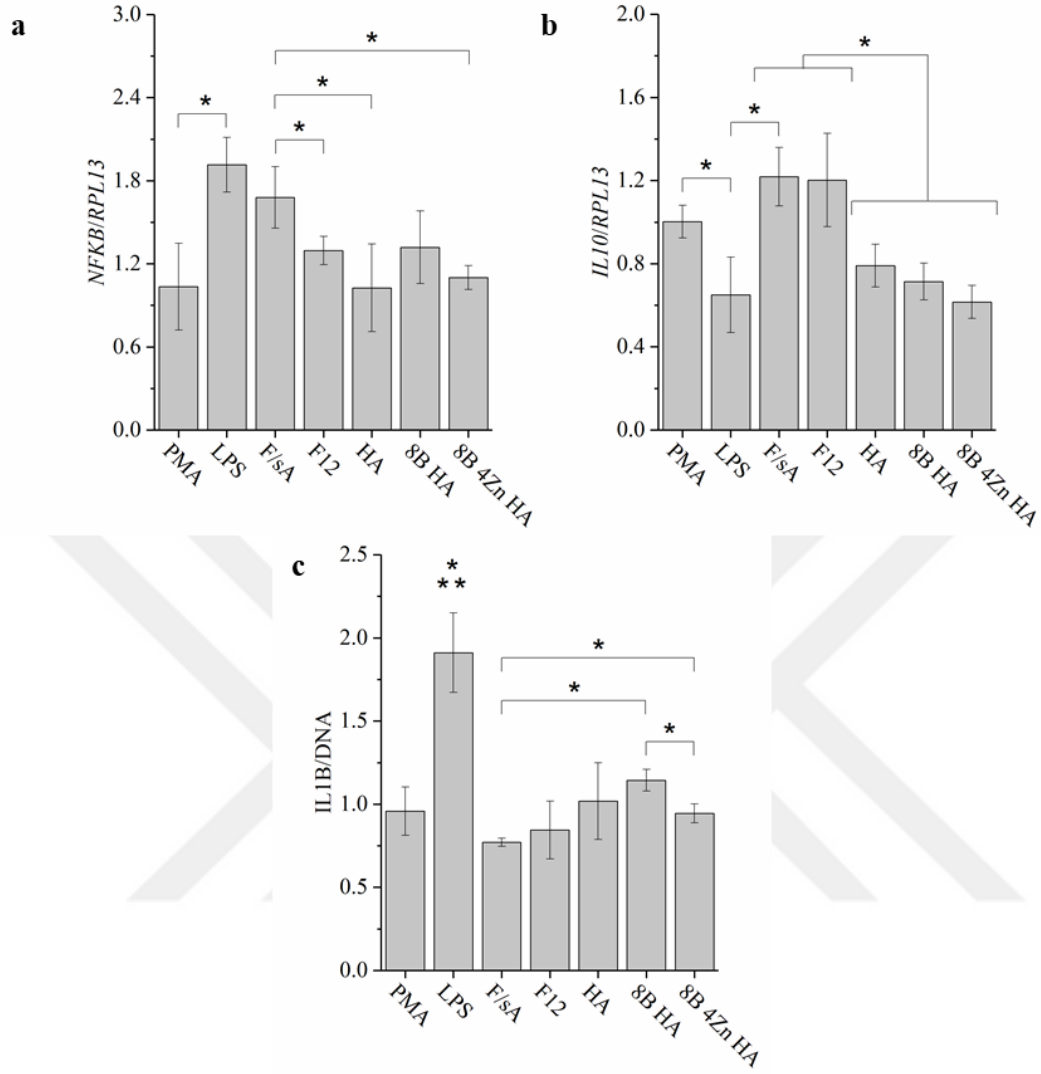

Figure 3.32. Expression of a) *NFKB* and b) *IL10* relative to *RPL13* from PMA differentiated and LPS treated THP-1 macrophages seeded on groups (n=3, $p<0.05$). c) Amount of IL1B released from THP-1 macrophages, relative to DNA (n=4, $p<0.05$). Single asterisk refers statistical significance between the groups whereas triple asterisk denotes significantly the highest group at the given time point.

3.5.4 NLRP3 Inflammasomes

In order to examine inflammasome formation in samples treated with ATP, the expression of *CASP1* and *IL1B* genes was determined in proportion to *RPL13* gene

expression (Figure 33a, b). In order to examine inflammasome formation at the proteome level, the relative amount of CASP1 in the cells was determined with ELISA (Figure 33c). The results obtained were normalized according to the amount of DNA. As a result of stimulation of macrophages with ATP, NLRP3 inflammasomes were formed. As a result, CASP1 levels increase, which in turn increases IL1B levels. For this reason, it was aimed to investigate the expression levels of the mentioned genes (He, Hara, & Núñez, 2016). As a result of the analyses, it was determined that exosome contributions did not have any effect on the *IL1B* expression of ATP-induced macrophages. Consistent with previous analyses, it was determined that the F/sA group caused a significant decrease in *CASP1* expression and protein amount compared to the TCPS+ group. Additionally, considering exosome contributions, F12, HA and 8B HA groups were found to increase *CASP1* expression compared to the F/sA group. Similar results could not be obtained for the amount of CASP1. It was determined that the amount of intracellular CASP1 in the 8B 4Zn HA group was significantly higher than other exosome loaded groups. It has been reported in various studies that zinc plays a role in CASP1 activation (Brough et al., 2009; Truong-Tran et al., 2001). It is thought that the differences at the transcriptome and proteome levels may result from zinc-dependent CASP1 activation.

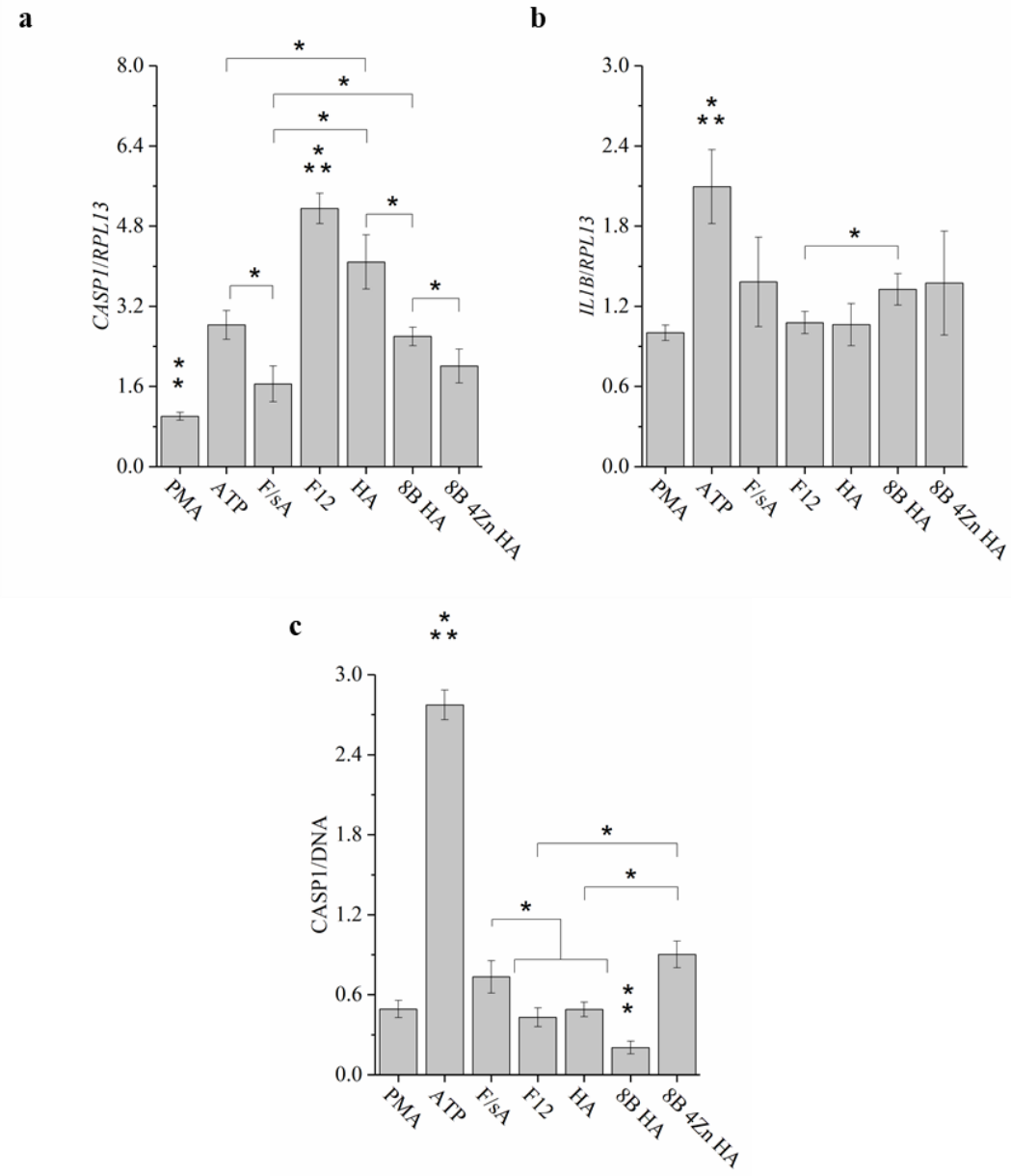

Figure 3.33. a) *CASP1* and b) *IL1B* expression of PMA differentiated and ATP treated THP-1 macrophages seeded on groups relative to *RPL13* (n=3, $p<0.05$). c) Amount of CASP1 released from THP-1 macrophages, relative to DNA (n=4, $p<0.05$). Single asterisk is used to refer statistical significance between the groups. Double and triple asterisk denote significantly the lowest and the highest groups at the given time point, respectively.

3.5.5 Angiogenesis

In order to examine the effect of the groups on angiogenesis on the expression of *NOS3* and *VEGFA* (Figure 34a, b) and the amount of VEGFA was determined (Figure 34c). Although no difference in *VEGFA* expression was detected, it was determined that VEGFA amounts of the F/sA, F12 and 8B 4Zn HA groups were significantly lower than the TCPS group. It was also found that the expression of *NOS3* of the HA group was significantly higher than that of TCPS group. It was mentioned that exosomes may play an angiogenic or anti-angiogenic role. Angiogenic signals in the exosome cargo can be VEGF, MMP or miRNAs, while anti-angiogenic signals can be angiopoietin, angiostatin and collagen (Olejarz et al., 2020). Stem cell exosomes can increase the expression of angiogenic genes with miRNAs, as well as anti-angiogenic signals with VEGF inhibition. Considering the available data, it can be suggested that the HA group has the potential to support angiogenesis.

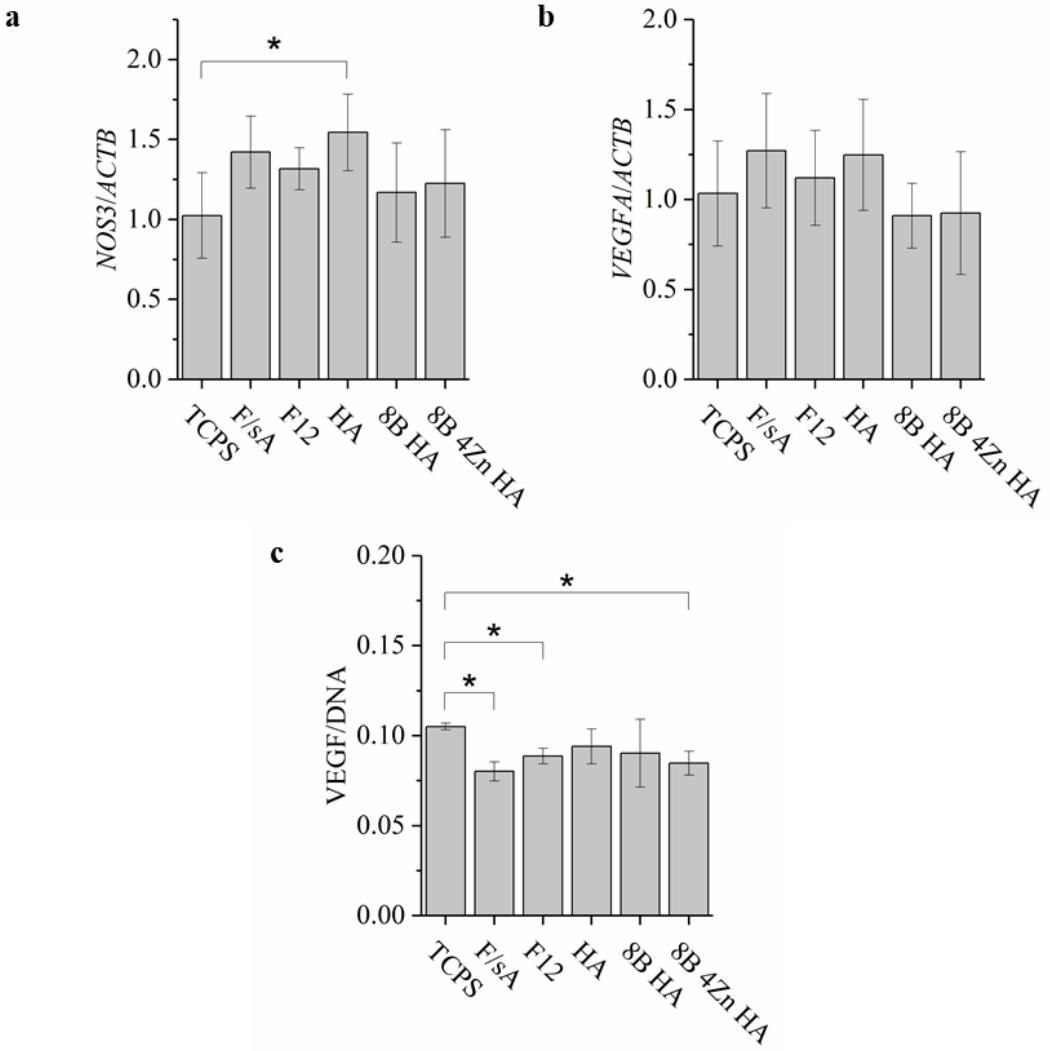

Figure 3.34. Expression of a) *NOS3* and b) *VEGFA* and c) relative amount of VEGFA of HUVECs treated with membrane groups (n=4, $p<0.05$). Single asterisk denotes statistical significance between the groups.

CHAPTER 4

CONCLUSION

In this study, novel F/sA composite scaffolds loaded with exosomes of hADSC treated with pure, and doped HA, were developed for periosteal tissue engineering. Developed a periosteal implant was intended to restore lost periosteum, improve bone regeneration process and shorten healing time. B and Zn-doped HA was investigated for the first time as well. B and Zn release was found to occur mostly within 48 hours, which is a critical timespan for initial cell attachment and angiogenic and immunomodulatory properties for a biomaterial. *In vitro* bioactivity, cell viability and proliferation, osteogenic differentiation and angiogenesis were found to be improved by B and Zn. It was concluded that B and Zn can be utilized to provide complementary effects, needed for bone tissue engineering. Investigation of antimicrobial and immunomodulatory properties of B and Zn co-doped HA can be done to assess further applications of this biomaterial.

In the scope of this thesis, novel F/sA membranes were fabricated and characterized as well. It was revealed that 20% sA led to loss of integrity. F/A ratio of 95:5 was found to be increasing cell viability and proliferation as well as enabling immunomodulation. In this study, M1 macrophages were used to determine immunomodulatory effect of the membrane groups. Further studies can be considered to subject response from T-cells in an *in vivo* model, to demonstrate implant success.

Exosomes were isolated from hADSCs treated with different pure and doped HA groups to evaluate changes in content, for the first time as well. Exosome yield was found to increase with B. HA treatment led to decrease in protein and DNA in general. Interestingly, RNA content was found to significantly higher for B-doped HA and B and Zn doped HA groups, indicating dopants also play role in composition

of exosomes. *In vitro* effects of F/sA membranes loaded with exosomes were investigated for its potential use. It was revealed that exosome loaded F/sA membranes significantly increased initial attachment and proliferation of hADSCs. Osteogenic differentiation was supported by all treated groups. Exosome loaded groups were also found to be immunomodulatory, except 8B 4Zn HA group. Overall, it was shown that exosome loaded F/sA membrane holds potential by its regenerative and immunomodulatory properties. It is considered that further identification of contents of exosomes through transcriptomic and proteomics would explain their effects on recipient cells and identify their potential use in tissue engineering applications.

REFERENCES

Aburabie, J. H., Puspasari, T., & Peinemann, K. V. (2020). Alginate-based membranes: Paving the way for green organic solvent nanofiltration. *Journal of Membrane Science*, *596*, 117615. https://doi.org/10.1016/j.memsci.2019.117615

Akbaba, S., Atila, D., Keskin, D., Tezcaner, T., & Tezcaner, A. (2021). Multilayer fibroin/chitosan oligosaccharide lactate and pullulan immunomodulatory patch for treatment of hernia and prevention of intraperitoneal adhesion. *Carbohydrate Polymers*, *265*, 118066. https://doi.org/10.1016/j.carbpol.2021.118066

Akdere, Ö. E., Shikhaliyeva, İ., & Gümüşderelioğlu, M. (2019). Boron mediated 2D and 3D cultures of adipose derived mesenchymal stem cells. *Cytotechnology*, *71*, 611-622. https://doi.org/10.1007/s10616-019-00310-9

Akshata, C. R., Harichandran, G., & Murugan, E. (2023). Effect of pectin on the crystallization of strontium substituted HA for bone reconstruction application. *Colloids and Surfaces B: Biointerfaces*, *226*, 113312. https://doi.org/10.1016/j.colsurfb.2023.113312

Al Asmari, D., & Khan, M. K. (2019). Evaluate efficacy of desensitizing toothpaste containing zinc-carbonate hydroxyapatite nanocrystals: Non-comparative eight-week clinical study. *Journal of International Society of Preventive and Community Dentistry*, *9*(6), 566–570. https://doi.org/10.4103/jispcd.JISPCD_261_19

Al-Azzam, N., & Alazzam, A. (2022). Micropatterning of cells via adjusting surface wettability using plasma treatment and graphene oxide deposition. *Plos one*, *17*(6), e0269914. https://doi.org/10.1371/journal.pone.0269914

Albayrak, O., Ipekoglu, M., Mahmutyazicioglu, N., Varmis, M., Kaya, E., & Altintas, S. (2016). Preparation and characterization of porous hydroxyapatite pellets: effects of calcination and sintering on the porous structure and mechanical properties. *Proceedings of the Institution of Mechanical Engineers, Part L: Journal of Materials: Design and Applications*, *230*(6), 985-993. https://doi.org/10.1177/1464420715591

Alioui, H., Bouras, O., & Bollinger, J. C. (2019). Toward an efficient antibacterial agent: Zn-and Mg-doped hydroxyapatite nanopowders. *Journal of Environmental Science and Health, Part A*, *54*(4), 315-327. https://doi.org/10.1080/10934529.2018.1550292

Alshemary, A. Z., Pazarceviren, A. E., Tezcaner, A., & Evis, Z. (2016). Mesoporous strontium doped nano sized sulphate hydroxyapatite as a novel biomaterial for bone tissue applications. *RSC Advances*, *6*(72), 68058-68071. https://doi.org/10.1039/C6RA16809D

Anandan, D., & Jaiswal, A. K. (2024). Synthesis methods of hydroxyapatite and biomedical applications: an updated review. *Journal of the Australian Ceramic Society*, *60*(2), 663-679. https://doi.org/10.1007/s41779-023-00943-2

Anandan, D., Kumar, A., & Jaiswal, A. K. (2023). Comparative study of hydroxyapatite synthesized using Schiff base and wet chemical precipitation methods. *Journal of the Mechanical Behavior of Biomedical Materials*, *148*, 106200. https://doi.org/10.1016/j.jmbbm.2023.106200

Arlov, Ø., Aachmann, F. L., Sundan, A., Espevik, T., & Skjåk-Bræk, G. (2014). Heparin-like properties of sulfated alginates with defined sequences and sulfation degrees. *Biomacromolecules*, 15(7), 2744-2750. https://doi.org/10.1021/bm500602w

Arnold, U., Lindenhayn, K., & Perka, C. (2002). In vitro-cultivation of human periosteum derived cells in bioresorbable polymer-TCP-composites. *Biomaterials*, 23(11), 2303-2310. https://doi.org/10.1016/S0142-9612(01)00364-7

Arnsdorf, E. J., Jones, L. M., Carter, D. R., & Jacobs, C. R. (2009). The periosteum as a cellular source for functional tissue engineering. *Tissue Engineering Part A*, 15(9), 2637-2642. https://doi.org/10.1089/ten.TEA.2008.0244

Arslan A., Çakmak S., & Gümüşderelioğlu M. (2018). Enhanced osteogenic activity with boron- doped nanohydroxyapatite-loaded poly(butylene adipate-coterephthalate) fibrous 3D matrix. *Artificial Cells, Nanomedicine, and Biotechnology*, *46*(sup2), 790-799. https://doi.org/10.1080/21691401.2018.1470522

Askari, M., Bonakdar, S., Anbouhi, M. H., Shahsavarani, H., Kargozar, S., Khalaj, V., & Shokrgozar, M. A. (2019). Sustained release of TGF-β1 via genetically-modified cells induces the chondrogenic differentiation of mesenchymal stem cells encapsulated in alginate sulfate hydrogels. *Journal of Materials Science: Materials in Medicine*, *30*(7), 1-11. https://doi.org/10.1007/s10856-018-6203-9

Atila, D., Keskin, D., & Tezcaner, A. (2015). Cellulose acetate based 3-dimensional electrospun scaffolds for skin tissue engineering applications. *Carbohydrate Polymers*, *133*, 251-261. https://doi.org/10.1016/j.carbpol.2015.06.109

Badea, M. A., Balas, M., Popa, M., Borcan, T., Bunea, A.-C., Predoi, D., & Dinischiotu, A. (2023). Biological response of human gingival fibroblasts to

zinc-doped hydroxyapatite designed for dental applications—An in vitro study. *Materials*, *16*(11), 4145. https://doi.org/10.3390/ma16114145

Baei, P., Daemi, H., Mostafaei, F., Sayahpour, F. A., Baharvand, H., & Eslaminejad, M. B. (2021). A tough polysaccharide-based cell-laden double-network hydrogel promotes articular cartilage tissue regeneration in rabbits. *Chemical Engineering Journal*, *418*, 129277. https://doi.org/10.1016/j.cej.2021.129277

Baglio, S. R., Rooijers, K., Koppers-Lalic, D., Verweij, F. J., Pérez Lanzón, M., Zini, N., ... & Pegtel, D. M. (2015). Human bone marrow-and adipose-mesenchymal stem cells secrete exosomes enriched in distinctive miRNA and tRNA species. *Stem Cell Research & Therapy*, *6*(127), 1-20. https://doi.org/10.1186/s13287-015-0116-z

Bahcecioglu, G., Hasirci, N., & Hasirci, V. (2018). Effects of microarchitecture and mechanical properties of 3D microporous PLLA-PLGA scaffolds on fibrochondrocyte and L929 fibroblast behavior. *Biomedical Materials*, *13*(3), 035005. https://doi.org/10.1088/1748-605X/aaa77f

Baldwin, J. G., Wagner, F., Martine, L. C., Holzapfel, B. M., Theodoropoulos, C., Bas, O., ... & Hutmacher, D. W. (2017). Periosteum tissue engineering in an orthotopic in vivo platform. *Biomaterials*, 121, 193-204. https://doi.org/10.1016/j.biomaterials.2016.11.016

Barheine, S., Hayakawa, S., Jäger, C., Shirosaki, Y., & Osaka, A. (2011). Effect of disordered structure of boron- containing calcium phosphates on their in vitro biodegradability. *Journal of the American Ceramic Society*, *94*(8), 2656-2662. https://doi.org/10.1111/j.1551-2916.2011.04400.x

Barkholt, L., Flory, E., Jekerle, V., Lucas-Samuel, S., Ahnert, P., Bisset, L., ... & Salmikangas, P. (2013). Risk of tumorigenicity in mesenchymal stromal cell–based therapies—bridging scientific observations and regulatory viewpoints. *Cytotherapy*, *15*(7), 753-759. https://doi.org/10.1016/j.jcyt.2013.03.005

Becerra, J., Rodriguez, M., Leal, D., Noris-Suarez, K., & Gonzalez, G. (2022). Chitosan-collagen-hydroxyapatite membranes for tissue engineering. *Journal of Materials Science: Materials in Medicine*, *33*(2), 18. https://doi.org/10.1007/s10856-022-06643-w

Begam, H., Kundu, B., Chanda, A., & Nandi, S. K. (2017). MG63 osteoblast cell response on Zn doped hydroxyapatite (HAp) with various surface features. *Ceramics International*, *43*(4), 3752–3760. https://doi.org/10.1016/j.ceramint.2016.12.010

Bermudez-Lekerika, P., Crump, K. B., Wuertz-Kozak, K., Le Maitre, C. L., & Gantenbein, B. (2024). Sulfated hydrogels as primary intervertebral disc cell culture systems. *Gels*, *10*(5), 330. https://doi.org/10.3390/gels10050330

Bhattacharjee, P., Begam, H., Chanda, A., & Nandi, S. K. (2014). Animal trial on zinc doped hydroxyapatite: A case study. *Journal of Asian Ceramic Societies*, *2*(1), 44-51. https://doi.org/10.1016/j.jascer.2014.01.005

Bhattacharya, B., Dhar, R., Mukherjee, S., Gorai, S., Devi, A., Krishnan, A., ... & Papadakis, M. (2023). Exosome DNA: An untold story of cancer. *Clinical and Translational Discovery*, *3*(4), e218. https://doi.org/10.1002/ctd2.218

Blevins, H. M., Xu, Y., Biby, S., & Zhang, S. (2022). The NLRP3 inflammasome pathway: A review of mechanisms and inhibitors for the treatment of inflammatory diseases. *Frontiers in Aging Neuroscience*, *14*, 879021. https://doi.org/10.3389/fnagi.2022.879021

Bojedla, S. S. R., Yeleswarapu, S., Alwala, A. M., Nikzad, M., Masood, S. H., Riza, S., & Pati, F. (2022). Three-dimensional printing of customized scaffolds with polycaprolactone–silk fibroin composites and integration of gingival tissue-derived stem cells for personalized bone therapy. *ACS Applied Bio Materials*, *5*(9), 4465-4479. https://doi.org/10.1021/acsabm.2c00560

Bombaldi de Souza, R. F., & Moraes, Â. M. (2022). Hybrid bilayered chitosan-xanthan/PCL scaffolds as artificial periosteum substitutes for bone tissue regeneration. *Journal of Materials Science*, *57*, 2924–2940. https://doi.org/10.1007/s10853-021-06800-6

Brough, D., Pelegrin, P., & Rothwell, N. J. (2009). Pannexin- 1- dependent caspase- 1 activation and secretion of IL- 1β is regulated by zinc. *European Journal of Immunology*, *39*(2), 352-358. https://doi.org/10.1002/eji.200838843

Butera, A., Gallo, S., Maiorani, C., Preda, C., Chiesa, A., Esposito, F., … & Scribante, A. (2021a). Management of gingival bleeding in periodontal patients with domiciliary use of toothpastes containing hyaluronic acid, lactoferrin, or paraprobiotics: A randomized controlled clinical trial. *Applied Sciences*, *11*(18), 8586. https://doi.org/10.3390/app11188586

Butera, A., Pascadopoli, M., Gallo, S., Lelli, M., Tarterini, F., Giglia, F., & Scribante, A. (2021b). SEM/EDS evaluation of the mineral deposition on a polymeric composite resin of a toothpaste containing biomimetic zn-carbonate hydroxyapatite (microRepair®) in oral environment: A randomized clinical trial. *Polymers*, *13*(16), 2740. https://doi.org/10.3390/polym13162740

Cacciotti, I. (2019). Multisubstituted hydroxyapatite powders and coatings: The influence of the codoping on the hydroxyapatite performances. *International Journal of Applied Ceramic Technology*, *16*(5), 1864-1884. https://doi.org/10.1111/ijac.13229

Candidato Jr, R. T., Sergi, R., Jouin, J., Noguera, O., & Pawłowski, L. (2018). Advanced microstructural study of solution precursor plasma sprayed Zn doped hydroxyapatite coatings. *Journal of the European Ceramic*

Society, *38*(4), 2134-2144. https://doi.org/10.1016/j.jeurceramsoc.2017.12.037

Canillas, M., Pena, P., de Aza, A. H., & Rodríguez, M. A. (2017). Calcium phosphates for biomedical applications. *Boletín de la Sociedad Española de Cerámica Y Vidrio*, *56*(3), 91-112. https://doi.org/10.1016/j.bsecv.2017.05.001

Cao, R., Chen, B., Song, K., Guo, F., Pan, H., & Cao, Y. (2023). Characterization and potential of periosteum-derived cells: an overview. *Frontiers in Medicine*, *10*, 1235992. https://doi.org/10.3389/fmed.2023.1235992

Çayır Bozoğlu, Ü., Kiremitçi, A., Yurtsever, M. Ç., & Gümüşderelioğlu, M. (2022). Peek dental implants coated with boron-doped nano-hydroxyapatites: Investigation of in-vitro osteogenic activity. *Journal of Trace Elements in Medicine and Biology*, *73*, 127026. https://doi.org/10.1016/j.jtemb.2022.127026

Chanput, W., Mes, J., Vreeburg, R. A., Savelkoul, H. F., & Wichers, H. J. (2010). Transcription profiles of LPS-stimulated THP-1 monocytes and macrophages: A tool to study inflammation modulating effects of food-derived compounds. *Food & Function*, *1*(3), 254-261. https://doi.org/10.1039/c0fo00113a

Chen, J., Chen, J., Zhu, Z., Sun, T., Liu, M., Lu, L., ... & Luo, B. (2022). Drug-loaded and anisotropic wood-derived hydrogel periosteum with super antibacterial, anti-inflammatory, and osteogenic activities. *ACS Applied Materials & Interfaces*, *14*(45), 50485-50498. https://doi.org/10.1021/acsami.2c12147

Chen, P. Y., Wang, S. F., Chien, R. R., Tu, C. S., Feng, K. C., Chen, C. S., ... & Schmidt, V. H. (2019). Evolution of the microstructural and mechanical properties of hydroxyapatite bioceramics with varying sintering temperature. *Ceramics International*, *45*(13), 16226-16233. https://doi.org/10.1016/j.ceramint.2019.05.144

Chen, T. W., Chang, S. J., Niu, G. C. C., Hsu, Y. T., & Kuo, S. M. (2006). Alginate-coated chitosan membrane for guided tissue regeneration. *Journal of Applied Polymer Science*, *102*(5), 4528-4534. https://doi.org/10.1002/app.24945

Chen, W., Huang, Y., Han, J., Yu, L., Li, Y., Lu, Z., ... & Xiao, Y. (2016). Immunomodulatory effects of mesenchymal stromal cells-derived exosome. *Immunologic research*, *64*(4), 831-840. https://doi.org/10.1007/s12026-016-8798-6

Chon, J. W., Kim, H., Jeon, H. N., Park, K., Lee, K. G., Yeo, J. H., ... & Park, Y. K. (2012). Silk fibroin hydrolysate inhibits osteoclastogenesis and induces apoptosis of osteoclasts derived from RAW 264.7 cells. *International journal of molecular medicine*, *30*(5), 1203-1210. https://doi.org/10.3892/ijmm.2012.1120

Chung, I. M., Rajakumar, G., Venkidasamy, B., Subramanian, U., & Thiruvengadam, M. (2020). Exosomes: Current use and future applications. *Clinica Chimica Acta*, *500*, 226-232. https://doi.org/10.1016/j.cca.2019.10.022

Çiftci Dede, E., Korkusuz, P., Bilgiç, E., Çetinkaya, M. A., & Korkusuz, F. (2022). Boron nano-hydroxyapatite composite increases the bone regeneration of ovariectomized rabbit femurs. *Biological Trace Element Research*, *200*, 183-196. https://doi.org/10.1007/s12011-021-02626-0

Colnot, C., Zhang, X., & Tate, M. L. K. (2012). Current insights on the regenerative potential of the periosteum: molecular, cellular, and endogenous engineering approaches. *Journal of Orthopaedic Research*, 30(12), 1869-1878. https://doi.org/10.1002/jor.22181

Daemi, H., Mashayekhi, M., & Modaress, M. P. (2018). Facile fabrication of sulfated alginate electrospun nanofibers. *Carbohydrate Polymers*, 198, 481-485. https://doi.org/10.1016/j.carbpol.2018.06.105

Daigneault, M., Preston, J. A., Marriott, H. M., Whyte, M. K., & Dockrell, D. H. (2010). The identification of markers of macrophage differentiation in PMA-stimulated THP-1 cells and monocyte-derived macrophages. *PloS One*, *5*(1), e8668. https://doi.org/10.1371/journal.pone.0008668

Dalgic, A. D., Alshemary, A. Z., Tezcaner, A., Keskin, D., & Evis, Z. (2018). Silicate-doped nano-hydroxyapatite/graphene oxide composite reinforced fibrous scaffolds for bone tissue engineering. *Journal of Biomaterials Applications*, *32*(10), 1392-1405. https://doi.org/10.1177/08853282187636

Dasgupta, S., Bandyopadhyay, A., & Bose, S. (2010). Zn and Mg doped hydroxyapatite nanoparticles for controlled release of protein. *Langmuir*, *26*(7), 4958-4964. https://doi.org/10.1021/la903617e

De Bari, C., Dell'Accio, F., Vanlauwe, J., Eyckmans, J., Khan, I. M., Archer, C. W., ... & Luyten, F. P. (2006). Mesenchymal multipotency of adult human periosteal cells demonstrated single- cell lineage analysis. *Arthritis & Rheumatism*, *54*(4), 1209-1221. https://doi.org/10.1002/art.21753

De Moraes, M. A., & Beppu, M. M. (2013). Biocomposite membranes of sodium alginate and silk fibroin fibers for biomedical applications. *Journal of Applied Polymer Science*, *130*(5), 3451-3457. https://doi.org/10.1002/app.39598

De Souza, R. F. B., de Souza, F. C. B., Thorpe, A., Mantovani, D., Popat, K. C., & Moraes, Â. M. (2020). Phosphorylation of chitosan to improve osteoinduction of chitosan/xanthan-based scaffolds for periosteal tissue engineering. *International Journal of Biological Macromolecules*, *143*, 619-632. https://doi.org/10.1016/j.ijbiomac.2019.12.004

Deng, L., Hou, M., Lv, N., Zhou, Q., Hua, X., Hu, X., ... & He, F. (2024). Melatonin-encapsuled silk fibroin electrospun nanofibers promote vascularized bone regeneration through regulation of osteogenesis-angiogenesis coupling. *Materials Today Bio*, *25*, 100985. https://doi.org/10.1016/j.mtbio.2024.100985

Ding, Q., Zhang, X., Huang, Y., Yan, Y., & Pang, X. (2015). In vitro cytocompatibility and corrosion resistance of zinc-doped hydroxyapatite coatings on a titanium substrate. *Journal of Materials Science*, *50*, 189-202. https://doi.org/10.1007/s10853-014-8578-4

Ding, X., Wu, C., Ha, T., Wang, L., Huang, Y., Kang, H., ... & Fan, Y. (2016). Hydroxyapatite-containing silk fibroin nanofibrous scaffolds for tissue-engineered periosteum. *RSC Advances*, *6*(23), 19463-19474. https://doi.org/10.1039/C5RA26752H

Doherty, L., Wan, M., Kalajzic, I., & Sanjay, A. (2021). Diabetes impairs periosteal progenitor regenerative potential. *Bone*, *143*, 115764. https://doi.org/10.1016/j.bone.2020.115764

El Hotaby, W., Bakr, A. M., Sherif, H. H. A., Soliman, A. A., & Hemdan, B. (2024). Exploring the antimicrobial and anticancer activities of zinc doped nanohydroxyapatite prepared via ultrasonic-assisted method for bone tissue engineering. *Journal of Materials Research*, *39*(13), 1911–1925. https://doi.org/10.1557/s43578-024-01350-4

Fabregat, I., Fernando, J., Mainez, J., & Sancho, P. (2014). TGF-beta signaling in cancer treatment. *Current Pharmaceutical Design*, *20*(17), 2934-2947. https://doi.org/10.2174/13816128113199990591

Fan, W., Crawford, R., & Xiao, Y. (2010). Enhancing in vivo vascularized bone formation by cobalt chloride-treated bone marrow stromal cells in a tissue engineered periosteum model. *Biomaterials*, 31(13), 3580-3589. https://doi.org/10.1016/j.biomaterials.2010.01.083

Farazin, A., & Ghasemi, A. H. (2022). Design, synthesis, and fabrication of chitosan/hydroxyapatite composite scaffold for use as bone replacement tissue by sol–gel method. *Journal of Inorganic and Organometallic Polymers and Materials*, *32*(8), 3067-3082. https://doi.org/10.1007/s10904-022-02343-8

Farias, K. A. S., Sousa, W. J. B., Cardoso, M. J. B., Lima, R. J. S., Rodriguez, M. A., & Fook, M. V. L. (2019). Obtaining hydroxyapatite with different precursors for application as a biomaterial. *Cerâmica*, *65*(373), 99-106. https://doi.org/10.1590/0366-69132019653732462

Fathi, M. H., Hanifi, A., & Mortazavi, V. (2008). Preparation and bioactivity evaluation of bone-like hydroxyapatite nanopowder. *Journal of Materials*

Processing Technology, *202*(1-3), 536-542. https://doi.org/10.1016/j.jmatprotec.2007.10.004

Ferretti, C., Borsari, V., Falconi, M., Gigante, A., Lazzarini, R., Fini, M., ... & Mattioli-Belmonte, M. (2012). Human periosteum-derived stem cells for tissue engineering applications: the role of VEGF. *Stem Cell Reviews and Reports*, *8*, 882-890. https://doi.org/10.1007/s12015-012-9374-7

Ferro, A. C., & Guedes, M. (2019). Mechanochemical synthesis of hydroxyapatite using cuttlefish bone and chicken eggshell as calcium precursors. *Materials Science and Engineering: C*, *97*, 124-140. https://doi.org/10.1016/j.msec.2018.11.083

Fiume, E., Magnaterra, G., Rahdar, A., Verné, E., & Baino, F. (2021). Hydroxyapatite for biomedical applications: A short overview. *Ceramics*, *4*(4), 542-563. https://doi.org/10.3390/ceramics4040039

Freeman, I., Kedem, A., & Cohen, S. (2008). The effect of sulfation of alginate hydrogels on the specific binding and controlled release of heparin-binding proteins. *Biomaterials*, *29*(22), 3260-3268. https://doi.org/10.1016/j.biomaterials.2008.04.025

Frohbergh, M. E., Katsman, A., Botta, G. P., Lazarovici, P., Schauer, C. L., Wegst, U. G., & Lelkes, P. I. (2012). Electrospun hydroxyapatite-containing chitosan nanofibers crosslinked with genipin for bone tissue engineering. *Biomaterials,* *33*(36), 9167-9178. https://doi.org/10.1016/j.biomaterials.2012.09.009

Gao, B. O., Deng, R., Chai, Y. U., Chen, H., Hu, B., Wang, X., ... & Cao, X. (2019). Macrophage-lineage TRAP+ cells recruit periosteum-derived cells for periosteal osteogenesis and regeneration. *The Journal of Clinical Investigation*, *129*(6), 2578-2594. https://doi.org/10.1172/JCI98857

Gao, W., Deng, J., Ren, J., Zhang, W., Wang, Z., He, R., ... & Liang, T. (2022). 3D-printed hydroxyapatite (HA) scaffolds combined with exos from BMSCs cultured in 3D HA scaffolds to repair bone defects. *Composites Part B: Engineering*, *247*, 110315. https://doi.org/10.1016/j.compositesb.2022.110315

Geão, C., Costa-Pinto, A. R., Cunha-Reis, C., Ribeiro, V. P., Vieira, S., Oliveira, J. M., ... & Oliveira, A. L. (2019). Thermal annealed silk fibroin membranes for periodontal guided tissue regeneration. *Journal of Materials Science: Materials in Medicine*, *30*(2), 1-19. https://doi.org/10.1007/s10856-019-6225-y

Gheisari, H., Karamian, E., & Abdellahi, M. (2015). A novel hydroxyapatite–Hardystonite nanocomposite ceramic. *Ceramics International*, *41*(4), 5967-5975. https://doi.org/10.1016/j.ceramint.2015.01.033

Gionet-Gonzales, M. A., Gresham, R. C., Griffin, K. H., Casella, A., Wohlgemuth, R. P., Ramos-Rodriguez, D. H., ... & Leach, J. K. (2023). Mesenchymal stromal cell spheroids in sulfated alginate enhance muscle regeneration. *Acta Biomaterialia*, *155*, 271-281. https://doi.org/10.1016/j.actbio.2022.10.054

Greening, D.W., Xu, R., Ji, H., Tauro, B.J., Simpson, R.J. (2015). A Protocol for Exosome isolation and characterization: Evaluation of ultracentrifugation, density-gradient separation, and immunoaffinity capture methods. In A., Posch (Ed.) *Proteomic Profiling. Methods in Molecular Biology* (Vol 1295, pp. 179-209). https://doi.org/10.1007/978-1-4939-2550-6_15

Grottkau, B. E., & Lin, Y. (2013). Osteogenesis of adipose-derived stem cells. *Bone Research*, *1*(1), 133-145. https://doi.org/10.4248/BR201302003

Guo, H., Li, X., Yuan, X., & Ma, X. (2012). Reconstruction of radial bone defects using the reinforced tissue-engineered periosteum: An experimental study on rabbit weight-bearing segment. *Journal of Trauma and Acute Care Surgery*, *72*(2), E94-E100. https://doi.org/10.1097/TA.0b013e3182196a54

Gupta, S., Qayoom, I., Gupta, P., Gupta, A., Singh, P., Singh, S., & Kumar, A. (2023). Exosome-functionalized, drug-laden bone substitute along with an antioxidant herbal membrane for bone and periosteum regeneration in bone sarcoma. *ACS Applied Materials & Interfaces*, *15*(7), 8824-8839. https://doi.org/10.1021/acsami.2c18308

Gupta, S., Teotia, A. K., Qayoom, I., Shiekh, P. A., Andrabi, S. M., & Kumar, A. (2021). Periosteum-mimicking tissue-engineered composite for treating periosteum damage in critical-sized bone defects. *Biomacromolecules*, *22*(8), 3237-3250. https://doi.org/10.1021/acs.biomac.1c00319

Gurung, S., Perocheau, D., Touramanidou, L., & Baruteau, J. (2021). The exosome journey: From biogenesis to uptake and intracellular signaling. *Cell Communication and Signaling*, *19*(47), 1-19. https://doi.org/10.1186/s12964-021-00730-1

Ha, D. H., Kim, S. D., Lee, J., Kwon, H. H., Park, G. H., Yang, S. H., ... & Yi, Y. W. (2020). Toxicological evaluation of exosomes derived from human adipose tissue-derived mesenchymal stem/stromal cells. *Regulatory Toxicology and Pharmacology*, *115*, 104686. https://doi.org/10.1016/j.yrtph.2020.104686

Han, C., Liu, F., Zhang, Y., Chen, W., Luo, W., Ding, F., ... & Li, Y. (2021). Human umbilical cord mesenchymal stem cell derived exosomes delivered using silk fibroin and sericin composite hydrogel promote wound healing. *Frontiers in Cardiovascular Medicine*, *8*, 713021. https://doi.org/10.3389/fcvm.2021.713021

Hao, S., Zhou, D., Wang, F., Li, G., Deng, A., Ren, X., ... & Su, J. (2024). Hamburger-like biomimetic nutrient periosteum with

osteoimmunomodulation, angio-/osteo-genesis capacity promoted critical-size bone defect repair. *Chemical Engineering Journal*, *489*, 150990. https://doi.org/10.1016/j.cej.2024.150990

Hao, Z., Ren, L., Zhang, Z., Yang, Z., Wu, S., Liu, G., ... & Xia, J. (2023). A multifunctional neuromodulation platform utilizing Schwann cell-derived exosomes orchestrates bone microenvironment via immunomodulation, angiogenesis and osteogenesis. *Bioactive Materials*, *23*, 206-222. https://doi.org/10.1016/j.bioactmat.2022.10.018

Haumont, S. (1961). Distribution of zinc in bone tissue. *Journal of Histochemistry & Cytochemistry*, *9*(2), 141-145. https://doi.org/10.1177/9.2.141

He, J., Li, Z., Yu, T., Wang, W., Tao, M., Wang, S., ... & Ao, Q. (2020). In vitro and in vivo biocompatibility study on acellular sheep periosteum for guided bone regeneration. *Biomedical Materials*, *15*(1), 015013. https://doi.org/10.1088/1748-605X/ab597f

He, X., Liu, Y., Dai, Z., Chen, Y., Liu, W., Dai, H., & Hu, Y. (2024). Yoda1 pretreated BMSC derived exosomes accelerate osteogenesis by activating phospho-ErK signaling via Yoda1-mediated signal transmission. *Journal of Nanobiotechnology*, *22*(1), 407. https://doi.org/10.1186/s12951-024-02669-0

He, Y. X., Zhang, N. N., Li, W. F., Jia, N., Chen, B. Y., Zhou, K., ... & Zhou, C. Z. (2012). N-terminal domain of Bombyx mori fibroin mediates the assembly of silk in response to pH decrease. *Journal of Molecular Biology*, *418*(3-4), 197-207. https://doi.org/10.1016/j.jmb.2012.02.040

He, Y., Hara, H., & Núñez, G. (2016). Mechanism and regulation of NLRP3 inflammasome activation. *Trends in Biochemical Sciences*, *41*(12), 1012-1021. https://doi.org/10.1016/j.tibs.2016.09.002

Hegazy, S. A., & Salama, R. I. (2016). Antiplaque and remineralizing effects of Biorepair mouthwash: A comparative clinical trial. *Pediatric Dental Journal*, *26*(3), 89–94. https://doi.org/10.1016/j.pdj.2016.05.002

Hernández, L., González, J. E., Barranco, V., Veranes-Pantoja, Y., Galván, J. C., & Gattorno, G. R. (2022). Biomimetic hydroxyapatite (HAp) coatings on pure Mg and their physiological corrosion behavior. *Ceramics International*, *48*(1), 1208-1222. https://doi.org/10.1016/j.ceramint.2021.09.206

Ho, W. F., Hsu, H. C., Hsu, S. K., Hung, C. W., & Wu, S. C. (2013). Calcium phosphate bioceramics synthesized from eggshell powders through a solid state reaction. *Ceramics International*, *39*(6), 6467-6473. https://doi.org/10.1016/j.ceramint.2013.01.076

Hoffman, M. D., Xie, C., Zhang, X., & Benoit, D. S. (2013). The effect of mesenchymal stem cells delivered via hydrogel-based tissue engineered

periosteum on bone allograft healing. *Biomaterials*, 34(35), 8887-8898. https://doi.org/10.1016/j.biomaterials.2013.08.005

Hofmann, L., Ludwig, S., Vahl, J. M., Brunner, C., Hoffmann, T. K., & Theodoraki, M. N. (2020). The emerging role of exosomes in diagnosis, prognosis, and therapy in head and neck cancer. *International Journal of Molecular Sciences*, *21*(11), 4072. https://doi.org/10.3390/ijms21114072

Hosseini-Beheshti , E., Choi, W., Weiswald, L. B., Kharmate, G., Ghaffari, M., Roshan-Moniri, M., ... & Guns, E. S. T. (2016). Exosomes confer pro-survival signals to alter the phenotype of prostate cells in their surrounding environment. *Oncotarget*, *7*(12), 14639. https://doi.org/10.18632/oncotarget.7052

Hu, X., Ning, X., Zhao, Q., Zhang, Z., Zhang, C., Xie, M., ... & Ou, C. (2022). Islet-1 mesenchymal stem cells-derived exosome-incorporated angiogenin-1 hydrogel for enhanced acute myocardial infarction therapy. *ACS Applied Materials & Interfaces*, *14*(32), 36289-36303. https://doi.org/10.1021/acsami.2c04686

Huang, C., Dong, L., Zhao, B., Huang, S., Lu, Y., Zhang, X., ... & Luo, G. (2023). Tunable sulfated alginate-based hydrogel platform with enhanced anti-inflammatory and antioxidant capacity for promoting burn wound repair. *Journal of Nanobiotechnology*, *21*, 387. https://doi.org/10.1186/s12951-023-02144-2

Huang, H., Qiang, L., Fan, M., Liu, Y., Yang, A., Chang, D., ... & Weng, J. (2024). 3D-printed tri-element-doped hydroxyapatite/polycaprolactone composite scaffolds with antibacterial potential for osteosarcoma therapy and bone regeneration. *Bioactive Materials*, *31*, 18-37. https://doi.org/10.1016/j.bioactmat.2023.07.004

Huang, Z., & Feng, Y. (2017). Exosomes derived from hypoxic colorectal cancer cells promote angiogenesis through Wnt4-induced β-catenin signaling in endothelial cells. *Oncology Research Featuring Preclinical and Clinical Cancer Therapeutics*, *25*(5), 651-661. https://doi.org/10.3727/096504016X14752792816791

Huiwen, W., Shuai, L., Jia, X., Shihao, D., Kun, W., Runhuai, Y., ... & Jun, L. (2024). 3D-printed nanohydroxyapatite/methylacrylylated silk fibroin scaffold for repairing rat skull defects. *Journal of Biological Engineering*, *18*, 22. https://doi.org/10.1186/s13036-024-00416-5

Iwamoto, T., Hieda, Y., & Kogai, Y. (2022). Physicochemical and microstructural properties of porous Zn-doped hydroxyapatite ceramics: Cell behavior on their surfaces. *Journal of Porous Materials*, *29*(6), 1759–1770. https://doi.org/10.1007/s10934-022-01281-7

Janitermi, M., Jorsarai, S. G. A., & Fattahi, E. (2021). Chondrogenic differentiation of mesenchymal stem cells from rat bone marrow on the elastic modulus of electrospun silk fibroin scaffolds. *Regenerative Engineering and Translational Medicine*, *8*, 125-133. https://doi.org/10.1007/s40883-021-00199-x

Jegoux, F., Goyenvalle, E., Aguado, E., Cognet, R., Moreau, F., & Daculsi, G. (2009). Periostal reconstruction using new porcine microstructured collagen membrane and calcium phosphate cement: a dog model. *Key Engineering Materials*, *396-398*, 257-260. https://doi.org/10.4028/www.scientific.net/KEM.396-398.257

Jiang, Y., Yuan, Z., & Huang, J. (2020). Substituted hydroxyapatite: a recent development. *Materials Technology*, *35*(11-12), 785-796. https://doi.org/10.1080/10667857.2019.1664096

Jodati, H., Evis, Z., Tezcaner, A., Alshemary, A. Z., & Motameni, A. (2023). 3D porous bioceramic based boron-doped hydroxyapatite/baghdadite composite scaffolds for bone tissue engineering. *Journal of the Mechanical Behavior of Biomedical Materials*, *140*, 105722. https://doi.org/10.1016/j.jmbbm.2023.105722

Jodati, H., Tezcaner, A., Alshemary, A. Z., Şahin, V., & Evis, Z. (2022). Effects of the doping concentration of boron on physicochemical, mechanical, and biological properties of hydroxyapatite. *Ceramics International*, *48*(16), 22743-22758. https://doi.org/10.1016/j.ceramint.2022.04.058

Juang, H. Y., & Hon, M. H. (1996). Effect of calcination on sintering of hydroxyapatite. *Biomaterials*, *17*(21), 2059-2064. https://doi.org/10.1177/9.2.141

Jugdaohsingh, R., Pedro, L. D., Watson, A., & Powell, J. J. (2015). Silicon and boron differ in their localization and loading in bone. *Bone Reports*, *1*, 9-15. https://doi.org/10.1016/j.bonr.2014.10.002

Kanou, M., Ueno, T., Kagawa, T., Fujii, T., Sakata, Y., Ishida, N., ... & Sugahara, T. (2005). Osteogenic potential of primed periosteum graft in the rat calvarial model. *Annals of Plastic Surgery*, *54*(1), 71-78. https://doi.org/10.1097/01.sap.0000139562.42726.dd

Kawase, T., Yamanaka, K., Suda, Y., Kaneko, T., Okuda, K., Kogami, H., ... & Yoshie, H. (2010). Collagen- coated poly (l- lactide- co- ε- caprolactone) film: a promising scaffold for cultured periosteal sheets. *Journal of Periodontology*, 81(11), 1653-1662. https://doi.org/10.1902/jop.2010.100194

Kaygili, O., & Tatar, C. (2012). The investigation of some physical properties and microstructure of Zn-doped hydroxyapatite bioceramics prepared by sol–gel

method. *Journal of Sol-Gel Science and Technology*, *61*, 296-309. https://doi.org/10.1007/s10971-011-2627-0

Kelley, M., Fierstein, S., Purkey, L., & DeCicco-Skinner, K. (2022). Endothelial cell tube formation assay: An in vitro model for angiogenesis. *VEGF Signaling: Methods and Protocols* (pp. 187-196). New York, NY: Springer US. https://doi.org/10.1007/978-1-0716-2217-9_12

Kerschenmeyer, A., Arlov, Ø., Malheiro, V., Steinwachs, M., Rottmar, M., Maniura-Weber, K., ... & Zenobi-Wong, M. (2017). Anti-oxidant and immune-modulatory properties of sulfated alginate derivatives on human chondrocytes and macrophages. *Biomaterials Science*, *5*(9), 1756-1765. https://doi.org/10.1039/C7BM00341B

Keskin, M., Kelly, C. P., Moreira-Gonzalez, A., Lobocki, C., Yarim, M., Kaplan, S., & Jackson, I. T. (2008). Repairing critical-sized rat calvarial defects with a periosteal cell-seeded small intestinal submucosal layer. *Plastic and Reconstructive Surgery*, *122*(2), 400-409. https://doi.org/10.1097/PRS.0b013e31817d6206

Kim, K. H., Jeong, L., Park, H. N., Shin, S. Y., Park, W. H., Lee, S. C., ... & Ku, Y. (2005). Biological efficacy of silk fibroin nanofiber membranes for guided bone regeneration. *Journal of Biotechnology*, *120*(3), 327-339. https://doi.org/10.1016/j.jbiotec.2005.06.033

Kim, S., & Park, C. B. (2010). Mussel-inspired transformation of CaCO3 to bone minerals. *Biomaterials*, *31*(25), 6628-6634. https://doi.org/10.1016/j.biomaterials.2010.05.004

Kim, S., Lee, S. K., Kim, H., & Kim, T. M. (2018). Exosomes secreted from induced pluripotent stem cell-derived mesenchymal stem cells accelerate skin cell proliferation. *International Journal of Molecular Sciences*, *19*(10), 3119. https://doi.org/10.3390/ijms19103119

Kolmas, J., Velard, F., Jaguszewska, A., Lemaire, F., Kerdjoudj, H., Gangloff, S. C., & Kaflak, A. (2017). Substitution of strontium and boron into hydroxyapatite crystals: Effect on physicochemical properties and biocompatibility with human Wharton-Jelly stem cells. *Materials Science and Engineering: C*, *79*, 638-646. https://doi.org/10.1016/j.msec.2017.05.066

Kong, X., Zhu, D., Hu, Y., Liu, C., Zhang, Y., Wu, Y., ... & Zhu, L. (2024). Melt electrowriting (MEW)-PCL composite Three-Dimensional exosome hydrogel scaffold for wound healing. *Materials & Design*, *238*, 112717. https://doi.org/10.1016/j.matdes.2024.112717

Koons, G. L., Diba, M., & Mikos, A. G. (2020). Materials design for bone-tissue engineering. *Nature Reviews Materials*, *5*(8), 584-603. https://doi.org/10.1038/s41578-020-0204-2

Korc, M., & Friesel, R. E. (2009). The role of fibroblast growth factors in tumor growth. *Current Cancer Drug Targets*, *9*(5), 639–651. https://doi.org/10.2174/156800909789057006

Kordelas, L., Rebmann, V., Ludwig, A. K., Radtke, S., Ruesing, J., Doeppner, T. R., ... & Giebel, B. (2014). MSC-derived exosomes: A novel tool to treat therapy-refractory graft-versus-host disease. *Leukemia*, *28*(4), 970-973. https://doi.org/10.1038/leu.2014.41

Kouya, T., Tada, S. I., Minbu, H., Nakajima, Y., Horimizu, M., Kawase, T., ... & Tanaka, T. (2013). Microporous membranes of PLLA/PCL blends for periosteal tissue scaffold. *Materials Letters*, *95*, 103-106. https://doi.org/10.1016/j.matlet.2012.12.076

Ladner, Y. D., Alini, M., & Armiento, A. R. (2022). The dimethylmethylene blue assay (DMMB) for the quantification of sulfated glycosaminoglycans. In *Cartilage Tissue Engineering* (pp. 115-121). New York, NY: Springer US. https://doi.org/10.1007/978-1-0716-2839-3_9

Lai, P., Chen, X., Guo, L., Wang, Y., Liu, X., Liu, Y., … Weng, J. (2018). A potent immunomodulatory role of exosomes derived from mesenchymal stromal cells in preventing cGVHD. *Journal of Hematology & Oncology*, *11*(1), 135. https://doi.org/10.1186/s13045-018-0680-7

Lan, D., Liu, Z., Zhou, J., Xu, M., Li, Z., & Dai, F. (2022). Preparation and characterization of silk fibroin/polyethylene oxide nanofiber membranes with antibacterial activity. *Journal of Biomedical Materials Research Part A*, *110*(2), 287-297. https://doi.org/10.1002/jbm.a.37285

Lazar, E., Benedek, T., Korodi, S., Rat, N., Lo, J., & Benedek, I. (2018). Stem cell-derived exosomes - an emerging tool for myocardial regeneration. *World Journal of Stem Cells*, *10*(8), 106–115. https://doi.org/10.4252/wjsc.v10.i8.106

Li, H., Wang, H., Pan, J., Li, J., Zhang, K., Duan, W., ... & Chen, H. (2020). Nanoscaled bionic periosteum orchestrating the osteogenic microenvironment for sequential bone regeneration. *ACS Applied Materials & Interfaces*, *12*(33), 36823-36836. https://dx.doi.org/10.1021/acsami.0c06906

Li, J., He, D., Hu, L., Li, S., Zhang, C., Yin, X., & Zhang, Z. (2023). Decellularized periosteum promotes guided bone regeneration via manipulation of macrophage polarization. *Biotechnology Journal*, *18*(10), 2300094. https://doi.org/10.1002/biot.202300094

Li, N., Song, J., Zhu, G., Li, X., Liu, L., Shi, X., & Wang, Y. (2016). Periosteum tissue engineering—A review. *Biomaterials Science*, *4*(11), 1554-1561. https://doi.org/10.1039/C6BM00481D

Li, S., Deng, R., Zou, X., Rong, Q., Shou, J., Rao, Z., ... & Forouzanfar, T. (2022a). Development and fabrication of co-axially electrospun biomimetic periosteum with a decellularized periosteal ECM shell/PCL core structure to promote the repair of critical-sized bone defects. *Composites Part B: Engineering*, *234*, 109620. https://doi.org/10.1016/j.compositesb.2022.109620

Li, W. J., Chen, H., Tong, M. L., Niu, J. J., Zhu, X. Z., & Lin, L. R. (2022b). Comparison of the yield and purity of plasma exosomes extracted by ultracentrifugation, precipitation, and membrane-based approaches. *Open Chemistry*, *20*(1), 182-191. https://doi.org/10.1515/chem-2022-0139

Li, X. X., Yang, L. X., Wang, C., Li, H., Shi, D. S., & Wang, J. (2023). The roles of exosomal proteins: classification, function, and applications. *International Journal of Molecular Sciences*, *24*(4), 3061. https://doi.org/10.3390/ijms24043061

Li, X., Si, Y., Liang, J., Li, M., Wang, Z., Qin, Y., & Sun, L. (2024). Enhancing bone regeneration and immunomodulation via gelatin methacryloyl hydrogel-encapsulated exosomes from osteogenic pre-differentiated mesenchymal stem cells. *Journal of Colloid and Interface Science*, *672*, 179-199 https://doi.org/10.1016/j.jcis.2024.05.209

Lin, Z., Fateh, A., Salem, D. M., & Intini, G. (2014). Periosteum: biology and applications in craniofacial bone regeneration. *Journal of dental research*, *93*(2), 109-116. https://doi.org/10.1177/0022034513506445

Liu, J., Copland, D. A., Horie, S., Wu, W. K., Chen, M., Xu, Y., ... & Dick, A. D. (2013). Myeloid cells expressing VEGF and arginase-1 following uptake of damaged retinal pigment epithelium suggests potential mechanism that drives the onset of choroidal angiogenesis in mice. *PloS One*, *8*(8), e72935. https://doi.org/10.1371/journal.pone.0072935

Liu, L., Li, C., Liu, X., Jiao, Y., Wang, F., Jiang, G., & Wang, L. (2020). Tricalcium phosphate sol-incorporated poly (ε-caprolactone) membrane with improved mechanical and osteoinductive activity as an artificial periosteum. *ACS Biomaterials Science & Engineering*, *6*(8), 4631-4643. https://dx.doi.org/10.1021/acsbiomaterials.0c00511

Liu, T., Jin, M., Zhang, Y., Weng, W., Wang, T., Yang, H., & Zhou, L. (2021). K+/Sr2+/Na+ triple-doped hydroxyapatites/GelMA composite hydrogel scaffold for the repair of bone defects. *Ceramics International*, *47*(21), 30929-30937. https://doi.org/10.1016/j.ceramint.2021.07.277

Liu, W., Bi, W., Sun, Y., Wang, L., Yu, X., Cheng, R., ... & Cui, W. (2020). Biomimetic organic-inorganic hybrid hydrogel electrospinning periosteum for accelerating bone regeneration. *Materials Science and Engineering: C*, *110*, 110670. https://doi.org/10.1016/j.msec.2020.110670

Lorenz, R. R., Couch, M. E., & Burkey, B. B. (2017). Head and Neck. *Sabiston Textbook of Surgery* (pp. 796-797). Elsevier. ISBN 0323299873.

Lou, Y., Wang, H., Ye, G., Li, Y., Liu, C., Yu, M., & Ying, B. (2021). Periosteal tissue engineering: current developments and perspectives. *Advanced Healthcare Materials*, *10*(12), 2100215. https://doi.org/10.1002/adhm.202100215

Lu, W., Zeng, M., Liu, W., Ma, T., Fan, X., Li, H., ... & Xie, J. (2023). Human urine-derived stem cell exosomes delivered via injectable GelMA templated hydrogel accelerate bone regeneration. *Materials Today Bio*, *19*, 100569. https://doi.org/10.1016/j.mtbio.2023.100569

Luo, Z., Zhang, Q., Shi, M., Zhang, Y., Tao, W., & Li, M. (2015). Effect of pore size on the biodegradation rate of silk fibroin scaffolds. *Advances in Materials Science and Engineering*, *2015*(1), 315397. https://doi.org/10.1155/2015/315397

Maleki-Ghaleh, H., Siadati, M. H., Fallah, A., Zarrabi, A., Afghah, F., Koc, B., ... & Adibkia, K. (2021). Effect of zinc-doped hydroxyapatite/graphene nanocomposite on the physicochemical properties and osteogenesis differentiation of 3D-printed polycaprolactone scaffolds for bone tissue engineering. *Chemical Engineering Journal*, *426*, 131321. https://doi.org/10.1016/j.cej.2021.131321

Malkin, E. Z., & Bratman, S. V. (2020). Bioactive DNA from extracellular vesicles and particles. *Cell Death & Disease*, *11*(7), 584. https://doi.org/10.1038/s41419-020-02803-4

Mayr-Wohlfart, U., Fiedler, J., Günther, K. P., Puhl, W., & Kessler, S. (2001). Proliferation and differentiation rates of a human osteoblast-like cell line (SaOS-2) in contact with different bone substitute materials. *Journal of Biomedical Materials Research*, *57*(1), 132-139. https://doi.org/10.1002/1097-4636(200110)57:1<132::AID-JBM1152>3.0.CO;2-K

Mistry, S., Burman, S., Roy, S., Maitra, N. J., Roy, R., & Chanda, A. (2021). Surface characteristics of titanium dental implants with improved microdesigns: An in vivo study of their osseointegration performance in goat mandible. *Journal of Biomaterials Applications*, *35*(7), 799-813. https://doi.org/10.1177/0885328220947345

Mohammadi, S., Ramakrishna, S., Laurent, S., Shokrgozar, M. A., Semnani, D., Sadeghi, D., ... & Akbari, M. (2019). Fabrication of nanofibrous PVA/alginate- sulfate substrates for growth factor delivery. *Journal of Biomedical Materials Research Part A*, *107*(2), 403-413. https://doi.org/10.1002/jbm.a.36552

Mondal, S., Park, S., Choi, J., Vu, T. T. H., Doan, V. H. M., Vo, T. T., ... & Oh, J. (2023). Hydroxyapatite: A journey from biomaterials to advanced functional materials. *Advances in Colloid and Interface Science*, *321*, 103013. https://doi.org/10.1016/j.cis.2023.103013

Mostafavi, A., Daemi, H., Rajabi, S., & Baharvand, H. (2021). Highly tough and ultrafast self-healable dual physically crosslinked sulfated alginate-based polyurethane elastomers for vascular tissue engineering. *Carbohydrate Polymers*, *257*, 117632. https://doi.org/10.1016/j.carbpol.2021.117632

Motta, A., Maniglio, D., Migliaresi, C., Kim, H. J., Wan, X., Hu, X., & Kaplan, D. L. (2009). Silk fibroin processing and thrombogenic responses. *Journal of Biomaterials Science, Polymer Edition*, *20*(13), 1875-1897. https://doi.org/10.1163/156856208x399936

Mou, X., Shah, J., Bhattacharya, R., Kalejaiye, T. D., Sun, B., Hsu, P. C., & Musah, S. (2022). A biomimetic electrospun membrane supports the differentiation and maturation of kidney epithelium from human stem cells. *Bioengineering*, *9*(5), 188. https://doi.org/10.3390/bioengineering9050188

Mulloy, B., & Rider, C. C. (2006). Cytokines and proteoglycans: An introductory overview. *Biochemical Society Transactions*, *34*(3), 409–413. https://doi.org/10.1042/BST0340409

Murohara, T., Asahara, T., Silver, M., Bauters, C., Masuda, H., Kalka, C., ... & Huang, P. L. (1998). Nitric oxide synthase modulates angiogenesis in response to tissue ischemia. *The Journal of Clinical Investigation*, *101*(11), 2567-2578. https://doi.org/10.1172/JCI1560

Nair, S., & Salomon, C. (2018). Extracellular vesicles and their immunomodulatory functions in pregnancy. *Seminars in Immunopathology*, *40*, 425-437. https://doi.org/10.1007/s00281-018-0680-2

Nizet, A., Cavalier, E., Stenvinkel, P., Haarhaus, M., & Magnusson, P. (2020). Bone alkaline phosphatase: An important biomarker in chronic kidney disease–mineral and bone disorder. *Clinica Chimica Acta*, *501*, 198-206. https://doi.org/10.1016/j.cca.2019.11.012

Norouzzadeh, P., Mabhouti, K., Golzan, M. M., & Naderali, R. (2020). Comparative study on dielectric and structural properties of undoped, Mn-doped, and Ni-doped ZnO nanoparticles by impedance spectroscopy analysis. *Journal of Materials Science: Materials in Electronics*, *31*(10), 7335-7347. https://doi.org/10.1007/s10854-019-02517-0

O'Connor, J. P., Kanjilal, D., Teitelbaum, M., Lin, S. S., & Cottrell, J. A. (2020). Zinc as a therapeutic agent in bone regeneration. *Materials*, *13*(10), 2211. https://doi.org/10.3390/ma13102211

Ofudje, E. A., Adeogun, A. I., Idowu, M. A., & Kareem, S. O. (2019). Synthesis and characterization of Zn-doped hydroxyapatite: Scaffold application, antibacterial and bioactivity studies. *Heliyon*, *5*(5), e01716. https://doi.org/10.1016/j.heliyon.2019.e01716

Okada, M., Oshita, M., Kataoka, M., Azuma, Y., & Furuzono, T. (2021). Shareability of antibacterial and osteoblastic- proliferation activities of zinc- doped hydroxyapatite nanoparticles in vitro. *Journal of Biomedical Materials Research Part B: Applied Biomaterials*, *110*, 799-805. https://doi.org/10.1002/jbm.b.34959

Olejarz, W., Kubiak-Tomaszewska, G., Chrzanowska, A., & Lorenc, T. (2020). Exosomes in angiogenesis and anti-angiogenic therapy in cancers. *International Journal of Molecular Sciences*, *21*(16), 5840. https://doi.org/10.3390/ijms21165840

Omrani, E., Haramshahi, M. A., Najmoddin, N., Saeed, M., & Pezeshki-Modaress, M. (2024). Acceleration of chondrogenic differentiation utilizing biphasic core-shell alginate sulfate electrospun nanofibrous scaffold. *Colloids and Surfaces B: Biointerfaces*, *242*, 114080. https://doi.org/10.1016/j.colsurfb.2024.114080

Ortiz, I. Y., dos Santos, A. R., Costa, A. M., Mavropoulos, E., Tanaka, M. N., da Silva, M. H. P., & de Souza Camargo Jr, S. (2016). In vitro assessment of zinc apatite coatings on titanium surfaces. *Ceramics International*, *42*(14), 15502-15510. https://doi.org/10.1016/j.ceramint.2016.06.203

Panilaitis, B., Altman, G. H., Chen, J., Jin, H. J., Karageorgiou, V., & Kaplan, D. L. (2003). Macrophage responses to silk. *Biomaterials*, *24*(18), 3079–3085. https://doi.org/10.1016/S0142-9612(03)00158-3

Panseri, S., Cunha, C., D'Alessandro, T., Sandri, M., Giavaresi, G., Marcacci, M., ... & Tampieri, A. (2012). Intrinsically superparamagnetic Fe-hydroxyapatite nanoparticles positively influence osteoblast-like cell behaviour. *Journal of Nanobiotechnology*, *10*(1), 1-10. https://doi.org/10.1186/1477-3155-10-32

Park, E. K., Jung, H. S., Yang, H. I., Yoo, M. C., Kim, C., & Kim, K. S. (2007). Optimized THP-1 differentiation is required for the detection of responses to weak stimuli. *Inflammation Research*, *56*(1), 45-50. https://doi.org/10.1007/s00011-007-6115-5

Pasternak, G., Yang, Y., Santos, B. B., Brunello, F., Hanczyc, M. M., & Motta, A. (2019). Regenerated silk fibroin membranes as separators for transparent microbial fuel cells. *Bioelectrochemistry*, *126*, 146-155. https://doi.org/10.1016/j.bioelechem.2018.12.004

Pazarçeviren, A. E., Akbaba, S., Evis, Z., & Tezcaner, A. (2022). Versatile-in-all-trades: Multifunctional boron-doped calcium-deficient hydroxyapatite directs immunomodulation and regeneration. *ACS Biomaterials Science &*

Engineering, *8*(7), 3038-3053. https://doi.org/10.1021/acsbiomaterials.2c00242

Pazarceviren, A. E., Evis, Z., Dikmen, T., Altunbaş, K., Yaprakçı, M. V., Keskin, D., & Tezcaner, A. (2023). Alginate/gelatin/boron-doped hydroxyapatite-coated Ti implants: in vitro and in vivo evaluation of osseointegration. *Bio-Design and Manufacturing*, *6*(3), 217-242. https://doi.org/10.1007/s42242-022-00218-y

Pazarçeviren, A. E., Tezcaner, A., Keskin, D., Kolukısa, S. T., Sürdem, S., & Evis, Z. (2021). Boron-doped biphasic hydroxyapatite/β-tricalcium phosphate for bone tissue engineering. *Biological Trace Element Research*, *199*(3), 968-980. https://doi.org/10.1007/s12011-020-02230-8

Peetsch, A., & Epple, M. (2011). Characterization of the solid components of three desensitizing toothpastes and a mouth wash. *Materialwissenschaft und Werkstofftechnik*, *42*(2), 131-135. https://doi.org/10.1002/mawe.201100744

Ping, P., Guan, S., Ning, C., Yang, T., Zhao, Y., Zhang, P., ... & Fu, S. (2023). Fabrication of blended nanofibrous cardiac patch transplanted with TGF-β3 and human umbilical cord MSCs-derived exosomes for potential cardiac regeneration after acute myocardial infarction. *Nanomedicine: Nanotechnology, Biology and Medicine*, *54*, 102708. https://doi.org/10.1016/j.nano.2023.102708

Poongodi, R., Yang, T. H., Huang, Y. H., Yang, K. D., Chen, H. Z., Chu, T. Y., ... & Cheng, J. K. (2024). Stem cell exosome-loaded Gelfoam improves locomotor dysfunction and neuropathic pain in a rat model of spinal cord injury. *Stem Cell Research & Therapy*, *15*(1), 143. https://doi.org/10.1186/s13287-024-03758-5

Popa, C. L., Deniaud, A., Michaud-Soret, I., Guégan, R., Motelica-Heino, M., & Predoi, D. (2016). Structural and biological assessment of zinc doped hydroxyapatite nanoparticles. *Journal of Nanomaterials*, *2016*(1), 1062878. https://doi.org/10.1155/2016/1062878

Predoi, D., Iconaru, S. L., & Predoi, M. V. (2019). Dextran-coated zinc-doped hydroxyapatite for biomedical applications. *Polymers*, *11*(5), 886. https://doi.org/10.3390/polym11050886

Qi, Y., Wang, H., Wei, K., Yang, Y., Zheng, R. Y., Kim, I. S., & Zhang, K. Q. (2017). A review of structure construction of silk fibroin biomaterials from single structures to multi-level structures. *International Journal of Molecular Sciences*, *18*(3), 237. https://doi.org/10.3390/ijms18030237

Qiu, P., Li, M., Chen, K., Fang, B., Chen, P., Tang, Z., ... & Fan, S. (2020). Periosteal matrix-derived hydrogel promotes bone repair through an early immune regulation coupled with enhanced angio- and

osteogenesis. *Biomaterials*, *227*, 119552. https://doi.org/10.1016/j.biomaterials.2019.119552

Rajput, M., Mondal, P., Yadav, P., & Chatterjee, K. (2022). Light-based 3D bioprinting of bone tissue scaffolds with tunable mechanical properties and architecture from photocurable silk fibroin. *International Journal of Biological Macromolecules*, *202*, 644-656. https://doi.org/10.1016/j.ijbiomac.2022.01.081

Rajzer, I., Menaszek, E., Kwiatkowski, R., Planell, J. A., & Castano, O. (2014). Electrospun gelatin/poly (ε-caprolactone) fibrous scaffold modified with calcium phosphate for bone tissue engineering. *Materials Science and Engineering: C*, 44, 183-190. https://doi.org/10.1016/j.msec.2014.08.017

Ramya, J. R., Arul, K. T., Elayaraja, K., & Kalkura, S. N. (2014). Physicochemical and biological properties of iron and zinc ions co-doped nanocrystalline hydroxyapatite, synthesized by ultrasonication. *Ceramics International*, *40*(10), 16707-16717. https://doi.org/10.1016/j.ceramint.2014.08.035

Ressler, A., Žužić, A., Ivanišević, I., Kamboj, N., & Ivanković, H. (2021). Ionic substituted hydroxyapatite for bone regeneration applications: A review. *Open Ceramics*, *6*, 100122. https://doi.org/10.1016/j.oceram.2021.100122

Rethi, L., Lu, L., Huynh, V. T., Manga, Y. B., Rethi, L., Mutalik, C., ... & Chuang, E. Y. (2021). Bioactive glass fiber-reinforced plastic composites prompt a crystallographic lophelia atoll-like skeletal microarchitecture actuating periosteal cambium. *ACS Applied Materials & Interfaces*, *13*(27), 32226-32241. https://doi.org/10.1021/acsami.1c07950

Rhimi, A., Zlaoui, K., Horchani-Naifer, K., & Ennigrou, D. J. (2022). Characterization and extraction of sodium alginate from Tunisian algae: Synthesizing a cross-linked ultrafiltration membrane. *Iranian Polymer Journal*, *31*(3), 367-382. https://doi.org/10.1007/s13726-021-01005-9

Rial, R., González-Durruthy, M., Liu, Z., & Ruso, J. M. (2021). Advanced materials based on nanosized hydroxyapatite. *Molecules*, *26*(11), 3190. https://doi.org/10.3390/molecules26113190

Rockwood, D. N., Preda, R. C., Yücel, T., Wang, X., Lovett, M. L., & Kaplan, D. L. (2011). Materials fabrication from Bombyx mori silk fibroin. *Nature Protocols*, *6*(10), 1612–1631. https://doi.org/10.1038/nprot.2011.379

Romero, R., Travers, J. K., Asbury, E., Pennybaker, A., Chubb, L., Rose, R., ... & Kipper, M. J. (2017). Combined delivery of FGF- 2, TGF- β1, and adipose-derived stem cells from an engineered periosteum to a critical- sized mouse femur defect. *Journal of Biomedical Materials Research Part A, 105*(3), 900-911. https://doi.org/10.1002/jbm.a.35965

Romero-Torrecilla, J. A., Lamo-Espinosa, J. M., Ripalda-Cemboráin, P., López-Martínez, T., Abizanda, G., Riera-Álvarez, L., ... & Granero-Moltó, F. (2023). An engineered periosteum for efficient delivery of rhBMP-2 and mesenchymal progenitor cells during bone regeneration. *NPJ Regenerative Medicine*, *8*(1), 54. https://doi.org/10.1038/s41536-023-00330-2

Rutkovskiy, A., Stensløkken, K. O., & Vaage, I. J. (2016). Osteoblast differentiation at a glance. *Medical Science Monitor Basic Research*, *22*, 95-106. https://doi.org/10.12659/MSMBR.901142

Sabu, U., Logesh, G., Rashad, M., Joy, A., & Balasubramanian, M. (2019). Microwave assisted synthesis of biomorphic hydroxyapatite. *Ceramics International*, *45*(6), 6718-6722. https://doi.org/10.1016/j.ceramint.2018.12.161

Saddiqi, N., Patra, D., & Seeger, S. (2017). Hydroxyapatite biomineralization on functionalized silicone nanofilaments. *Colloid and Interface Science Communications*, *16*, 1-5. https://doi.org/10.1016/j.colcom.2016.12.002

Sadeghi, A., Zare-Gachi, M., Najjar-Asl, M., Rajabi, S., Fatemi, M. J., Forghani, S. F., ... & Pezeshki-Modaress, M. (2023). Hybrid gelatin-sulfated alginate scaffolds as dermal substitutes can dramatically accelerate healing of full-thickness diabetic wounds. *Carbohydrate Polymers*, *302*, 120404. https://doi.org/10.1016/j.carbpol.2022.120404

Sadetskaya, A. V., Bobrysheva, N. P., Osmolowsky, M. G., Osmolovskaya, O. M., & Voznesenskiy, M. A. (2021). Correlative experimental and theoretical characterization of transition metal doped hydroxyapatite nanoparticles fabricated by hydrothermal method. *Materials Characterization*, *173*, 110911. https://doi.org/10.1016/j.matchar.2021.110911

Salimi, E., Ghaee, A., Ismail, A. F., & Karimi, M. (2018). Anti-thrombogenicity and permeability of polyethersulfone hollow fiber membrane with sulfonated alginate toward blood purification. *International Journal of Biological Macromolecules*, *116*, 364-377. https://doi.org/10.1016/j.ijbiomac.2018.04.137

Sánchez-Campos, D., Reyes Valderrama, M. I., López-Ortíz, S., Salado-Leza, D., Fernández-García, M. E., Mendoza-Anaya, D., ... & Rodríguez-Lugo, V. (2021). Modulated monoclinic hydroxyapatite: the effect of ph in the microwave assisted method. *Minerals*, *11*(3), 314. https://doi.org/10.3390/min11030314

Sangkert, S., Kamolmatyakul, S., Gelinsky, M., & Meesane, J. (2021). 3D printed scaffolds of alginate/polyvinylalcohol with silk fibroin based on mimicked extracellular matrix for bone tissue engineering in maxillofacial surgery. *Materials Today Communications*, *26*, 102140. https://doi.org/10.1016/j.mtcomm.2021.102140

Schönmeyr, B., Clavin, N., Avraham, T., Longo, V., & Mehrara, B. J. (2009). Synthesis of a tissue-engineered periosteum with acellular dermal matrix and cultured mesenchymal stem cells. *Tissue Engineering Part A*, 15(7), 1833-1841. https://doi.org/10.1089/ten.tea.2008.0446

Schwartz, H. S., Holt, G. E., & Halpern, J. L. (2016). Bone tumors. In C. M. Townsend Jr, R. D. Beauchamp, B. M. Evers, & K. L. Mattox. *Sabiston textbook of surgery: The biological basis of modern surgical practice* (20th ed., p. 778). Elsevier. ISBN 978-0-323-40162-3.

Sedykh, S. E., Burkova, E. E., Purvinsh, L. V., Klemeshova, D. A., Ryabchikova, E. I., & Nevinsky, G. A. (2019). Milk exosomes: Isolation, biochemistry, morphology, and perspectives of use. In *Extracellular Vesicles*. IntechOpen. https://doi.org/10.5772/intechopen.85416

Shi, X., Chen, S., Zhao, Y., Lai, C., & Wu, H. (2013). Enhanced osteogenesis by a biomimic pseudo- periosteum- involved tissue engineering strategy. *Advanced Healthcare Materials*, *2*(9), 1229-1235. https://doi.org/10.1002/adhm.201300012

Shi, X., Fujie, T., Saito, A., Takeoka, S., Hou, Y., Shu, Y., ... & Khademhosseini, A. (2014). Periosteum- mimetic structures made from freestanding microgrooved nanosheets. *Advanced Materials*, *26*(20), 3290-3296. https://doi.org/10.1002/adma.201305804

Shi, X., Zhou, K., Huang, F., & Wang, C. (2017). Interaction of hydroxyapatite nanoparticles with endothelial cells: internalization and inhibition of angiogenesis in vitro through the PI3K/Akt pathway. *International Journal of Nanomedicine*, *12*, 5781–5795. https://doi.org/10.2147/IJN.S140179

Shuai, Y., Lu, H., Lv, R., Wang, J., Wan, Q., Mao, C., & Yang, M. (2021). Biomineralization directed by prenucleated calcium and phosphorus nanoclusters improving mechanical properties and osteogenic potential of Antheraea pernyi silk fibroin- based artificial periosteum. *Advanced Healthcare Materials*, *10*(8), 2001695. https://doi.org/10.1002/adhm.202001695

Singer, V. L., Jones, L. J., Yue, S. T., & Haugland, R. P. (1997). Characterization of PicoGreen reagent and development of a fluorescence-based solution assay for double-stranded DNA quantitation. *Analytical Biochemistry*, *249*(2), 228-238. https://doi.org/10.1006/abio.1997.2177

Singh, N., Uppoor, A., & Naik, D. G. (2015). Bone's smart envelope-The periosteum: Unleashing its regenerative potential for periodontal reconstruction. *International Journal of Contemporary Dental and Medical Reviews*, 090215. https://doi.org/10.15713/ins.ijcdmr.62

Sirait, M., Sinulingga, K., Siregar, N., & Doloksaribu, M. E. (2022). Characterization of hydroxyapatite by cytotoxicity test and bending test. *Journal of Physics:*

Conference Series, *2193*, 012039. https://doi.org/10.1088/1742-6596/2193/1/012039

Sisquella, X., Ofir-Birin, Y., Pimentel, M. A., Cheng, L., Abou Karam, P., Sampaio, N. G., ... & Regev-Rudzki, N. (2017). Malaria parasite DNA-harbouring vesicles activate cytosolic immune sensors. *Nature Communications*, *8*(1), 1985. https://doi.org/10.1038/s41467-017-02083-1

Solchaga, L. A., Gao, J., Dennis, J. E., Awadallah, A., Lundberg, M., Caplan, A. I., & Goldberg, V. M. (2002). Treatment of osteochondral defects with autologous bone marrow in a hyaluronan-based delivery vehicle. *Tissue Engineering*, *8*(2), 333-347. https://doi.org/10.1089/107632702753725085

Song, N., Scholtemeijer, M., & Shah, K. (2020). Mesenchymal stem cell immunomodulation: mechanisms and therapeutic potential. *Trends in Pharmacological Sciences*, *41*(9), 653-664. https://doi.org/10.1016/j.tips.2020.06.009

Stanić, V., Dimitrijević, S., Antić-Stanković, J., Mitrić, M., Jokić, B., Plećaš, I. B., & Raičević, S. (2010). Synthesis, characterization and antimicrobial activity of copper and zinc-doped hydroxyapatite nanopowders. *Applied Surface Science*, *256*(20), 6083-6089. https://doi.org/10.1016/j.apsusc.2010.03.124

Su, W. T., Chiou, W. L., Yu, H. H., & Huang, T. Y. (2016). Differentiation potential of SHEDs using biomimetic periosteum containing dexamethasone. *Materials Science and Engineering: C*, *58*, 1036-1045. https://doi.org/10.1016/j.msec.2015.09.077

Su, Y., Gao, Q., Deng, R., Zeng, L., Guo, J., Ye, B., ... & Guo, X. (2022). Aptamer engineering exosomes loaded on biomimetic periosteum to promote angiogenesis and bone regeneration by targeting injured nerves via JNK3 MAPK pathway. *Materials Today Bio*, *16*, 100434. https://doi.org/10.1016/j.mtbio.2022.100434

Sun, X., Mao, Y., Liu, B., Gu, K., Liu, H., Du, W., ... & Zhang, J. (2023). Mesenchymal stem cell-derived exosomes enhance 3D-printed scaffold functions and promote alveolar bone defect repair by enhancing angiogenesis. *Journal of Personalized Medicine*, *13*(2), 180. https://doi.org/10.3390/jpm13020180

Sutterwala, F. S., Haasken, S., & Cassel, S. L. (2014). Mechanism of NLRP3 inflammasome activation. *Annals of the New York Academy of Sciences*, *1319*(1), 82-95. https://doi.org/10.1111/nyas.12458

Swanson, W. B., Zhang, Z., Xiu, K., Gong, T., Eberle, M., Wang, Z., & Ma, P. X. (2020). Scaffolds with controlled release of pro-mineralization exosomes to promote craniofacial bone healing without cell transplantation. *Acta Biomaterialia*, *118*, 215-232. https://doi.org/10.1016/j.actbio.2020.09.052

Syanda, A. M., Kringstad, V. I., Blackford, S. J., Kjesbu, J. S., Ng, S. S., Ma, L., ... & Strand, B. L. (2022). Sulfated alginate reduces pericapsular fibrotic overgrowth on encapsulated cGMP-compliant hPSC-hepatocytes in mice. *Frontiers in Bioengineering and Biotechnology*, *9*, 816542. https://doi.org/10.3389/fbioe.2021.816542

Tabassum, S. (2020). Role of substitution in bioceramics. In *Handbook of ionic substituted hydroxyapatites* (pp. 117-148). Elsevier. https://doi.org/10.1016/B978-0-08-102834-6.00005-7

Tai, H. Y., Fu, E., & Don, T. M. (2012). Calcium phosphates synthesized by reverse emulsion method for the preparation of chitosan composite membranes. *Carbohydrate Polymers*, *88*(3), 904-911. https://doi.org/10.1016/j.carbpol.2012.01.042

Tao, F., Cheng, Y., Tao, H., Jin, L., Wan, Z., Dai, F., ... & Deng, H. (2020). Carboxymethyl chitosan/sodium alginate-based micron-fibers fabricated by emulsion electrospinning for periosteal tissue engineering. *Materials & Design*, *194*, 108849. https://doi.org/10.1016/j.matdes.2020.108849

Tariq, S., Shah, S. A., Hameed, F., Mutahir, Z., Khalid, H., Tufail, A., ... & Khan, A. F. (2024). Tissue engineered periosteum: Fabrication of a gelatin basedtrilayer composite scaffold with biomimetic properties for enhanced bone healing. *International Journal of Biological Macromolecules*, *263*, 130371. https://doi.org/10.1016/j.ijbiomac.2024.130371

Taylor, M., Urquhart, A. J., Zelzer, M., Davies, M. C., & Alexander, M. R. (2007). Picoliter water contact angle measurement on polymers. *Langmuir*, *23*(13), 6875-6878. https://doi.org/10.1021/la070100j

Ternane, R., Cohen-Adad, M. T., Panczer, G., Goutaudier, C., Kbir-Ariguib, N., Trabelsi-Ayedi, M., ... & Massiot, D. (2002). Introduction of boron in hydroxyapatite: synthesis and structural characterization. *Journal of Alloys and Compounds*, *333*(1-2), 62-71. https://doi.org/10.1016/S0925-8388(01)01558-4

Thitiset, T., Damrongsakkul, S., Yodmuang, S., Leeanansaksiri, W., Apinun, J., & Honsawek, S. (2021). A novel gelatin/chitooligosaccharide/demineralized bone matrix composite scaffold and periosteum-derived mesenchymal stem cells for bone tissue engineering. *Biomaterials Research*, *25*(1), 19. https://doi.org/10.1186/s40824-021-00220-y

Tilkin, R. G., Mahy, J. G., Régibeau, N., Grandfils, C., & Lambert, S. D. (2019). Optimization of synthesis parameters for the production of biphasic calcium phosphate ceramics via wet precipitation and sol- gel process. *ChemistrySelect*, *4*(21), 6634-6641. https://doi.org/10.1002/slct.201901175

Truong-Tran, A. Q., Carter, J., Ruffin, R. E., & Zalewski, P. D. (2001). The role of zinc in caspase activation and apoptotic cell death. *Biometals*, *14*, 315-330. https://doi.org/10.1023/a:1012993017026

Turhan, E. A., Akbaba, S., Tezcaner, A., & Evis, Z. (2023). Boron nitride nanofiber/Zn-doped hydroxyapatite/polycaprolactone scaffolds for bone tissue engineering applications. *Biomaterials Advances*, *148*, 213382. https://doi.org/10.1016/j.bioadv.2023.213382

Ueda, M., Yokota, T., Honda, M., Lim, P. N., Osaka, N., Makita, M., ... & Aizawa, M. (2021). Regulating size of silver nanoparticles on calcium carbonate via ultrasonic spray for effective antibacterial efficacy and sustained release. *Materials Science and Engineering: C*, *125*, 112083. https://doi.org/10.1016/j.msec.2021.112083

Uysal, I., Yilmaz, B., & Evis, Z. (2020). Boron doped hydroxapatites in biomedical applications. *Journal of Boron*, *5*(4), 199-208. https://doi.org/10.30728/boron.734804

van Rijt, M. M., Nooteboom, S. W., van der Weijden, A., Noorduin, W. L., & de With, G. (2021). Stability-limited ion-exchange of calcium with zinc in biomimetic hydroxyapatite. *Materials & Design*, *207*, 109846. https://doi.org/10.1016/j.matdes.2021.109846

Vitale, M., Ligorio, C., McAvan, B., Hodson, N. W., Allan, C., Richardson, S. M., ... & Bella, J. (2022). Hydroxyapatite-decorated Fmoc-hydrogel as a bone-mimicking substrate for osteoclast differentiation and culture. *Acta Biomaterialia*, *138*, 144-154. https://doi.org/10.1016/j.actbio.2021.11.011

Wang, H. Y., & Zhang, Y. Q. (2014). Processing and characterisation of a novel electropolymerized silk fibroin hydrogel membrane. *Scientific Reports*, *4*(1), 1-11. https://doi.org/10.1038/srep06182

Wang, M. H., Zhou, X. M., Zhang, M. Y., Shi, L., Xiao, R. W., Zeng, L. S., … Mai, S. J. (2017). BMP2 promotes proliferation and invasion of nasopharyngeal carcinoma cells via mTORC1 pathway. *Aging*, *9*(4), 1326–1340. https://www.nature.com/articles/srep06182#article-info

Wang, T., Xue, Y., Zhang, W., Zheng, Z., Peng, X., & Zhou, Y. (2024). Collagen sponge scaffolds loaded with Trichostatin A pretreated BMSCs-derived exosomes regulate macrophage polarization to promote skin wound healing. *International Journal of Biological Macromolecules*, *269*, 131948. https://doi.org/10.1016/j.ijbiomac.2024.131948

Wang, T., Zhai, Y., Nuzzo, M., Yang, X., Yang, Y., & Zhang, X. (2018). Layer-by-layer nanofiber-enabled engineering of biomimetic periosteum for bone repair and reconstruction. *Biomaterials*, *182*, 279-288. https://doi.org/10.1016/j.biomaterials.2018.08.028

Wang, Z., Yang, H., & Zhu, Z. (2019). Study on the blends of silk fibroin and sodium alginate: Hydrogen bond formation, structure and properties. *Polymer*, *163*, 144-153. https://doi.org/10.1016/j.polymer.2019.01.004

Weber, A., Wasiliew, P., & Kracht, M. (2010). Interleukin-1 (IL-1) pathway. *Science Signaling*, *3*(105cm1), 1-6. https://doi.org/10.1126/scisignal.3105cm1

Wittaya-areekul, S., & Prahsarn, C. (2006). Development and in vitro evaluation of chitosan–polysaccharides composite wound dressings. *International Journal of Pharmaceutics*, *313*(1-2), 123-128. https://doi.org/10.1016/j.ijpharm.2006.01.027

Wu, F., Lin, D. D., Chang, J. H., Fischbach, C., Estroff, L. A., & Gourdon, D. (2015). Effect of the materials properties of hydroxyapatite nanoparticles on fibronectin deposition and conformation. *Crystal Growth & Design*, *15*(5), 2452-2460. https://doi.org/10.1021/acs.cgd.5b00231

Wu, Q., Guo, Y., Li, H., Zhang, D., Wang, S., Hou, J., ... & Jin, C. (2024). Recombinant human collagen I/carboxymethyl chitosan hydrogel loaded with long-term released hUCMSCs derived exosomes promotes skin wound repair. *International Journal of Biological Macromolecules*, *265*, 130843. https://doi.org/10.1016/j.ijbiomac.2024.130843

Wu, Z., Liang, J., Zhu, S., Liu, N., Zhao, M., Xiao, F., ... & Zhu, P. (2023). Single-cell analysis of graft-infiltrating host cells identifies caspase-1 as a potential therapeutic target for heart transplant rejection. *Frontiers in Immunology*, *14*, 1251028. https://doi.org/10.3389/fimmu.2023.1251028

Xie, H., Wang, Z., Zhang, L., Lei, Q., Zhao, A., Wang, H., … & Zhang, W. (2016). Development of an angiogenesis-promoting microvesicle-alginate-polycaprolactone composite graft for bone tissue engineering applications. *The Journal of Life and Environmental Sciences*, *4*, e2040. https://doi.org/10.7717/peerj.2040

Yakubovich, E. I., Polischouk, A. G., & Evtushenko, V. I. (2022). Principles and problems of exosome isolation from biological fluids. *Biochemistry (Moscow), Supplement Series A: Membrane and Cell Biology*, *16*(2), 115-126. https://doi.org/10.1134/S1990747822030096

Yang, C., Zhao, C., Wang, X., Shi, M., Zhu, Y., Jing, L., ... & Chang, J. (2019). Stimulation of osteogenesis and angiogenesis by micro/nano hierarchical hydroxyapatite via macrophage immunomodulation. *Nanoscale*, *11*(38), 17699-17708. https://doi.org/10.1039/C9NR05730G

Yang, F., Dong, W. J., He, F. M., Wang, X. X., Zhao, S. F., & Yang, G. L. (2012). Osteoblast response to porous titanium surfaces coated with zinc-substituted hydroxyapatite. *Oral Surgery, Oral Medicine, Oral Pathology and Oral Radiology*, *113*(3), 313-318. https://doi.org/10.1016/j.tripleo.2011.02.049

Yang, H., Qu, X., Lin, W., Wang, C., Zhu, D., Dai, K., & Zheng, Y. (2018). In vitro and in vivo studies on zinc-hydroxyapatite composites as novel biodegradable metal matrix composite for orthopedic applications. *Acta Biomaterialia*, *71*, 200-214. https://doi.org/10.1016/j.actbio.2018.03.007

Yang, Z., Yang, Z., Ding, L., Zhang, P., Liu, C., Chen, D., ... & Chen, X. (2022). Self-adhesive hydrogel biomimetic periosteum to promote critical-size bone defect repair via synergistic osteogenesis and angiogenesis. *ACS Applied Materials & Interfaces*, *14*(32), 36395-36410. https://doi.org/10.1021/acsami.2c08400

Yao, J., Huang, C., Yao, J., Hui, J., Shen, S., Zheng, X., ... & Fan, D. (2024). A moldable hydrogel based on sericin and Zn2+/F-dual-doped hydroxyapatite promotes skull defect repair through the synergistic effects of immunoregulation, enhanced angiogenesis and osteogenesis. *Chemical Engineering Journal*, *491*, 151789. https://doi.org/10.1016/j.cej.2024.151789

Yao, M., Liang, S., Zeng, Y., Peng, F., Zhao, X., Du, C., ... & Zhang, Y. (2024). Dual factor-loaded artificial periosteum accelerates bone regeneration. *ACS Biomaterials Science & Engineering*, *10*(4), 2200-2211. https://doi.org/10.1021/acsbiomaterials.3c01587

Yilmaz, B., Alshemary, A. Z., & Evis, Z. (2019). Co-doped hydroxyapatites as potential materials for biomedical applications. *Microchemical Journal*, *144*, 443-453. https://doi.org/10.1016/j.microc.2018.10.007

Yin, J., Qiu, S., Shi, B., Xu, X., Zhao, Y., Gao, J., ... & Min, S. (2018). Controlled release of FGF-2 and BMP-2 in tissue engineered periosteum promotes bone repair in rats. *Biomedical Materials*, *13*(2), 025001. https://doi.org/10.1088/1748-605X/aa93c0

Ying, X., Cheng, S., Wang, W., Lin, Z., Chen, Q., Zhang, W., ... & Lu, C. (2011). Effect of boron on osteogenic differentiation of human bone marrow stromal cells. *Biological Trace Element Research*, *144*, 306-315. https://doi.org/10.1007/s12011-011-9094-x

Yoo, D. S., Cho, J. S., Chung, Y. C., & Rhee, S. H. (2021). Defect structures of sodium and chloride co-substituted hydroxyapatite and its osseointegration capacity. *Journal of Materials Science*, *56*, 5493-5508. https://doi.org/10.1007/s10853-020-05645-9

You, Y., Min, B. M., Lee, S. J., Lee, T. S., & Park, W. H. (2005). In vitro degradation behavior of electrospun polyglycolide, polylactide, and poly (lactide- co-glycolide). *Journal of Applied Polymer Science*, *95*(2), 193-200.

Yu, H., Lin, L., Zhang, Z., Zhang, H., & Hu, H. (2020). Targeting NF-κB pathway for the therapy of diseases: mechanism and clinical study. *Signal Transduction and Targeted Therapy*, *5*(1), 209.

Yu, L., Wei, Q., Li, J., Wang, H., Meng, Q., Xie, E., ... & Li, B. (2023). Engineered periosteum-diaphysis substitutes with biomimetic structure and composition promote the repair of large segmental bone defects. Composites Part B: Engineering, *252*, 110505. https://doi.org/10.1016/j.actbio.2020.06.030

Yu, W., Wang, H., Sun, R., & Chen, K. (2021). Electrodeposition of micro-nano hierarchically structured fluoridated hydroxyapatite coating on AZ31B alloy. *Surface Engineering*, *37*(9), 1186-1193. https://doi.org/10.1080/02670844.2020.1815485

Yu, Y., Wang, Y., Zhang, W., Wang, H., Li, J., Pan, L., ... & Li, B. (2020). Biomimetic periosteum-bone substitute composed of preosteoblast-derived matrix and hydrogel for large segmental bone defect repair. *Acta Biomaterialia*, *113*, 317-327. https://doi.org/10.1016/j.actbio.2020.06.030

Yuan, M., Liu, K., Jiang, T., Li, S., Chen, J., Wu, Z., ... & Chen, Z. (2022). GelMA/PEGDA microneedles patch loaded with HUVECs-derived exosomes and Tazarotene promote diabetic wound healing. *Journal of Nanobiotechnology*, *20*(1), 147. https://doi.org/10.1186/s12951-022-01354-4

Zampieron, C. I., Cesca, K., Faita, F. L., Immich, A. P. S., & Parize, A. L. (2023). Effect of heat-treatment temperature on the structure of calcium phosphate synthesized by wet precipitation. *Ceramics International*, *49*(17), 29198-29207. https://doi.org/10.1016/j.ceramint.2023.06.204

Zeng, Y. J., Sun, X. P., Yang, J., Wu, W. H., Xu, X. H., & Yan, Y. P. (2003). Mechanical properties of nasal fascia and periosteum. *Clinical Biomechanics*, *18*(8), 760-764. https://doi.org/10.1016/S0268-0033(03)00136-0

Zhang, F. X., Liu, P., Ding, W., Meng, Q. B., Su, D. H., Zhang, Q. C., ... & Jiang, L. B. (2021). Injectable Mussel- Inspired highly adhesive hydrogel with exosomes for endogenous cell recruitment and cartilage defect regeneration. *Biomaterials*, *278*, 121169. https://doi.org/10.1016/j.biomaterials.2021.121169

Zhang, K., & Cheng, K. (2023b). Stem cell-derived exosome versus stem cell therapy. *Nature Reviews Bioengineering*, *1*(9), 608-609. https://doi.org/10.1038/s44222-023-00064-2

Zhang, R., Wei, Z., Lei, W., Jiang, T., Zhang, Q., & Shi, D. (2020). Mitigating the shielding effect of ether oxygen in poly (ethylene glycol) on boron atoms in boron- doped Poly (ethylene glycol) hybrid polymer electrolyte by introducing siloxane spacers. *ChemElectroChem*, *7*(15), 3353-3360. https://doi.org/10.1002/celc.202000784

Zhang, W., Sun, T., Zhang, J., Hu, X., Yang, M., Han, L., ... & Li, Z. (2023a). Construction of artificial periosteum with methacrylamide gelatin hydrogel-

wharton's jelly based on stem cell recruitment and its application in bone tissue engineering. *Materials Today Bio*, *18*, 100528. https://doi.org/10.1016/j.mtbio.2022.100528

Zhang, W., Wang, N., Yang, M., Sun, T., Zhang, J., Zhao, Y., ... & Li, Z. (2022). Periosteum and development of the tissue-engineered periosteum for guided bone regeneration. *Journal of Orthopaedic Translation*, *33*, 41-54. https://doi.org/10.1016/j.jot.2022.01.002

Zhang, Z., Yang, J., Yan, W., Li, Y., Shen, Z., & Asahara, T. (2016). Pretreatment of cardiac stem cells with exosomes derived from mesenchymal stem cells enhances myocardial repair. *Journal of the American Heart Association*, *5*(1), e002856. https://doi.org/10.1161/JAHA.115.002856

Zhao, D., Wang, Y., Yu, Z., Wang, C., Zhang, H., Han, D., & Li, Q. (2023a). Co-culture bioprinting of tissue-engineered bone-periosteum biphasic complex for repairing critical-sized skull defects in rabbits. *International Journal of Bioprinting*, *9*(3), 698. https://doi.org/10.18063/ijb.698

Zhao, F., Zhang, C., Liu, J., Liu, L., Cao, X., Chen, X., ... & Shao, L. (2020a). Periosteum structure/function-mimicking bioactive scaffolds with piezoelectric/chem/nano signals for critical-sized bone regeneration. *Chemical Engineering Journal*, *402*, 126203. https://doi.org/10.1016/j.cej.2020.126203

Zhao, L., Zhao, J., Yu, J. J., & Zhang, C. (2020b). Irregular bone defect repair using tissue-engineered periosteum in a rabbit model. *Tissue Engineering and Regenerative Medicine*, *17*, 717-727. https://doi.org/10.1007/s13770-020-00282-4

Zhao, L., Zhao, J., Yu, J., Sun, R., Zhang, X., & Hu, S. (2017). In vivo investigation of tissue-engineered periosteum for the repair of allogeneic critical size bone defects in rabbits. *Regenerative Medicine*, *12*(4), 353-364. https://doi.org/10.2217/rme-2016-0157

Zhao, Y., Xiong, Y., Zheng, J., Kongling, W., Chen, J., Li, C., ... & Wang, X. (2023b). A multifaceted biomimetic periosteum with a lamellar architecture and osteogenic/angiogenic dual bioactivities. *Biomaterials Science*, *11*(11), 3878-3892. https://doi.org/10.1039/D3BM00382E

Zhong, Z., & Ma, J. (2017). Fabrication, characterization, and in vitro study of zinc substituted hydroxyapatite/silk fibroin composite coatings on titanium for biomedical applications. *Journal of Biomaterials Applications*, *32*(3), 399-409. https://doi.org/10.1177/0885328217723501

Zhou, Z., Liu, Y., Li, W., Zhao, Z., Xia, X., Liu, J., ... & Zhu, X. (2024). A self-adaptive biomimetic periosteum employing nitric oxide release for augmenting angiogenesis in bone defect regeneration. *Advanced Healthcare Materials*, *13*(3), 2302153. https://doi.org/10.1002/adhm.202302153

Zhu, M., Heydarkhan-Hagvall, S., Hedrick, M., Benhaim, P., & Zuk, P. (2013). Manual isolation of adipose-derived stem cells from human lipoaspirates. *JoVE (Journal of Visualized Experiments)*, (79), e50585. https://doi.org/10.3791/50585

Zhu, Y., Jia, Y., Wang, Y., Xu, J., & Chai, Y. (2019). Impaired bone regenerative effect of exosomes derived from bone marrow mesenchymal stem cells in type 1 diabetes. *Stem Cells Translational Medicine*, *8*(6), 593-605. https://doi.org/10.1002/sctm.18-0199

Zhuang, Z., John, J. V., Liao, H., Luo, J., Rubery, P., Mesfin, A., ... & Zhang, X. (2020). Periosteum mimetic coating on structural bone allografts via electrospray deposition enhances repair and reconstruction of segmental defects. *ACS Biomaterials Science & Engineering*, *6*(11), 6241-6252. https://dx.doi.org/10.1021/acsbiomaterials.0c00421

Ziadlou, R., Rotman, S., Teuschl, A., Salzer, E., Barbero, A., Martin, I., ... & Grad, S. (2021). Optimization of hyaluronic acid-tyramine/silk-fibroin composite hydrogels for cartilage tissue engineering and delivery of anti-inflammatory and anabolic drugs. *Materials Science and Engineering: C*, *120*, 11170. https://doi.org/10.1016/j.msec.2020.111701

APPENDICES

A. BCA Calibration Curve (n=3)

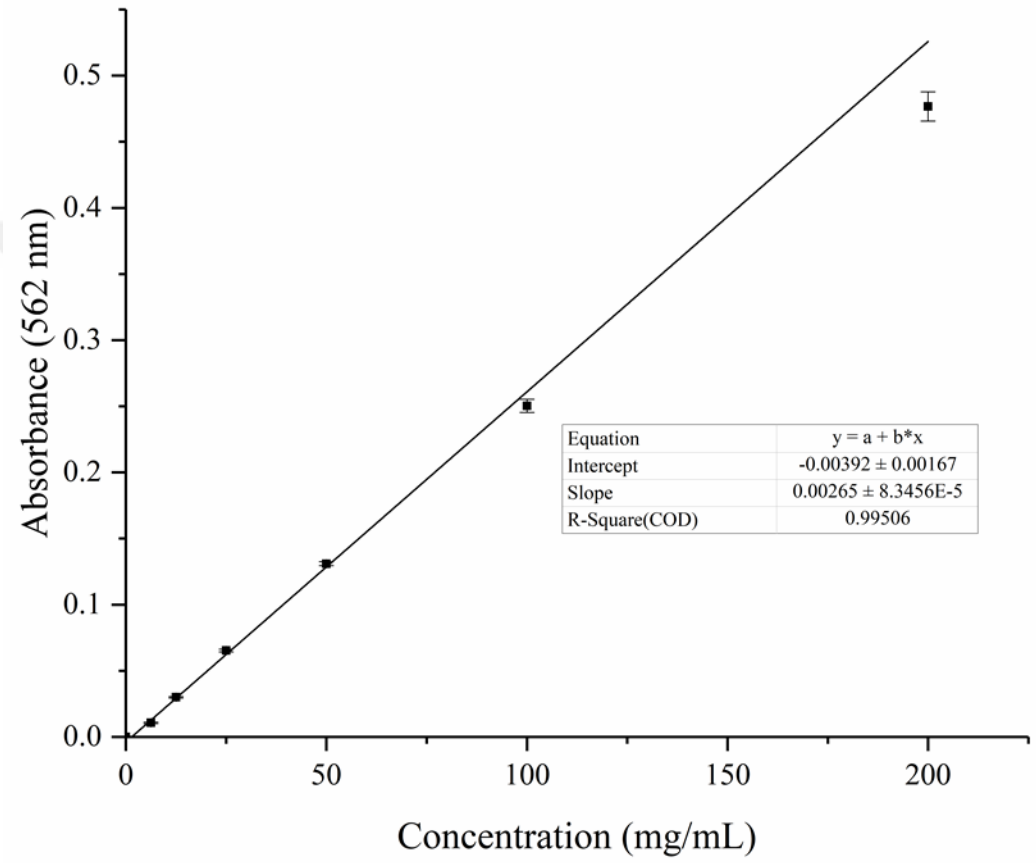

B. DMMB Calibration Curve (n=3)

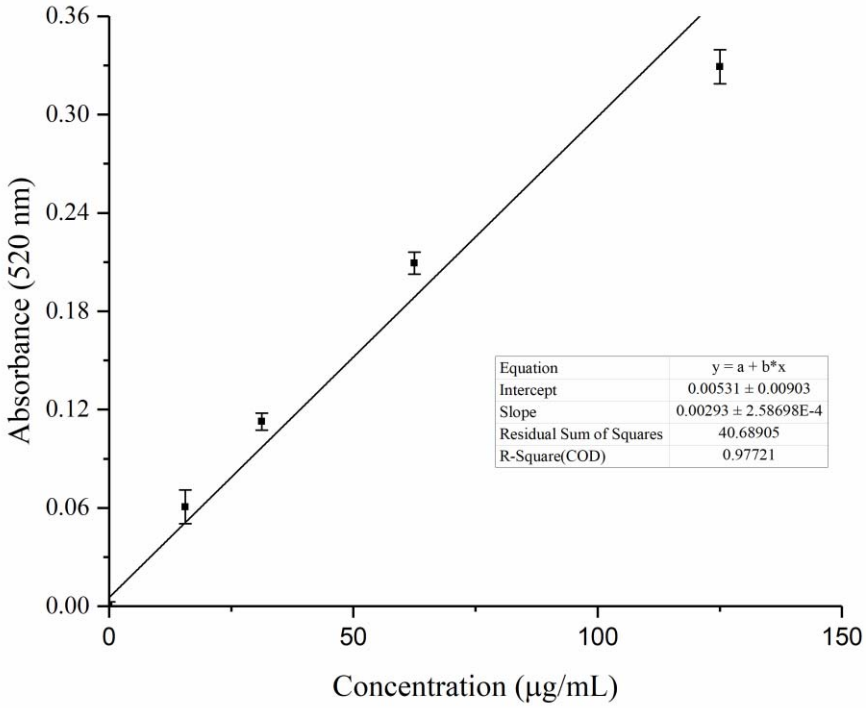

C. DNA Calibration Curve (n=3)

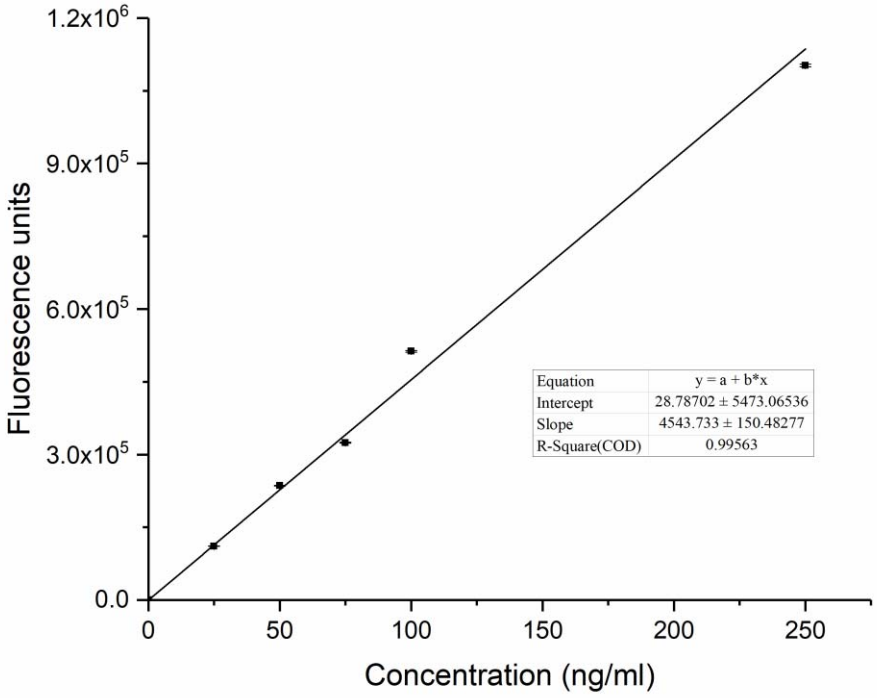

D. p-nitrophenol Calibration Curve (n=3)

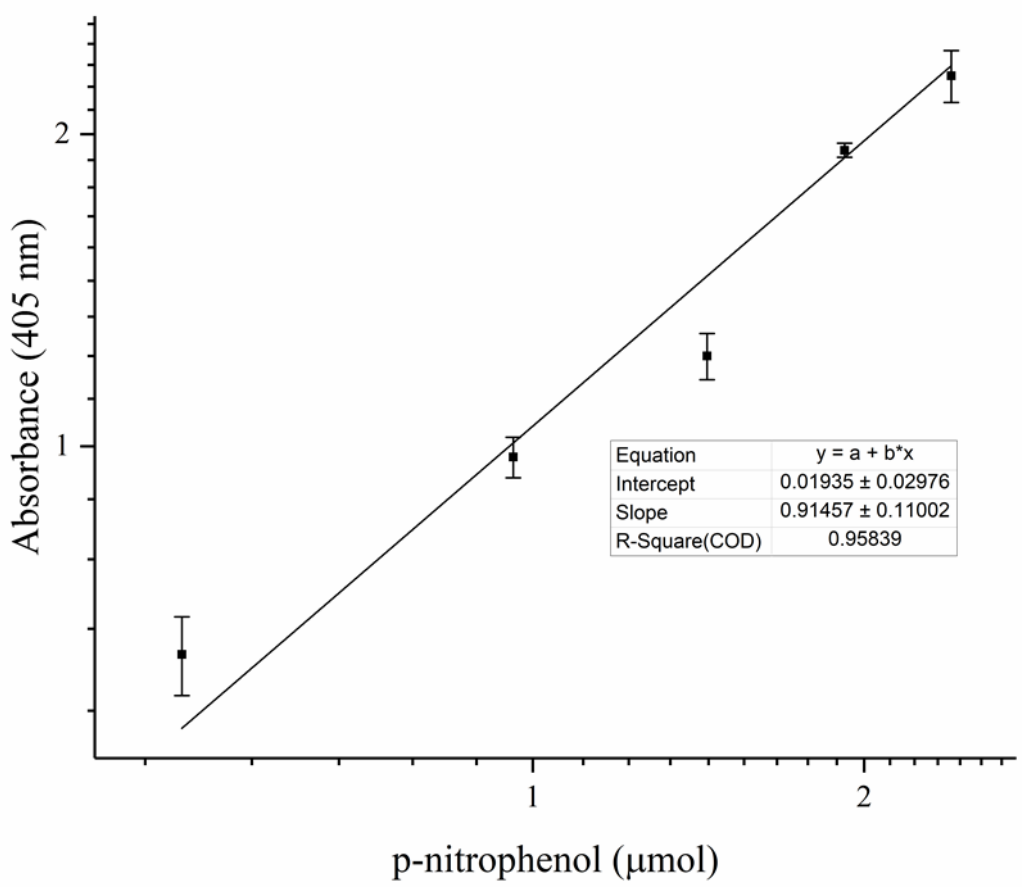

E. OCN Calibration Curve (n=3)

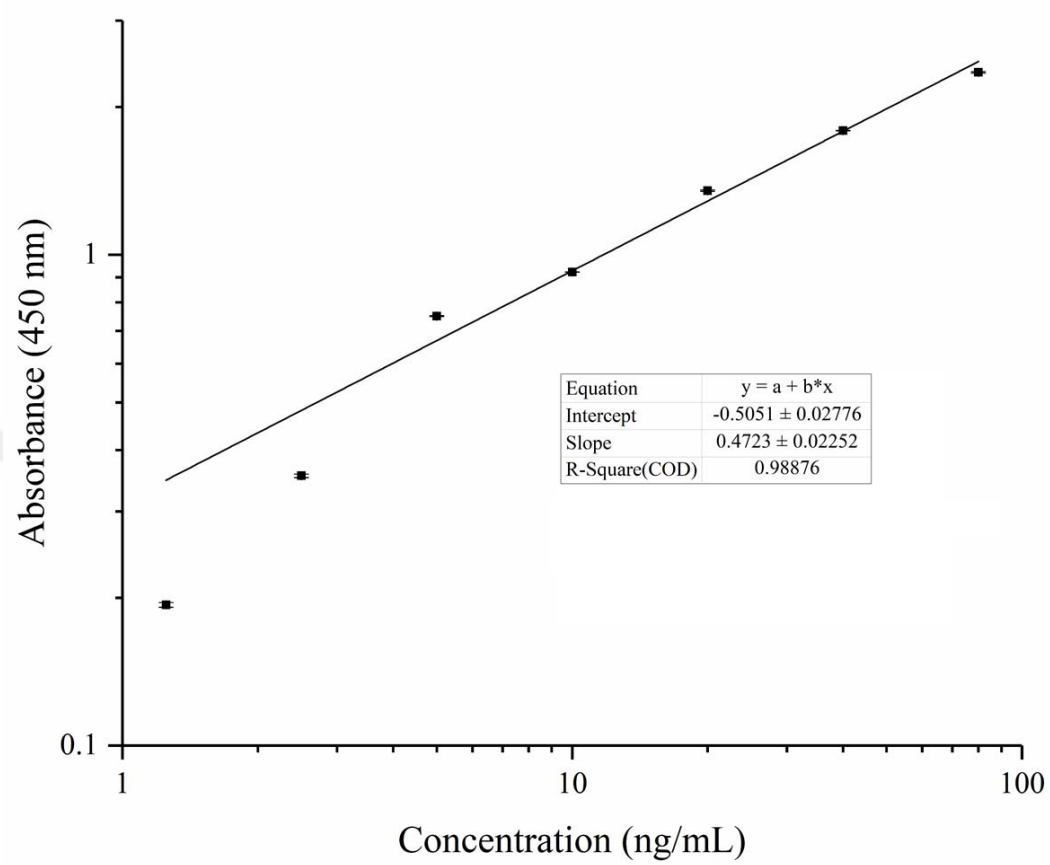

F. IL1B Calibration Curve (n=3)

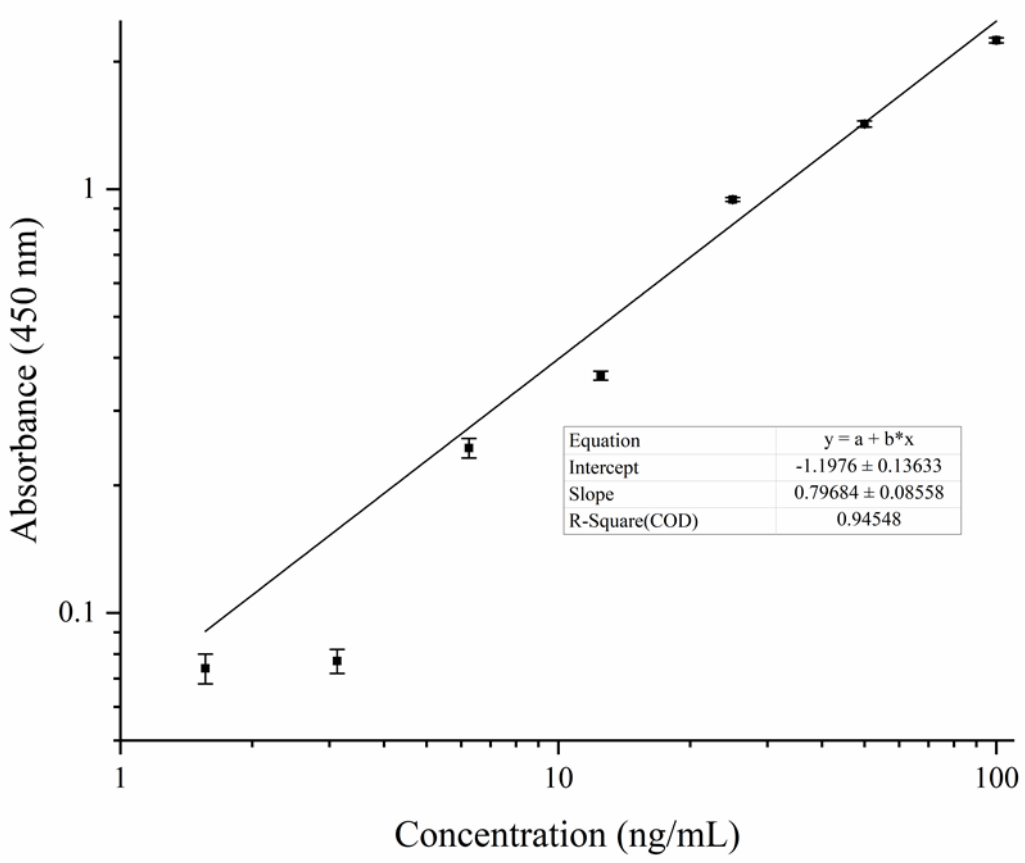

G. CASP1 Calibration Curve (n=3)

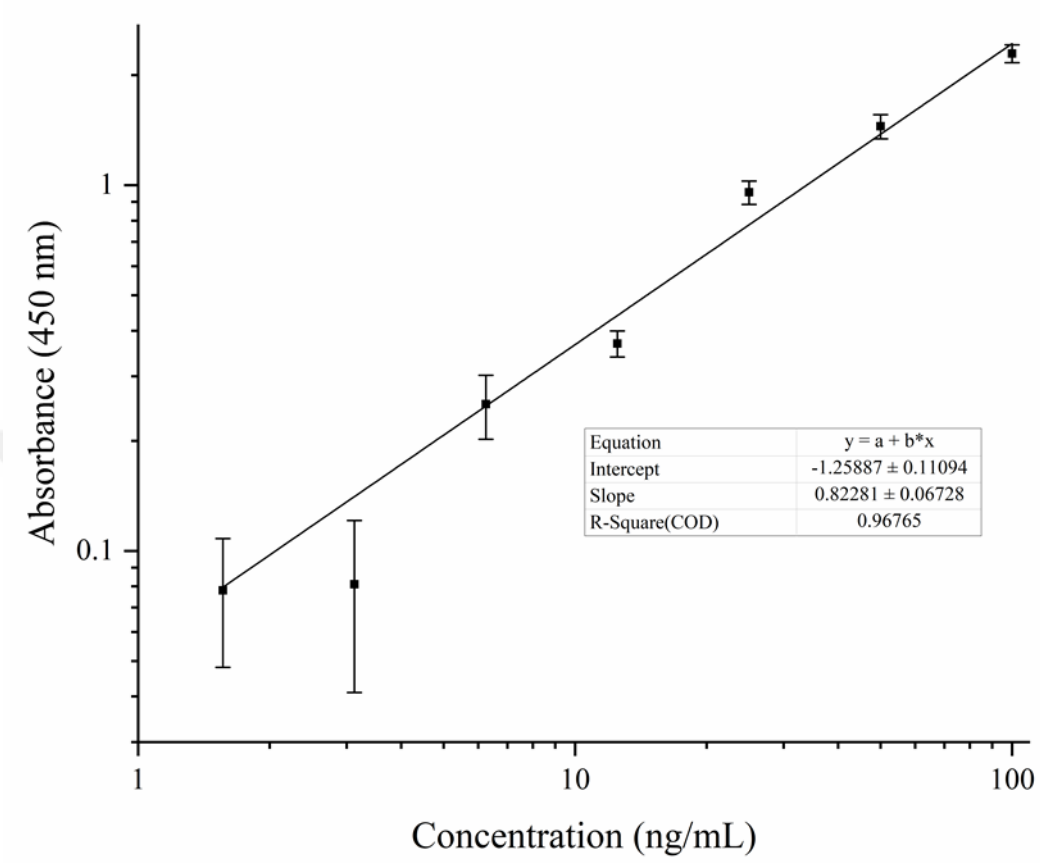

H. VEGFA Calibration Curve (n=3)

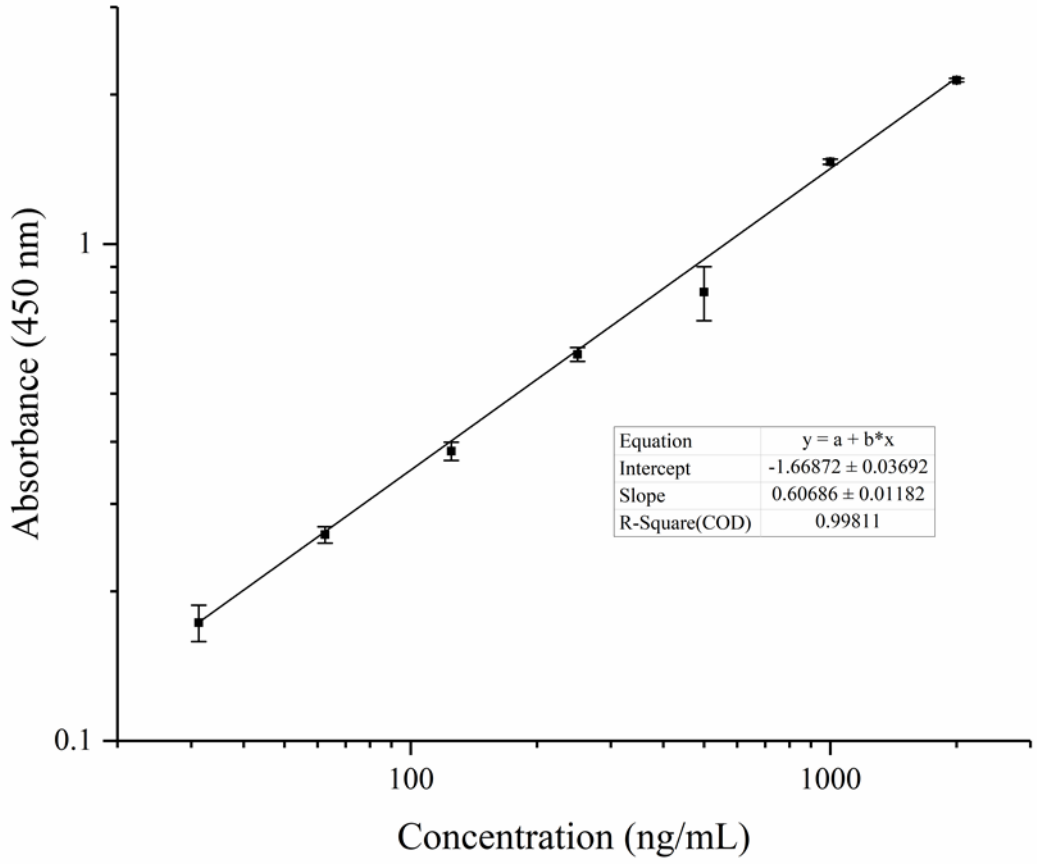

CURRICULUM VITAE

Surname, Name: Akbaba Fathi, Sema

EDUCATION

Degree	Institution	Year of Graduation
MS	METU, Biotechnology	2018
BS	ITU, Molecular Biology and Genetics	2015
High School	Atatürk High School, Ankara	2009

FOREIGN LANGUAGES

English

PUBLICATIONS

1. Turhan E. A., Akbaba S., Tezcaner A. and Evis Z. "Boron nitride nanofiber/Zn-doped hydroxyapatite/polycaprolactone scaffolds for bone tissue engineering applications", Biomaterials Advances, 148, 213382 (2023).

2. Balaban Y. E., Akbaba S., Bozkurt S. B., Buyuksungur A. Akgun E. E., Gonen Z. B., ... and Hakki S. S. "Local application of gingiva- derived mesenchymal stem cells on experimental periodontitis in rats" Journal of Periodontology, 95(5), 456-468 (2023).

3. Pazarçeviren A. E., Akbaba S., Evis Z., and Tezcaner A. "Versatile-in-all-trades: multifunctional boron-doped calcium-deficient hydroxyapatite directs immunomodulation and regeneration", ACS Biomaterials Science & Engineering, 8(7), 3038-3053 (2022).

4. Pazarçeviren A. E., Akbaba S., Tezcaner A., Keskin D., and Evis Z. "Seamless and Robust Alginate/Gelatin Coating on Ti-6Al-4V as a Gap Filling Interphase", Applied Surface Science, 152393 (2022).

5. Seemann A., Akbaba S., Buchholz J., Türkkan S., Tezcaner A., Woche S. K., ... and Dräger G. "RGD-Modified Titanium as an Improved Osteoinductive

Biomaterial for Use in Dental and Orthopedic Implants", Bioconjugate Chemistry, 33(2), 294-300 (2022).

6. Akbaba S., Atila D., Keskin D., Tezcaner T., & Tezcaner A. "Multilayer fibroin/chitosan oligosaccharide lactate and pullulan immunomodulatory patch for treatment of hernia and prevention of intraperitoneal adhesion", Carbohydrate Polymers, 265, 118066 (2021).